
Formation of cold gas filaments from colliding supershells

Evangelia Ntormousi



Formation of cold gas filaments from colliding supershells



Ph.D Thesis at the faculty of physics
of the Ludwig-Maximilians-Universität München

Presented by Evangelia Ntormousi
from Thessaloniki, Greece
in Munich, on February the 22nd, 2012



1st Evaluator: Prof. Dr. Andreas Burkert

2nd Evaluator: Prof. Dr. Harald Lesch

Contents

Contents	vii
List of Figures	x
Abstract	xi
Zusammenfassung	xiii
1 Preface	1
2 The Interstellar Medium	3
2.1 General	3
2.2 Atomic Interstellar Gas	3
2.2.1 Molecular Interstellar Gas	5
2.2.2 Ionized Interstellar Gas	7
2.3 Dust	10
2.4 Cosmic Rays	11
2.5 Magnetic Fields	14
2.6 The system as a whole	15
2.6.1 Models of the multi-phase ISM	15
2.6.2 Cooling and Heating Processes of the Interstellar Gas	16
2.6.3 The modern view of the ISM: the role of turbulence	21
3 Principles of Hydrodynamics	23
3.1 The equations of hydrodynamics	23
3.1.1 The equation of continuity	23
3.1.2 The force equation	24
3.1.3 The energy equation	25
3.2 Hydrodynamical Instabilities	26
3.2.1 The Non-linear Thin Shell Instability	27
3.2.2 The Kelvin-Helmholtz Instability	29
3.2.3 The Thermal Instability	32
3.3 The instabilities combined	33
3.4 Some comments on turbulence	35

4	Previous Work	39
4.1	Molecular Cloud Formation	39
4.2	Shell fragmentation and collapse	41
5	Numerical Method	43
5.1	Solving the equations of hydrodynamics on a grid	43
5.2	The RAMSES code	45
5.3	Sources and sinks of energy	46
5.3.1	Implementation of a new cooling and heating module	46
5.3.2	Implementation of a winds	46
5.4	Creating turbulent initial conditions	46
5.5	Simulation setup	48
6	Formation of cold filaments from colliding shells	49
6.1	Shell collision in a uniform diffuse medium	49
6.2	Shell collision in a turbulent diffuse medium	56
7	Morphological features of the cold clumps	67
7.1	General	67
7.2	Velocity dispersions	74
7.3	Sizes	74
7.4	Clump evolution	76
8	Metal enrichment of the clouds	79
8.1	Setup of the simulation	79
8.2	Metal enrichment of the gas from the OB associations	84
8.3	Metal enrichment of the clumps	86
9	Summary and Conclusions	91
	Bibliography	99
	Acknowledgments	101
	Curriculum Vitae	103

List of Figures

2.1	Distance calculation ambiguity	6
2.2	The "Pipe" dark nebula	8
2.3	The "Shamrock" nebula	10
2.4	Dense gas filaments	12
2.5	The Milky Way in various wavelengths	13
2.6	Cooling-heating equilibrium curve	17
2.7	McKee & Ostriker (1977) view of the ISM	18
2.8	Cooling and heating rates of the local ISM	20
3.1	Illustration of the Vishniac instability.	30
3.2	Eddies created by the Kelvin-Helmholtz instability	32
3.3	Instabilities in phase space	34
3.4	Two-dimensional slab	34
5.1	Energy and mass ejection from an "average star"	47
6.1	Collision snapshots: uniform background	50
6.2	Uniform background: zoom-in	51
6.3	Gas phase histogram: uniform background	53
6.4	Gas fractions with time: uniform background	54
6.5	Number of clumps with time	55
6.6	Collision snapshots: turbulent background	57
6.7	Turbulent background: zoom-in	58
6.8	Filament 1	59
6.9	Filament 2	60
6.10	Filament 3	61
6.11	Filament evolution	62
6.12	Phase histogram: turbulent background	63
6.13	Gas fractions: turbulent background	64
7.1	Condensing clouds	68
7.2	Rotating clouds	69
7.3	Clouds with random motions	70
7.4	Clouds with low internal velocities	71

7.5	Cloud velocity dispersions	72
7.6	Velocity dispersion with time	73
7.7	Clump size distributions	75
7.8	Clump size over Jeans length distributions	75
7.9	Cores in the phase diagram	77
8.1	AMR-unigrid comparison	80
8.2	Density and pressure histograms	81
8.3	AMR-unigrid comparison: Mass fractions with time	82
8.4	Shell collision with metal advection	85
8.5	2d histograms: density-metallicity distribution	87
8.6	Metal distribution of the clumps	88
8.7	Metal content of the clumps with distance from the stars	88
8.8	Metal content of the clumps with polar angle	89

Abstract

The aim of this work is to study the dynamics of the interstellar gas, with an eye towards the formation of the Cold Neutral Medium (CNM), gas with high densities ($n_H \simeq 100 \text{ cm}^{-3}$) and low temperatures ($T < 300 \text{ K}$). In particular, we want to explore the mechanisms that can lead to the filamentary structure typical of these clouds.

A natural mechanism for the formation of large amounts of cold gas in a small region are converging flows. This type of problem has been studied extensively in the literature in the form of academic, infinite high-Mach number flows that collide at a perturbed boundary. The novelty of our approach lies in simulating converging flows by using physically motivated parameters, extracted from models of young stellar feedback. This feedback creates finite, structured shocks which are the seeds for turbulence at the shock collision interface.

In our numerical experiments two superbubbles, blown by the violent feedback of OB associations, collide and fragment to form cold filaments through various fluid instabilities. The amount of cold gas formed, the morphologies and the kinematics of the cold gas clumps are roughly in accordance with observed properties of such structures. In particular, our simulations are able to capture the observed filamentary structure of the cold clouds and their fractal character.

The metal content of the clumps is tracked through an advected quantity in the code, inserted in the feedback regions along with the rest of the stellar feedback. Our studies show that little or no enrichment happens from one stellar generation to the next, if only turbulent diffusion is considered.

Although further work is needed in order to study the details of the clump structure and its dependence on the OB association parameters, this work opens a new path to the study of the ISM dynamics by showing that complex characteristics of the observed structures can be reproduced by applying physically motivated initial conditions.

Zusammenfassung

Das Ziel dieser Arbeit ist es, die Dynamik des interstellaren Gases zu studieren, insbesondere die Entstehung des kalten neutralen Mediums, d.h. Gases mit hohen Dichten ($n_H \simeq 100 \text{ cm}^{-3}$) und niedrigen Temperaturen ($T < 300 \text{ K}$). Wir wollen die Mechanismen, die die typische filamentartige Struktur dieser Wolken erzeugen, im Detail verstehen.

Ein natürlicher Mechanismus für die Entstehung großer Mengen kalten Gases in einem kleinen Gebiet sind konvergente Flüsse. Diese Art von Problem wurde in Form von akademischen Flüssen mit unendlich großen Mach Zahlen, die an einem gestörten Rand kollidieren, ausgiebig in der Literatur studiert. Unser Ansatz ist insofern neu, als das wir konvergierende Flüsse simulieren, indem wir physikalisch motivierte Parameter verwenden, die wir aus Modellen für das sogenannte Feedback junger Sterne erhalten, die aus Beobachtungen entstanden sind. Dieses Feedback erzeugt endliche, strukturierte Schocks, die als Keime fuer Turbulenzen an den von kollidierenden Schocks erzeugten Grenzflächen dienen.

In unseren numerischen Experimenten kollidieren zwei Superbubbles, erzeugt durch das heftige Feedback von OB-Sternansammlungen, miteinander und fragmentieren, wobei sich auf Grund verschiedener, in Flüssigkeiten typischer, Instabilitäten kalte Filamente ausbilden. Die Menge an dabei geformtem, kaltem Gas sowie die Morphologie und Kinematik der so erzeugten kalten Gasklumpen stimmt in guter Näherung mit den für derartige Strukturen beobachteten Eigenschaften überein. Insbesondere erwähnenswert ist, das unsere Simulationen in der Lage sind, die beobachtete, filamentartige Struktur und den fraktalen Charakter der kalten Molekülwolken zu reproduzieren.

Innerhalb des Codes verfolgen wir die Metallizität durch eine Größe, die zusammen mit dem restlichen stellaren Feedback in der OB-Sternansammlung erzeugt wird, aber selbst keine speziellen physikalischen Eigenschaften hat. Unsere Studien zeigen, das von einer stellaren Generation zur nächsten, sofern nur die Ausbreitung durch Turbulenzen berücksichtigt wird, wenig oder gar keine Anreicherung mit Metallen erfolgt.

Ogleich zum Verständnis der Details der Entstehung der klumpigen Strukturen und deren Abhngigkeit von den Parametern der OB-Sternansammlung weitere, detailliertere Studien nötig sind, öffnet diese Arbeit jedoch neue Wege, die Dynamik des Interstellaren Mediums zu studieren, da sie beweist, das die komplexen Charakteristika der beobachteten Strukturen durch das Anwenden physikalisch motivierter Parameter in den Anfangsbedingungen reproduziert werden können.

Chapter 1

Preface

*One Sun by Day, by Night ten thousand shine
And light us deep into the Deity.*

Edward Young, "*Night Thoughts*"

In the late eighteenth century, Sir Frederick William Herschel came across a puzzling fact in his deep sky observations: there were regions on the sky where there appeared to be no stars. This was not an easy observation to interpret. Did stars have a tendency to leave voids in the Universe? As it so often happens in science, the explanation was as simple, elegant and exciting as it was surprising and unexpected. These celestial voids turned out to be "dark clouds", nebulae which obscure the background starlight almost entirely. This discovery revolutionized the way scientists view the cosmos, as it gave the first indication that the Galaxy contains non-stellar matter which fills the vast space between the stars.

Support for this interpretation actually came much later, from Johannes Hartmann's (1904) discovery of an absorption line in stellar spectra that could only be explained by interstellar absorption. Three decades later, in 1930, Robert Julius Trumpler showed that, apart from Herschel's "dark clouds", interstellar space also contained a more diffuse gaseous material, thus discovering one more of what we now know to be at least four gaseous phases of Interstellar Matter. In the years that followed, the existence of all the other constituents of the Interstellar Medium were discovered, dust, magnetic fields, and cosmic rays.

It is nowadays a known fact that the constituents of Interstellar Matter not only affect the way stellar radiation reaches the Earth, but they are also important ingredients of the Galaxy as a complex system, especially in due to their active role in the process of star formation. Interstellar gas is the building material for stars and it carries the energy and mass ejected by them during their lives. Magnetic fields are thought to play an important role in the regulation of star formation. Dust, among others, provides an important cooling path for the gas and is an necessary catalyst for the formation of hydrogen molecules, as well as for other chemical reactions.

As a complex system the Interstellar Medium makes a fascinating area of study on its own, but it also holds great part of the solution to problems at much larger scales, as the laboratory of Galactic evolution. At the time this text is written, the mystery of galaxy formation and evolution is yet to be solved. Although the Λ CDM model for dark matter has

been very successful in reproducing the large-scale structure of the mass in the Universe, we are still far from understanding the mechanisms by which galaxies form their stars and the details of metal enrichment from one generation of stars to the next. Moreover, the processes which shape the distribution of masses in a young stellar cluster in an apparently universal way are still under debate and are possibly connected to the drivers of turbulence in the interstellar gas.

I strongly believe the answers to all these questions lie on understanding the physics of the interstellar medium. However, this thesis does not aspire to answer them. Instead, it would be considered successful by this author if it managed to break them down in simpler, more straightforward thought problems. More specifically, this is a thesis about the complex process of forming cold and dense gas out of the warm diffuse component of the interstellar medium.

The novel ingredient in this work is that the hot energetic component of the interstellar medium is controlling this transition, implemented in a self-consistent way, in the form of winds and supernova explosions from stellar models rather than as academic, perfect shocks. The non-linear nature of this system is what yields the complex cold structure we observe. Furthermore, this thesis studies the process of metal mixing between these components, with an eye towards the possible enrichment of the next generation of stars.

This counting as the first chapter of this work, the second chapter overviews the properties of interstellar matter as they are known at this time. The third chapter includes the theoretical background needed to follow the phenomena studied in this thesis, essentially an overview of hydrodynamics. The fourth chapter presents the current state of the art in the field of cold cloud formation and hot shell expansion, thus giving a more detailed motivation for this work. The fifth chapter is dedicated to the description of the techniques used for the numerical modeling of the systems under study, and the next chapters are dedicated to illustrating our results. The very last chapter summarizes and concludes the thesis.

The Interstellar Medium

2.1 General

Thanks to the continuous advances in astronomical observations it is now known that the space between stars is not empty, but rather filled with gas, dust and energetic particles.

The different ways in which stars interact with this material, which is collectively called the Interstellar Medium (ISM), leave spectacular tracks for astronomers to follow : HII regions, reflection nebulae, luminous shocks and supernova remnants. By studying these fascinating objects it has been discovered, for example, that the matter which fills the space between stars is a mixture of hydrogen, helium and a small amount of heavier elements, in a gaseous or in a solid state.

Most of the solid state of the ISM is dust, an ingredient with very important effects on the radiation we receive from the ISM. The gaseous state itself comprises many phases, ranging from molecular, to cool atomic, to ionized gas. In this Chapter we give an overview of the known properties of each of the gas phases, as well some general characteristics of interstellar dust. We also briefly mention some features of the Galactic magnetic fields and cosmic rays, since they are important sources of pressure and also tracers of many physical processes in the ISM.

2.2 Atomic Interstellar Gas

The phase of interstellar gas we refer to as neutral atomic gas is defined by the absence of Lyman continuum photons, meaning that hydrogen is mostly neutral. However, this term should not be interpreted in a very strict sense, since other species can still be ionized in this medium due to the dependence of interstellar extinction on wavelength. In fact, energetic charged particles traveling in the Galaxy, known as cosmic rays, are known to cause partial ionization even in the interiors of very dense clouds. What we call neutral atomic gas is actually not purely atomic, either. Some molecular lines have been detected in this medium, in the same way that atoms are known to exist in the coronas of molecular clouds.

The information contained in Chapter 2 is mostly a combination of material from the following sources: Tielens (2005), Lequeux (2005), Ferrière (2001) and Hollenbach & Thronson (1987), unless otherwise stated. Individual references for the information quoted here can be found in these reviews.

There are several ways to study the neutral atomic ISM observationally, in emission and in absorption. Since interstellar gas is mostly hydrogen, we can study many of its properties by observing the well-known 21 cm line radio emission from this atom.

This line results from the hyperfine structure of the hydrogen atom, caused by the interaction of the magnetic moments of the electron and the proton within the atom. The transition is strongly forbidden, with a spontaneous emission probability as low as $A_{ul} = 2.87 \times 10^{-15} \text{s}^{-1}$. Nonetheless, due to the enormous amounts of hydrogen in interstellar space we can indeed observe it. It is usually detected in absorption in front of continuum radio sources or in front of 21 cm emission of warmer gas. Moreover, since the lifetime of the upper sublevel is much longer than the average collision timescale in ISM conditions, local thermodynamical equilibrium (LTE) can be assumed for the gas when interpreting observations.

The main applications of 21 cm observations are to estimate the mass, the distribution and the kinematics of atomic hydrogen. From these observations we know, for example, that atomic hydrogen amounts to at least half of the mass of the interstellar medium of our Galaxy. This is roughly true for most of the mass in other galaxies as well. Since the 21 cm line is usually assumed to be optically thin (meaning that we assume all the photons produced in the emitting source can escape it), which might not always be the case, these masses are mostly upper limits.

By comparing absorption and emission spectra from the same region of the sky, we can identify two phases of neutral atomic hydrogen. A dense ($n_H \approx 10 - 50 \text{ cm}^{-3}$), cold ($T \approx 100 - 300 \text{ K}$) phase, which is usually called the cold neutral medium (CNM), and a more diffuse ($n_H \approx 0.1 - 0.3 \text{ cm}^{-3}$), warm ($T \approx 10000 \text{ K}$) phase, called the warm neutral medium (WNM). The WNM is extended in interstellar space and is mostly responsible for what we observe in emission, while the CNM forms discrete, highly inhomogeneous and structured filaments, which appear in the spectra as absorption peaks. We should point out that this extremely inhomogeneous structure of the CNM is believed to be a result of turbulence in interstellar space, a process which is actually the main subject of this thesis.

The WNM contains as much mass as the CNM in our Galaxy, but it forms a thicker disk, with a scale height of $|z| = 186 \text{ pc}$, compared to $|z| = 106 \text{ pc}$ of the CNM. From absorption measurements we know that local cold clouds have a velocity dispersion of 6.9 km/sec and from emission measurements that the WNM has a velocity dispersion of about 9 km/sec.

The distribution of H I in the Galaxy can also be deduced from 21 cm observations, although not without some uncertainties. In general, it is very difficult to discern the exact distribution of interstellar gas in the Galactic disk, the reason for this coming from the available ways to measure a cosmic object's distance from us. For example, to measure the distances to stars, when they are too far away to use parallaxes, we can use the difference between their apparent (m) and their absolute magnitude (M):

$$m - M = 5 \log \frac{d}{10 \text{ pc}} - A \quad (2.1)$$

where A is the extinction at the observed wavelength, primarily caused by interstellar dust. For the gas, however, it is not possible to measure distances this way, unless we know from the nature of the process that it is intrinsically spatially connected to stars. Examples of such objects are H II regions, formed by young massive stars as they ionize their surroundings (–See Figure 2.3 and Section 2.2.2). Another way to measure the distance to an object, which also comes from equation 2.1, involves determining the distance of stars unobscured by the cloud. This is applicable to dark, neutral clouds (–See Figure 2.2).

Of course, a spatial correlation between stars and a region of the ISM only happens for a few clouds. In absence of such a fortunate coincidence, the only way to determine the distance to a Galactic gaseous source is through its line-of-sight velocity, induced from its emission or absorption spectrum. In the case of atomic hydrogen velocity estimates come from 21 cm hydrogen line observations. By making 21 cm observations for many different lines of sight and correlating the resulting velocities with a model for the Galaxy's differential rotation curve, we can calculate the object's position in the Galaxy. It should be mentioned here that in emission this line probes the CNM and the WNM together.

Figure 2.1 illustrates a problem intrinsic to this method. For observations of the inner Galaxy (regions closer to the center of the Galaxy than the Sun) this method gives two possible distance estimates for a given object, yielding an uncertainty for the distribution of atomic hydrogen in these regions. It is still possible, though, to calculate the surface density of H I. So far it has been found to be constant up to a radius of about 4 kpc from the center of the Galaxy, and decreasing beyond this distance. The vertical structure of atomic hydrogen is also estimated to be roughly constant with radius.

The distance uncertainty does not exist for the outer Galaxy, where we can make exact distance measurements from 21 cm observations. In that part of the Galaxy, we can discern the spiral arm pattern of the Galactic disk. Until 2008, our Galaxy was thought to have four spiral arms, named Perseus, Cygnus, Carina and Orion after the constellations where they were projected. However, high-resolution observations with the Spitzer telescope, gave significant indications that our Galaxy possesses a bar in the inner parts and only two spiral arms, like most observed barred galaxies (Churchwell et al., 2009). It is also known that atomic hydrogen exists at radii of at least 30 kpc from the center of the Galaxy and that the outer part of the gaseous Galactic disk is warped.

Another important observable of interstellar neutral gas are the fine-structure lines of certain atoms, such as C I, C II, N I, N II, O I, O II and O III, to name a few. Fine-structure interactions are interactions between the orbital momentum of the electrons in an atom and their total spin and for these species, they are mostly found in the far-infrared. These lines are the main coolants of the atomic interstellar medium, as we will explain in Section 2.6.2.

Finally, we can infer the chemical composition of interstellar matter from absorption lines observed in the spectra of stars. We can distinguish the lines coming from interstellar gas from the intrinsic stellar lines because they have a fixed wavelength, unlike the periodically Doppler-shifted lines from the star, and because they are much narrower. The abundance of hydrogen, for example, is calculated by fitting a theoretical profile to the observed Ly α line. Once the hydrogen column density is known, the elemental abundances of heavier atoms are expressed in terms of the hydrogen abundance. If the observed line comes from a species which is expected to be mostly neutral in the atomic ISM, then the procedure is similar to that for Ly α . If more than one ionization state of the element is observed, then the abundance is determined by solving the ionization equilibrium for the observed species.

2.2.1 Molecular Interstellar Gas

Although by far the most abundant molecule in the Galaxy is H_2 , there are many more molecules in the ISM (more than 100 known so far) some of them very complex. We can find molecular emission or absorption due to electronic transitions, like in atoms, but also due to vibrational and rotational transitions, in the spectra of the ISM, of the envelopes of asymptotic giant branch stars and of comets.

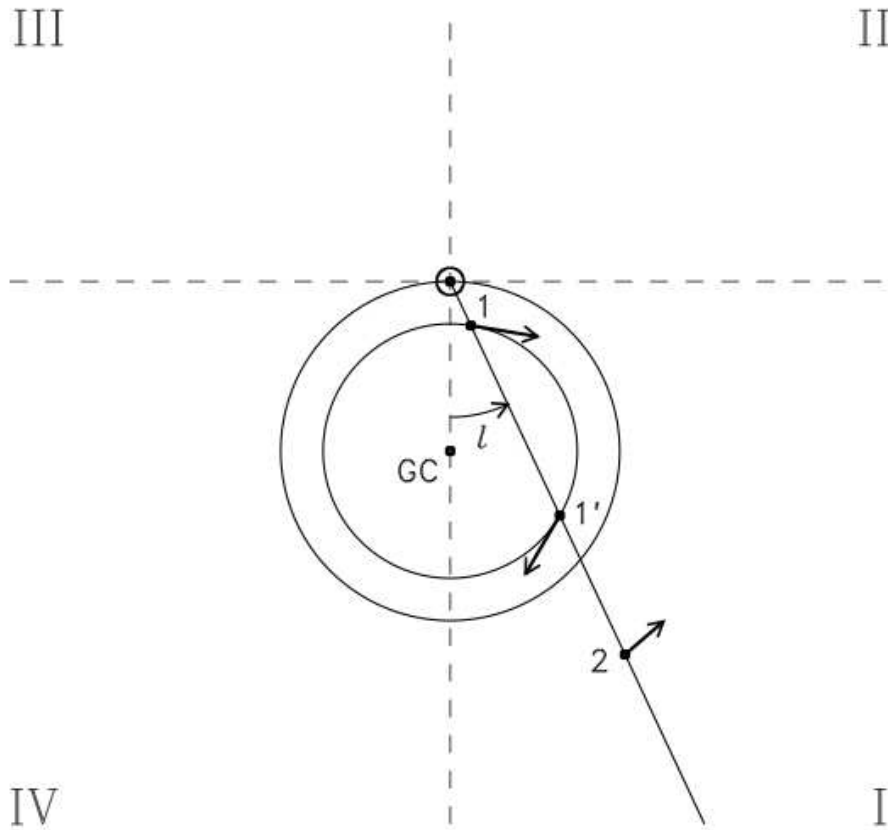


Figure 2.1: Illustration of a line of sight towards the inner galaxy and through the Galactic disk. For a given line of sight velocity, there are two possible distances. (Image Credit: Ferrière (2001))

Vibrational transitions of molecules come from stretching, bending and deformation modes. Each vibrational transition can be further decomposed into rotational transitions, so they appear in spectra as ro-vibrational bands. The typical energies for vibrational transitions are of the order of a fraction of an eV so the bands are observable in the near-infrared. Rotational transitions, on the other hand, have energies of the order of meV and we can usually observe them in sub-mm to cm wavelengths.

Molecular electronic transitions are of the order of a few eV and are generally found in the far-UV. The most important results from such measurements come from H_2 emission observations, owing, of course, to the high abundance of this molecule. The highest intensity lines can yield interstellar H_2 abundances. Comparison of molecular to atomic hydrogen abundances in many lines of sight has shown that, above a gas column density of about $N(\text{H I}) \geq 10^{21} \text{ cm}^{-2}$ interstellar gas is almost entirely molecular. This has important consequences for theoretical models of the Galactic ISM where one needs to include some measure of the molecular

component without explicitly modeling the chemistry of atomic to molecular phase transition.

Ultraviolet observations are possible in relatively diffuse environments, where interstellar extinction from dust is not significant. Nevertheless, most of the molecular gas in our Galaxy is located in large and dense structures, called molecular clouds. These clouds contain a lot of dust due to their high densities, which makes UV observations impossible. This, in combination with the fact that H_2 , being a symmetric molecule, has no permanent moment of inertia and thus no permitted transitions in the radio regime, has led astronomers to seek lines from other molecules as tracers of the internal structure of dense molecular clouds.

The next most abundant molecule in these clouds, which in addition has a rotational transition in the radio regime, is CO. Its $J = 1 \rightarrow 0$ rotational transition at 2.6 mm can be used, in a similar way as the 21 cm line of H I, for mapping the large-scale distribution of dense molecular gas in the Galaxy, since it is unaffected by dust extinction. Such surveys have yielded a very high concentration of molecules in a region of 0.4 kpc radius around the center of the Galaxy, and a ring structure at radii between 3.5 and 7 kpc. It has also been found that molecular gas follows the Galactic spiral pattern very closely in the outer Galaxy and less dominantly so in the inner Galaxy, where the ring structure dominates (–see Figure 2.5). Molecular gas is mostly confined at the midplane of the disk, with a scale height of about 81 pc.

High-resolution CO observations have shown that the mass distribution of molecular clouds is very hierarchical, with large structures containing ever smaller and denser cores. Hydrogen densities in these clouds range from 100 to 10^6 cm^{-3} , organized in an almost fractal structure.

It is widely believed that molecular clouds are gravitationally bound, although there are uncertainties in what defines the limits of a cloud. In any case, that the vast majority of observed molecular clouds are in the process of gravitational collapse. In particular, it is the dense cores within them that give birth to stars. After star formation has started in a cloud, the remaining molecular gas is believed to be quickly photodissociated by the intense radiation from the young stellar objects. The complex subject of star formation from dense molecular cores will not be treated in this thesis.

We will provide some more observational facts about molecular clouds in Chapter 4, and we want to point out here that most of them are still derived from CO observations. Another way to get reliable mass estimates in the densest clouds is from dust extinction itself, a matter we will explain further in Section 2.3, where we will discuss the properties of interstellar dust.

An important class of molecules in the ISM are Polycyclic Aromatic Hydrocarbons (PAHs). These are large molecules, the study of which is important, not only for understanding the chemistry of the ISM, but also for estimating its radiative heating and cooling rates, as we will see in Section 2.6.2. These molecules are believed to be the origin of observed infrared bands. This emission is a fluorescence effect, in which a FUV photon absorbed by the molecule leads to electronic excitations, with the energy re-emitted in the IR through vibrational modes of the molecule.

2.2.2 Ionized Interstellar Gas

The brightest stars in the Galaxy, O type stars, produce large amounts of high-energy photons, which are able to ionize hydrogen and helium around them. The energy required to ionize hydrogen is 13.6 eV, so photons with higher energies (UV wavelengths) will create a region of ionized hydrogen around the star. The remaining energy of photons which produced ionization



Figure 2.2: An example of a dark cloud is the "Pipe" nebula, named after its elongated shape which resembles a smoking pipe. This nebula is currently not star-forming and it has a filamentary, self-similar structure typical of molecular clouds. Located on the sky in the constellation of Ophiuchus, it is a small structure, of about 5 pc in projected length. This image shows dust absorption overlaid on the background starlight. (Image Credit: ESO/Yuri Beletsky)

is deposited in the free electrons of the plasma as thermal energy, effectively heating the gas. The ionized regions around O stars are called H II regions, after the fact that hydrogen in these regions is fully ionized.

From their natural connection to very bright young stars we know that H II regions have the same distribution as O-type stars in the Galactic disk, following the spiral density pattern in the disk midplane and with a vertical scale height of about 80 pc.

The simplest description of an H II region, although not entirely accurate in most cases, is the Strömgen sphere. The Strömgen sphere is defined as a region inside which the number of atom photoionizations by the stellar radiation per unit time is equal to the number of recombinations of the ions with free electrons. Since the absorption of UV photons by neutral hydrogen is very efficient, a Strömgen sphere has very well defined boundaries. Assuming a uniform medium composed entirely by hydrogen, the radius of a Strömgen sphere is given by

$$R_S = 30pc \left(\frac{N_{48}}{n_H n_e} \right)^{\frac{1}{3}} \quad (2.2)$$

where N_{48} is the number of ionizing photons released by the star per unit time, in units of 10^{48} s^{-1} , n_H is the neutral hydrogen number density and n_e is the electron number density.

H II regions produce continuum radiation as well as line emission. The continuum is thermal Bremsstrahlung in radio wavelengths, produced by free electrons as they are decelerated by the electric field of the ions. Thermal Brehmstrahlung can give us information on the temperature of the plasma, which in this case is about 8000 K. Incidentally, the same value can be obtained by theoretical considerations, assuming that photoelectric heating balances radiative cooling inside the ionized sphere surrounding the star. This gas is therefore called "Warm Ionized Medium", to distinguish it from an even hotter phase we know exists in the ISM.

In a wide range of wavelengths, free-bound continuum emission is also produced by the recombinations of free electrons with ions. This process gives rise to characteristic discontinuities, caused by recombinations to a hydrogen energy level. The less probable, but important for metastable atomic levels mechanism of two-photon radiative de-excitation also becomes important for H II regions, especially at wavelengths near 400 nm.

Naturally, we can also observe the permitted recombination lines of H, He and other

elements from H II regions. These lines are very useful for determining dust extinction and elemental abundances of the ionized gas. Due to the low densities in these environments, we can also observe forbidden lines if C, O and other species.

However, not all the ionized gas in the Galaxy is confined in H II regions. Indeed, we can anticipate the existence of diffuse ionized gas in the interstellar medium by raising the assumption of a uniform medium surrounding the star, which enters the calculation of the Strömgen radius. Since the position of the ionization front is inversely related to the gas density, if one side of the surrounding medium is slightly more rarefied, or if the surrounding gas is stratified in density (like the Galactic ISM along the vertical direction), we expect the ionized gas to escape in the surrounding space in the direction of the less dense gas, extending to distances larger than the Strömgen radius given by equation 2.2. This effect is called the "champagne effect". Ionized gas from associations of young massive stars can also escape in surrounding space via the large cavities opened by the combination of their winds. It is not surprising then that, although stars are created in the very dense environments of molecular clouds, ionized gas can be found up to relatively high Galactic altitudes.

The distribution of diffuse interstellar gas has been deduced by the scattering of pulsar signals by the free electrons of the ionized gas, showing that this is actually the case. The interaction of the pulsar photons with the free electrons reduces the group velocity of the pulse proportionally to the wavelength. Then the spread in arrival times of different wavelengths within a pulsar signal will be proportional to the column density of free electrons along the line of sight to the pulsar. If we know the distance to the pulsar independently, we can deduce the number density of free electrons in the diffuse medium. With this method it has been found that the distribution of diffuse ionized gas in the Galaxy comprises a thin, annular component at about 4 kpc from the center in the radial direction, probably connected to the molecular annulus at that distance and a more extended, thick disk, with a Gaussian scale height of at least 20 kpc. The average number density of this medium is of the order of 10^{-3} cm^{-3} .

In addition to the warm ionized gas, there is an even hotter ionized phase of the ISM, usually referred to as the hot interstellar medium (HIM), with a temperature of about 10^6 K , which emits radiation in soft X-rays. This gas comes from supernova explosions when stars reach the end of their lives. It is also produced in large cavities, created by large stellar OB associations. It is therefore always directly related to the star formation rate of a galaxy. In these regions, elements such as oxygen get collisionally ionized to give emission and absorption lines of species such as O VI and O VII. Since interstellar X-ray observations probe emission from distant hot gas superimposed with absorption from intervening clouds, it is difficult to discern the distribution of this hot gas in the Galaxy. We do know, however, that this gas reaches very high Galactic altitudes and that it occupies some 80-90% of the volume in the Galactic disk.

X-ray emitting gas, in particular O VI, has also been associated with structures in the halo of the Galaxy called high-velocity clouds, which were first identified by 21 cm observations. These clouds are moving with velocities of several tens of kilometers per hour and are believed to be falling into the potential well of our Galaxy. The X-ray gas connected to these clouds could be coming from photoionization by a diffuse UV background, or it could be a thermally unstable front between the cold gas contained in these clouds and an even hotter gaseous halo, which could be detectable in soft X-rays in absorption. For a more detailed treatment of this matter, which is outside the scope of this thesis, we refer the reader to Ntormousi & Sommer-Larsen (2010) and references therein.

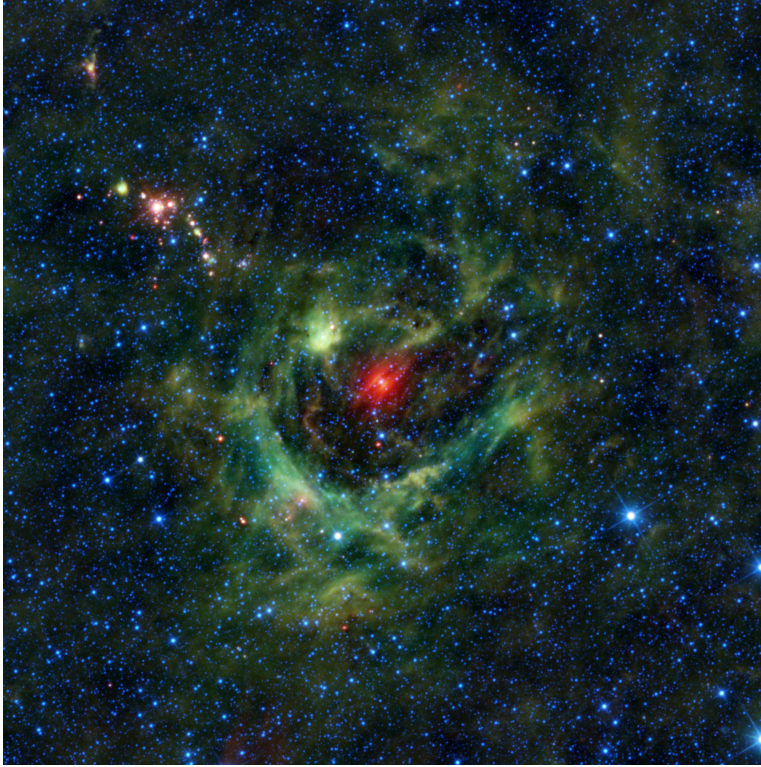


Figure 2.3: The "Shamrock nebula", located at about 10 pc from the Sun, at the outer edge of our local spiral arm. It is a typical example of an HII region, where a central O type star illuminates its parent cloud with strong, ionizing UV radiation. In this case the star is CY Camelopardalis. The image is taken in the infrared band, at wavelengths of 12 and 22 μm , which is emitted by the dust as it gets heated by the central star. (Image Credit: NASA/JPL-Caltech/UCLA)

2.3 Dust

The importance of dust in the physics of the ISM and in the interpretation of astronomical observations in general cannot be overstated. Since dust is very well mixed with the interstellar gas, it is of extreme importance to understand its effects on the observed radiation and take them into account both when analyzing observations and when producing theoretical models of the ISM.

Dust is the main cause of the ISM opacities at wavelengths longer than the Lyman discontinuity. It is also a cause of heavy metal depletion, since it keeps a large portion of the local ISM metals locked up in its grains. In addition, dust is a very important catalyst for many chemical reactions in the ISM. It provides not only a surface on which elements can combine, but also a third body to receive the excess energy from certain chemical reactions. This is one of the reasons why in many regions the dust content is an indication of the gas metallicity.

The alignment of elongated dust grains with the magnetic field of the Galaxy causes the linear polarization of the radiation that passes through the ISM, giving us a means to observe the Galactic magnetic field.

The most straightforward way to observe dust in the Galaxy is by the reddening effect it has on background light sources. From equation 2.1 we know that the difference between the absolute and the observed magnitude of a star depends on the dust extinction along the line of sight. By measuring the magnitude difference between a reddened star and a nearby star of the same spectral type, which is unaffected by the intervening dust cloud, we can calculate the color excess caused by the dust. Since stellar radiation covers a wide range of wavelengths, from this process we obtain the color excess as a function of wavelength. The

resulting curve, called extinction curve, for the ISM shows an increase in extinction with increasing wavelength. This is the reason why dust extinction is also called reddening.

By studying extinction curves we can derive the composition and sizes of interstellar dust grains. For instance, the presence of a "bump" in extinction curves in the UV, around 217nm indicates the presence of graphite particles. Infrared extinction bands, on the other hand, point to the presence of silicates. Absorption by dust is also a strong indicator of the total dust volume, if the optical properties of the dust particles are known.

Dust absorbs FUV photons and re-emits them in the infrared. Most of the electrons excited by the UV photons that hit the dust do not reach the surface of the grain. Their energy is left in the grain, which is thus heated and emits thermally in the infrared. This process has important implications for the heating and cooling of the ISM, as we will see in Section 2.6.2, but it also provides a means of observing the structure of the gas with space observatories which are unaffected by the Earth's atmosphere. A spectacular image of the structure of the ISM as traced by dust emission in the infrared, as seen by the Herschel satellite, is shown in Figure 2.4.

It follows from simple considerations of the way a solid particle can interact with electromagnetic radiation, that the strongest interaction will happen for particles of similar size to the incident wavelength. The fact that extinction curves depend on a wide range of wavelengths indicates that interstellar dust particles have a distribution of sizes. Although the shape of the distribution of dust particle sizes is still debated, the grain radii are known to vary between about 0.005 and 1 μm .

Solid particles do not only absorb, they also scatter background light. Scattering is dominated by the largest dust grains and is what creates the "reflection nebulae", usually blue-colored reflections of starlight by a cloud containing dust.

Although the mechanisms by which dust can be destroyed are numerous, shocks and ionizing photons being ubiquitous in the ISM and destructive for these particles, the origin of dust in the ISM is still poorly understood. The standard picture of grain creation is from planetary nebulae and from cool stellar winds. In both cases, the temperature of the gas should drop enough for the first nucleation to occur, namely for the bonds between particles to switch from strong molecular to weaker, inter-molecular bonds. For this to happen, the metallicity of the gas should be high enough and its cooling rate should be fast. After nucleation has begun, inter-particle collisions take over the growth of the grains. However, it is not clear if the production rate from these mechanisms is enough to account for all interstellar dust, given the rate at which shocks and supernovae can destroy it Salpeter (1977); Kochanek (2011); Draine (2011). On the other hand, the apparent element depletion inside dense molecular clouds could indicate that they are a site where dust could be forming.

2.4 Cosmic Rays

Mostly for historical reasons, we refer to energetic charged particles reaching the Earth from space as cosmic rays. These particles were initially thought to originate from the Earth itself or from the atmosphere, until balloon experiments proved their extraterrestrial origin.

These particles are injected into the ISM by supernova explosions and by flares or coronal mass ejections from late-type stars. Actually, the lowest-energy cosmic rays that reach the Earth do come from the closest such star to the Earth, the Sun. Cosmic rays are accelerated to the energies at which we observe them by turbulent magnetic fields and by crossing supernova

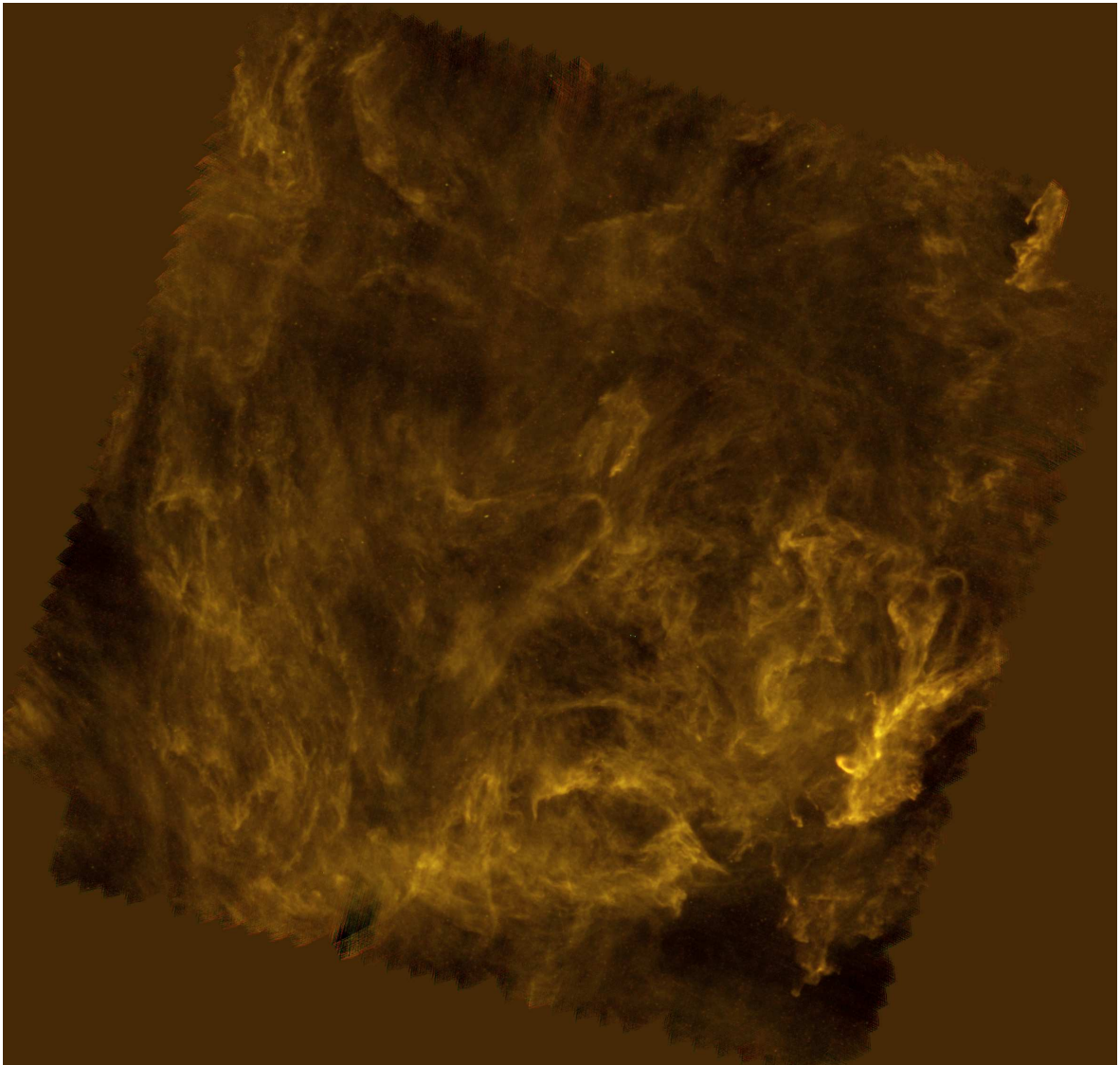


Figure 2.4: Dense gas filaments in Polaris, as seen by the Herschel satellite at infrared wavelengths 250, 350 and 500 μm , coming from dust and PAHs.
(Image credit:ESA/Herschel/SPIRE/Ph. André (CEA Saclay) and A. Abergel (IAS Orsay).)

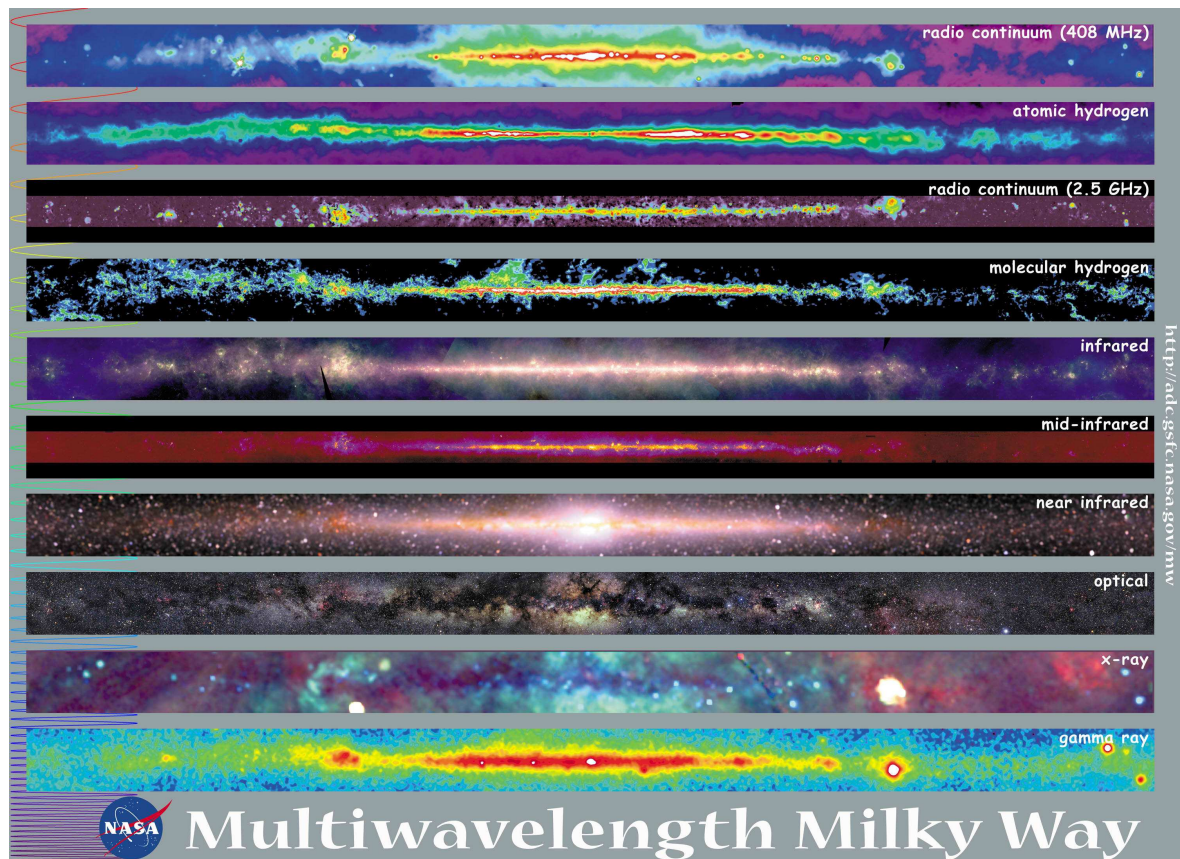


Figure 2.5: A collection of images of the Milky Way in 10 different wavelength bands. From top to bottom: **1.** 408 MHz radio continuum, mostly synchrotron emission as electrons move in the Galactic magnetic field. **2.** 21 cm atomic hydrogen emission. **3.** 2.4-2.7 GHz radio continuum, tracing hot ionized gas through the synchrotron emission of free electrons. **4.** $J = 1 \rightarrow 0$ CO emission in the radio, tracing the Galactic molecular gas. **5.** Composite image of mid- and far-infrared, principal tracer of interstellar dust emission. **6.** Mid-infrared, coming from Polycyclic Aromatic Hydrocarbons. **7.** Composite near-infrared image, probing unobscured radiation from cool star. **8.** Optical light, where we can see the regions obscured by dust. **9.** X-ray emitting hot gas. Cold clouds appear as shadows in this image. **10.** Gamma rays, produced by cosmic ray collisions with hydrogen atoms in the Galaxy and by the scattering of lower energy photons to higher energies as a result of collisions with cosmic ray electrons. (Image and caption credit: NASA Multiwavelength Milky Way project (<http://mwmw.gsfc.nasa.gov/>) and references therein)

or other types of shocks as they propagate in the Galaxy.

Given their observed constitution and energy distribution, we could say a typical cosmic ray particle is a proton of energy about 1-10 GeV. Protons actually make up about 85 % of the cosmic ray particles, the rest being alpha particles and 3% heavier nuclei. Cosmic rays also contain electrons, positrons and nuclei of elements such as Li, Be and B, which originate from their interaction with ISM particles. Cosmic ray energies range from 10^9 eV to values as high as 10^{20} eV, the latter termed ultra-high energy cosmic rays (UHECR). Their distribution roughly follows a broken power-law behavior, starting from a slope of -2.75, becoming steeper (slope=-3) after an energy of about 10^{15} eV and flatter again, with a slope of -2.5 after about 10^{18} eV.

The flow of cosmic rays to the Earth, especially at low energies, is regulated by the magnetic field of the Sun. The solar wind carries a significant magnetic field, which can trap these particles before they reach our atmosphere. This makes the exact shape of the cosmic ray energy spectrum quite uncertain. Cosmic rays also follow the magnetic field of the Galaxy, which makes them interesting tracers for studying its morphology (–see also Section 2.5).

The most important role played by cosmic rays in the ISM is that they provide a source of pressure. They are also the main cause of ionization in very dense environments, such as molecular clouds. The small degree of ionization they provide inside molecular clouds is of extreme importance for the coupling of the gas to the magnetic field.

2.5 Magnetic Fields

Cosmic rays gyrate around the field lines of the Galactic magnetic field, emitting synchrotron radiation (– see Figure 2.5). This radiation is an important probe of the Galactic magnetic field, if certain assumptions are made for the cosmic ray number densities in the Galaxy. From such modeling we know that the Galactic field on the plane of the disk can be decomposed into a structured component, following the spiral density wave pattern, and a turbulent component, with random direction. In the vertical direction it forms two disks: a thin disk of scale height of about 150 pc, and a thick disk of scale height about 1500 pc.

Synchrotron emission interpretations are very uncertain since they depend on assumptions of the cosmic ray number densities and of the magnetic field strength. An independent measure of the strength of the magnetic field that can be used in such estimates, at least for its component along the line of sight to the observer, is the Zeeman splitting of certain atomic levels. Zeeman splitting is the result of the interaction of the magnetic moment of the electrons in an atom with an external magnetic field. In the Galaxy this method can be applied to the 21 cm hydrogen line (with some adjustments to account for insufficient resolution that we will not discuss here). This of course renders it biased towards the densest regions. From Zeeman splitting measurements we know that the Galactic magnetic field has a typical strength of a few μG .

When a linearly polarized electromagnetic wave propagates through a magnetized plasma, its plane of rotation rotates by an angle which is proportional to the square of its wavelength. This phenomenon, called Faraday rotation, can also be used to probe the magnetic field of the Galaxy, although only in ionized regions.

The role played by magnetic fields in the physics of the ISM is, on large scales, to confine interstellar matter by providing a net pressure that can balance the self-gravity of the gas. It also traps cosmic ray particles in the Galaxy, which is an additional source of pressure.

In smaller scales, magnetic fields regulate the expansion of supernovae and superbubbles, as well as the dynamics of individual clouds, since there is a sufficient degree of ionization in all ISM phases for magnetic fields to be coupled to the gas. Magnetic fields have also been argued to support molecular clouds against gravitational collapse.

2.6 The system as a whole

In the previous Sections of this Chapter we introduced the observed properties of the different constituents of the Interstellar Medium separately. This is mainly justified by their different manifestations in observations and by the different physical state of each. Nonetheless, it has probably become evident to the reader that the different phases of the ISM not only interact with each other, but they also regulate the behavior of the Galaxy as a system.

Stars, especially massive ones, are the trigger of most of the processes in the ISM. Young stars, especially of early types, expel large amounts of matter in very energetic winds. They also provide large amounts of ionizing radiation, heating and ionizing the ISM around them. The ionization either leads to the formation of well-defined H II regions, or escapes to form the diffuse ionized medium.

Supernova explosions inject energies of the order of 10^{51} ergs to the gas surrounding the star. What is more, in large associations of O and B stars, the combination of the stellar winds and supernova explosions creates enormous cavities of hot gas, which compress the gas around them. Such shells, being subject to cooling from various processes that we will explain in the following Chapters of this thesis, can fragment to give cold gas. However, the violent passage of such a shock from a clouldlet can instead evaporate it, or trigger it to collapse gravitationally and give new stars.

2.6.1 Models of the multi-phase ISM

The different phases of the atomic ISM seem to be in rough pressure equilibrium with each other. This points to a fluid instability known as Thermal Instability (–see Section 3.2.3 for a detailed description of the instability), as a formation mechanism for the CNM and the WNM phases.

This instability happens when the heating-cooling rate equilibrium curve on the density-temperature plane of the gas shows wide plateaus, separated by steep steps. An example of such an equilibrium curve is shown in Figure 2.6. This gives two stable equilibria on either side of an unstable equilibrium point, defined by a line of constant pressure, for instance, like the one shown in Figure 2.6. The region above the curve is where cooling is stronger than heating and the region below the curve is where heating is stronger than cooling. When gas is perturbed from the unstable equilibrium point to the region above the curve by, say, a compression, cooling drives it to cool and condense further, until it reaches equilibrium again, to the equilibrium point on the high density regime. An equivalent process happens to drive gas that has been perturbed to lower densities and drive it to the plateau on the low density regime. Depending on the exact shape of the equilibrium curve and the positions of the plateaus the densities and temperatures of the two phases can be different. This mechanism for the formation of phases of the ISM was proposed by Field (1965). However, we know that the ISM possesses at least one more gas phase, the hot component, which is very important for its dynamics, as well as for its enrichment in metals, but it is not included in this model.

The inclusion of the third component in a dynamical model of the ISM was first proposed by McKee & Ostriker (1977). In their model, the ISM is composed of spherical clouds, each of them composed of a cold neutral core and surrounded by two envelopes, a warm neutral medium immediately outside the cold core and a warm ionized corona as the outer surface of the cloud. The cold clouds are assumed to have a very low filling factor, of about 0.02-0.04. Their ionized coronas have a filling factor of 0.2, while practically the whole volume of the ISM, with filling factors of about 0.7-0.8, is composed by a hot dilute medium, created by supernova explosions. In fact, supernova explosions regulate the behavior of the ISM in this model, compressing and sometimes evaporating the cold clouds. In their view of the ISM, the total mass of the gas is conserved and the phases are in pressure equilibrium. A schematic view of this model is shown in Figure 2.7.

Although this model significantly improved our understanding of the ISM physics, mainly by introducing the hot component, we now know that the neutral clouds are far from spherical (Figure 2.2) and that the hot phase of the ISM actually has almost double the pressure of the other phases and is thus sometimes driven outside the Galactic disk. An improved model for the ISM, where the cold clouds appear as "blobby sheets" rather than spheres, was presented by Heiles & Troland (2003), based on their observations.

2.6.2 Cooling and Heating Processes of the Interstellar Gas

This Subection is in effect a summary of Wolfire et al. (1995). We refer the reader to this paper for further details on the calculation of the rates.

One very important ingredient for understanding the formation of phases, by the mechanism described briefly in the previous subsection, is the net cooling and heating of the gas as a function of its density and temperature. The combination of all possible cooling and heating paths of the gas will give an equilibrium curve like the one shown in Figure 2.6, which predicts the densities and temperatures of the different phases of the gas. Although we have mentioned the possible heating and cooling mechanisms on the ISM in passing, here we explain them in more detail, with a focus only on the atomic phase of the ISM. The heating and cooling rates of the molecular phase, although of extreme importance for the study of the physics of molecular clouds, are outside the scope of this thesis.

Possibly the most important heating source of the atomic gas is photoelectric emission from small dust grains and large molecules, such as PAHs. To remind the reader this well-known phenomenon, the photoelectric effect happens when a photon carrying an energy larger than the work function of a material is absorbed by this material. Then it can give this energy to an internal electron, leading to the ejection of this electron. In the case of dust grains, the excess energy is mostly consumed in heating the grain, since most electrons liberated by UV photons do not reach the surface of the solid. However, for the 10% of electrons that do escape from the grain, the rest of the energy of the photon is available for heating the gas. The resulting heating rate from this process is

$$n\Gamma_{phot} = 10^{-24}n\epsilon G_0 \quad (2.3)$$

in $\text{ergs cm}^{-3} \text{ sec}^{-1}$. ϵ is the fraction of FUV photons absorbed by grains that is converted to gas heating and G_0 is the FUV flux in $1.6 \times 10^{-3} \text{ ergs cm}^{-2}$. Γ_{phot} is called the heating function for this process and n is the number density of gas atoms.

ϵ is not a constant, but rather a function of temperature and electron density. It depends on the ionization rate divided by the rate at which electrons recombine on the surface of the

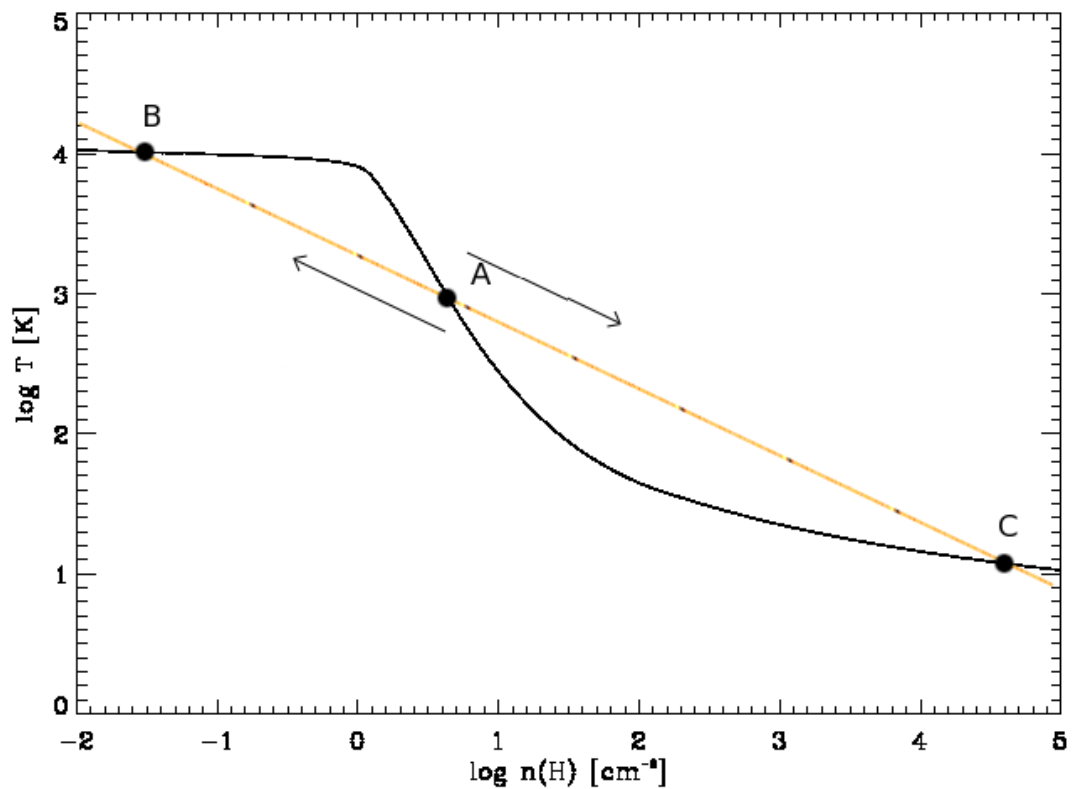


Figure 2.6: Thermal instability mechanism. The cooling-heating equilibrium curve as a function of density and temperature, assuming the cooling and heating rates described in the text, is plotted as a black curve and a straight line indicating a constant pressure curve is shown in orange. Gas parcels perturbed from the unstable regime A on the curve towards higher densities will condense further until they reach the stable equilibrium C. In the same way, a volume of gas heated from A to higher temperatures or lower densities will continue heating and expanding until it reaches equilibrium point B. We have then, the formation of two gas phases in temperatures and densities given by points B and C.

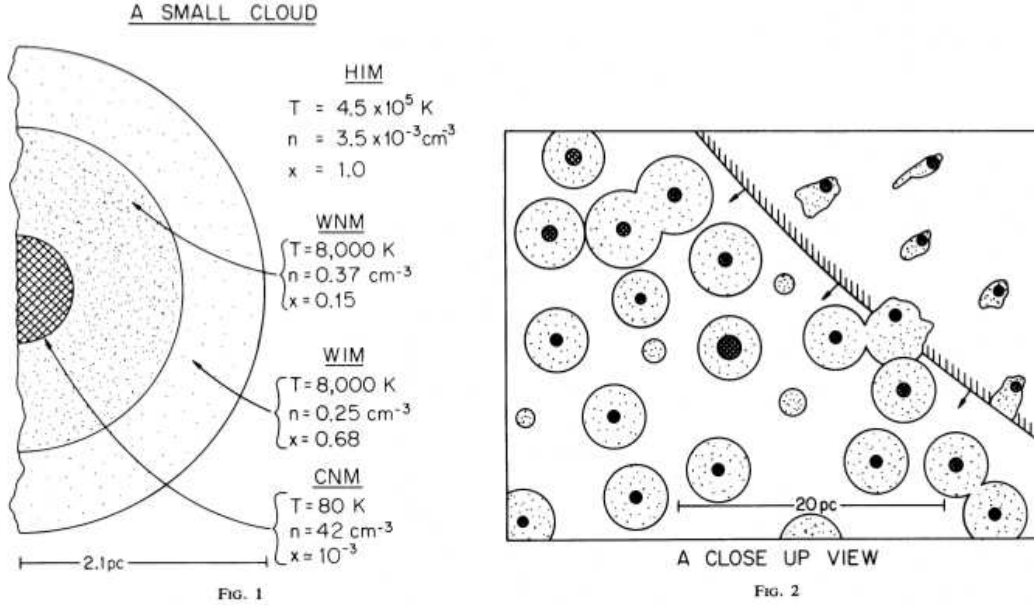


Figure 2.7: A schematic view of the ISM by McKee & Ostriker (1977). On the left (Fig. 1 of that paper), a cross-section of a typical cloud in their model. It is composed by a neutral atomic core, enveloped by a warm neutral and a warm ionized corona. The whole structure is immersed into the hot ionized medium. On the right (Fig. 2 of that paper), a small-scale view of the passage of a supernova shock wave, coming from the upper right, from a region of the ISM filled with clouds such as the one shown on the left. A fraction of these clouds will be evaporated.

grains. The maximum efficiency happens, of course, for low temperatures, when the grains are mostly neutral.

The shape of the FUV spectrum has not been found to affect the resulting heating function a lot, as long as the total flux remains constant. What does affect this heating rate appreciably is, of course, the distribution of grain sizes. Usually, the distribution is assumed to be a power-law with a slope of about -3.5, based on models that take into account the observed dust emission.

The heating rate of the gas by photoelectric emission from dust and PAHs is shown in Figure 2.8 as the top dashed line. It is evidently the most important heating rate in the local ISM. However, as we will explain shortly, under certain circumstances the photoelectric effect can result in a net cooling of the gas.

Additional heating of the ISM comes from cosmic ray ionization of the gas and from diffuse X-ray radiation. Cosmic rays can ionize the gas to appreciable degrees, with an ionization value usually adopted for the ISM being $n\zeta_{CR} = 1.8 \times 10^{-17} n \text{ cm}^{-3} \text{ sec}^{-1}$. After ionization, the excess energy is available for heating. Assuming a power-law distribution for the momenta of cosmic rays, which, as we have seen in Section 2.4, is a well-justified assumption, and taking into account also secondary ionizations of H and He, the heating rate from this process is

$$n\Gamma_{CR} = n\zeta_{CR}E_h(E, n_e/n) \quad (2.4)$$

where $E_h(E, n_e/n)$ is the heat provided to the gas by each electron of energy E. This function depends on the electron fraction in the gas and the energy of the electron and is provided in the Appendix of Wolfire et al. (1995).

A similar process gives the heating rate of the gas from soft X-rays. Soft X-rays in the Galaxy are produced by energetic stellar feedback, mostly from young massive stars, although at the highest energies an extragalactic X-ray component dominates, coming mainly from a hot intergalactic medium. Without going into the specific details of the calculation, we quote here the heating function calculated for this heating mechanism:

$$n\Gamma_{XR} = 4\pi n \sum_i \int \frac{J_\nu}{h\nu} e^{-\sigma_\nu N_w} \sigma_\nu^i E_h(E^i, n_e/n) d\nu \quad (2.5)$$

where the summation is assumed over all elements which experience primary ionization. N_w is the column density of neutrals, hence the factor $e^{-\sigma_\nu N_w}$, which accounts for an absorbing layer of neutral, warm interstellar gas, with the cross-section σ_ν for absorption in frequency ν taking into account the elemental abundances. n_e/n is the ionization fraction. J_ν , the assumed X-ray flux spectrum, is calculated by including three X-ray components: A single-temperature component from nearby sources, a single-temperature component from largest distances which has suffered absorption from interstellar clouds and an extragalactic power-law emission component. In Figure 2.8, heating from X-ray ionizations is the second most important heating mechanism up to hydrogen number densities of about 10^3 cm^{-3} , followed by cosmic ray ionization. At higher densities an important source of heating comes from the photoionization of C I.

It has already been mentioned in earlier Sections of this Chapter that the most important coolants of the atomic ISM, especially in the low-temperature regime, are the fine structure lines of species such as O I and C II (–see Figure 2.8).

Important energy losses, mostly in the low-density regime, come from the recombination of electrons onto small dust grains and PAH molecules, a process already mentioned when discussing heating mechanisms. When the thermal energy of the electrons that recombine on the grains exceeds the energy of the electrons being ejected, then the net effect is an energy loss from the gas to the grains. It is clear that this effect is important at high temperatures, when the electron thermal energy, kT , is larger than the typical 1 eV carried by the photoelectrically ejected electrons. When modeling the gains and losses of the gas caused by the photoelectric effect, the heating and cooling rates are calculated separately, so the net heating or cooling is defined as the difference between the two. The cooling by recombination of photoelectric electrons is shown in Figure 2.8 as a solid black line.

In addition to the fine-structure lines, cooling can also happen due to emission in metastable or resonance lines. In particular, the collisional excitation of the Lyman α line can contribute to the energy losses of the gas in the highest temperature regime.

Figure 2.8 summarizes the cooling and heating processes that we have taken into account in this work. In calculating these rates we have assumed that the lines are optically thin and that dust extinction is not important. These assumptions are increasingly inaccurate as we move towards the high density regime, but, since we are only interested in the transition from warm to cold gas, they provide an adequate description of the average cooling and heating rates of the gas in this regime. The gas has been assumed to have a constant ionization degree in the calculation of the rates. The resulting cooling and heating curve for the parameters we have used is shown in Figure 2.6. The abundances used in this calculation are roughly solar.

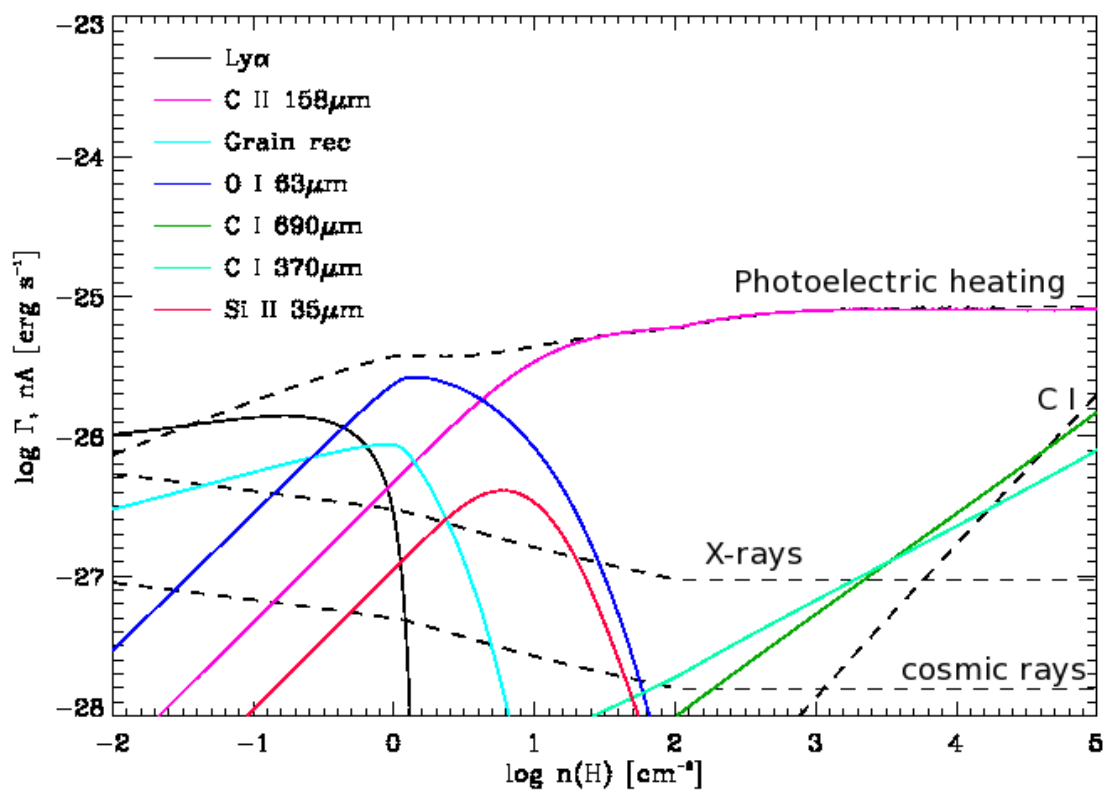


Figure 2.8: Cooling (solid lines) and heating (dashed lines) rates as a function of density, assuming local ISM conditions and optically thin lines. Dust absorption is not assumed to be important for the densities and the radiation frequencies considered.

2.6.3 The modern view of the ISM: the role of turbulence

As mentioned in Section 2.6.1, the inclusion of a third, hot phase of the ISM was proposed by McKee & Ostriker (1977) to account for cloud destruction and to count as a large volume-filling fluid. However, winds and supernova explosions from massive stars introduce a much more significant ingredient in the complex system of interactions in the ISM: they are a source of mechanical energy and, as such, the drivers of turbulence.

Turbulence, which will be treated in somewhat more detail in Section 3.4 as a consequence of the equations of hydrodynamics, is a term to describe the coupling of different scales of a fluid through the exchange of energy. It is characterized by a stochastic behavior and the replacement of the local properties of a flow by statistical laws. In principle, one could roughly describe a turbulent flow by the existence of curved shocks and eddies, appearing and disappearing unpredictably, almost chaotically.

In this context it is therefore understood that a large-scale energy injection as violent as a supernova explosion or combined feedback from young OB stars will act as the beginning of an energy cascade, creating smaller-scale eddies and shocks in the ISM. Although theoretically such models have been proposed since a long time (ie de Avillez & Breitschwerdt (2004)), and the turbulent nature of all the phases of the ISM has been evident in observations for even longer (Schneider & Elmegreen (1979); Lada et al. (1999); Hartmann (2002); Lada et al. (2007); Molinari et al. (2010), see also Figure 2.4 for a representative image of interstellar turbulence) it is very difficult to verify that the injection scale of interstellar turbulence has a supernova origin.

Turbulence in the warm atomic phase of the ISM is thought to be roughly sonic (Verschuur, 2004; Haud & Kalberla, 2007), meaning that the root mean square velocities of the gas are of the order of its sound speed (~ 10 km/sec) while in the cold molecular phase it is thought to be supersonic, reaching velocities of 1-5 km/sec, while the sound speed in these clouds is roughly 0.2-0.5 km/sec (–see also Section 4.1 and references therein). This has important implications not only for global models of the Galactic ISM, but also for the star formation process, which happens exclusively in molecular clouds.

Interstellar turbulence is a very efficient mechanism for mixing newly-produced metals from supernovae and stellar winds and dust in the gas. These elements can then participate in a new cycle of star formation. The velocity dispersion in the diffuse phase of the ISM has a stabilizing role against the global gravitational instability of the Galaxy. Inside molecular clouds, the transition scale from supersonic to transonic or subsonic motions is probable what sets the scale of prestellar cores (Walch et al., 2011a), thus deciding the typical mass of a protostellar object. It is therefore very useful to study the properties of interstellar turbulence and look for its drivers at different scales.

The fact that turbulence is maintained at the sonic level for the diffuse phase of the ISM is consistent with a picture in which the violent, evidently supersonic shocks from the drivers, possibly supernova explosions, distribute their energy to smaller scales through a cascade, until it is finally viscously dissipated. The root mean square velocity of such a flow can be proven to fall to sonic velocities very rapidly. The dissipation rate for sonic turbulence being much slower, such a turbulent flow can be maintained for many crossing times, in this case, many Galactic rotation times.

However, the true puzzle in the studies of interstellar turbulence is what maintains the supersonic velocities inside molecular clouds. Such supersonic motions should die out very quickly, as we explained before, so there must be a process at molecular cloud scales which

keeps driving turbulence in their interior. Star formation, through protostellar outflows has been proposed as a possible driving mechanism. The formation scenarios of the clouds themselves, however, very often invoke dynamical processes, which could also trigger turbulent motions in the formed structures. This subject is analyzed addressed in detail in Section 4.1, as part of the motivation for this work; this thesis is partially aimed at explaining the origin of turbulence in molecular clouds by proposing a very dynamical model for their formation.

Principles of Hydrodynamics

3.1 The equations of hydrodynamics

The work in this thesis can be essentially described as solving the equations of hydrodynamics numerically, for different boundary and initial conditions. It is therefore very important that we introduce these equations and some of their applications relevant to the phenomena we will encounter in the following Chapters.

The equations of hydrodynamics provide a macroscopic description of the behavior of a fluid. This means that the length and time scales of the system considered are much larger than those of the interactions between individual atoms or molecules. In practice, we are allowed to use this description of a fluid when the mean free path of the particles is much smaller than the size of the system under study. For all of the problems treated here, hydrodynamics is a more than sufficient approximation.

In hydrodynamics, the evolution of certain variables, representative of the state of the gas, is expressed as a function of space and time. In particular, we follow the velocity of the fluid, $\mathbf{v}(\mathbf{r}, t)$ and any two thermodynamic quantities, usually the density $\rho(\mathbf{r}, t)$ and the pressure $p(\mathbf{r}, t)$, from which the rest of them, such as the temperature, can be derived.

In the following Sections the equations of hydrodynamics are derived from the conservation of mass, energy and momentum. We will refer to small volumes in the fluid as fluid elements. Again, these volumes may be considered infinitesimally small for the sake of the mathematical derivation, but they are always large enough to contain a very large number of atoms or molecules and the equations of hydrodynamics are always valid.

3.1.1 The equation of continuity

The first equation we are going to derive expresses the conservation of mass in the system. Considering a volume element dV of a larger volume V_0 containing the fluid, the total mass in the system can be expressed as $\int \rho dV$, where ρ is the density as a function of position and the integral is taken over the volume V_0 .

Defining $d\mathbf{n}$ to be a vector with direction normal to the surface of the fluid element and magnitude equal to the area of this surface, the mass flux through this surface per unit time is equal to $\rho \mathbf{u} \cdot d\mathbf{n}$, where \mathbf{u} is the fluid velocity vector. We consider $d\mathbf{n}$ to be positive in

The contents of Section 3.1 are from the first chapter of Landau & Lifshitz (1959).

the outward direction, so that the flux is positive when material is leaving the volume and negative when material is entering the volume. Then the total flux of mass out of the volume V_0 is

$$\oint \rho \mathbf{u} \cdot d\mathbf{n} \quad (3.1)$$

where the integration is over the entire surface enclosing the volume V_0 . The mass flux outside the volume causes a decrease in the total mass contained in V_0 , which is equal to

$$-\frac{\partial}{\partial t} \int \rho dV \quad (3.2)$$

By equating equations 3.1 and 3.2, we get

$$\oint \rho \mathbf{u} \cdot d\mathbf{n} = -\frac{\partial}{\partial t} \int \rho dV \quad (3.3)$$

and replacing $\oint \rho \mathbf{v} \cdot d\mathbf{n}$ by its equivalent $\int \nabla(\rho \mathbf{v}) dV$ we get the equation of continuity

$$\frac{\partial \rho}{\partial t} + \nabla(\rho \mathbf{u}) = 0 \quad (3.4)$$

where the integral has been dropped, since this equality must hold for any volume in the fluid.

3.1.2 The force equation

The equation of force balance, in effect the equation of motion of the fluid, is also called the Euler equation, after L. Euler who derived it first.

Considering, as before, a volume element dV in a fluid of volume V_0 , we can express the total force acting on the fluid as the integral of the pressure over the surface enclosing the volume:

$$-\oint p d\mathbf{n} = -\int \nabla p dV \quad (3.5)$$

By equating this force to the change in momentum of the fluid element, we get

$$\rho \frac{d\mathbf{u}}{dt} = -\nabla p \quad (3.6)$$

The derivative $d\mathbf{u}/dt$ is here the total derivative of the velocity. This means that it carries the information on both the change of the velocity of the fluid in a given point in space after a time dt , and the change in velocity experienced by the fluid element because it traveled a distance $d\mathbf{r}$, to a different point of the fluid. To express this information explicitly, we can write

$$\left(\frac{\partial \mathbf{u}}{\partial t} \right) dt \quad (3.7)$$

namely the change in velocity with time when the spatial coordinates, say x , y and z for a Cartesian description, are held constant. Then the second part of the derivative, which is the

part expressing the change in velocity due to the change in coordinates, can be written as

$$dx \frac{\partial \mathbf{u}}{\partial x} + dy \frac{\partial \mathbf{u}}{\partial y} + dz \frac{\partial \mathbf{u}}{\partial z} \quad (3.8)$$

which is equal to $(d\mathbf{u} \cdot \nabla)\mathbf{u}$. So we have

$$d\mathbf{u} = \left(\frac{\partial \mathbf{u}}{\partial t} \right) dt + (d\mathbf{u} \cdot \nabla) \mathbf{u} \quad (3.9)$$

If we divide both sides by dt we can substitute this expression for the total derivative into equation 3.6 and obtain:

$$\frac{\partial \mathbf{u}}{\partial t} + (\mathbf{u} \cdot \nabla) \mathbf{u} = -\frac{1}{\rho} \nabla p \quad (3.10)$$

Equation 3.10 is the Euler equation. Additional terms are usually included in the right-hand side of the equation to account for other forces that may be acting on the fluid, such as gravity.

Here the Euler equation was derived assuming that all the changes in pressure around the fluid element are consumed in changing its momentum. In other words, we have assumed no energy losses due to viscosity or other dissipation mechanisms. This form of the equations of hydrodynamics, when thermal conductivity and viscosity are considered to be negligible, is called ideal hydrodynamics and the fluids with these properties are called ideal fluids.

Assuming a negligible thermal conductivity is equivalent to saying there is no heat exchange between different parts of the fluid. In other words, the motion of a fluid element is adiabatic. This condition can be expressed in terms of conservation of the entropy s of the fluid: $ds/dt=0$

$$\frac{\partial s}{\partial t} + \mathbf{u} \cdot \nabla s = 0 \quad (3.11)$$

which, in combination with the equation of continuity 3.4, gives an equivalent equation of continuity for the entropy in the fluid:

$$\frac{\partial s}{\partial t} + \nabla(\rho s \mathbf{u}) = 0 \quad (3.12)$$

If we consider that, at some initial instant the fluid had the same entropy everywhere, equation 3.12 becomes much simpler: $s = \text{constant}$.

3.1.3 The energy equation

The total energy of a fluid element, assumed to be fixed in space, can be expressed as

$$\frac{1}{2} \rho v^2 + \rho \epsilon \quad (3.13)$$

where ϵ is the internal energy per unit mass.

The change of the kinetic energy of the fluid with time can be written:

$$\frac{\partial}{\partial t} \left(\frac{1}{2} \rho v^2 \right) = \frac{1}{2} v^2 \frac{\partial \rho}{\partial t} + \rho \mathbf{u} \cdot \frac{\partial \mathbf{u}}{\partial t} \quad (3.14)$$

In equation 3.14 we can replace the first term of the right-hand side from the continuity equation, 3.4 and the second term from the Euler equation, 3.10. Then we obtain:

$$\frac{\partial}{\partial t} \left(\frac{1}{2} \rho v^2 \right) = -\frac{1}{2} v^2 \nabla (\rho \mathbf{u}) - \mathbf{v} \cdot \nabla p - \rho \mathbf{u} \cdot (\mathbf{u} \cdot \nabla) \mathbf{u} \quad (3.15)$$

In equation 3.15 we can replace the term $\rho \mathbf{u} \cdot (\mathbf{u} \cdot \nabla) \mathbf{u}$ with $\frac{1}{2} \mathbf{u} \cdot \nabla \nabla^2$. If we define w as the heat function per unit mass, then $dw = Tds + Vdp$. By replacing $V = 1/\rho$, ∇p can be written as $\rho \nabla w - \rho T \nabla s$. Thus we get for the kinetic energy of the volume element:

$$\frac{\partial}{\partial t} \left(\frac{1}{2} \rho v^2 \right) = -\frac{1}{2} u^2 \nabla (\rho \mathbf{u}) - \rho \mathbf{u} \cdot \nabla \left(\frac{1}{2} u^2 + w \right) + \rho T \mathbf{u} \cdot \nabla s \quad (3.16)$$

The change in the internal energy of the fluid element with time, $\partial(\rho\epsilon)/\partial t$ can be derived from the first law of thermodynamics:

$$d\epsilon = Tds - pdV = Tds + \frac{p}{\rho^2} d\rho \quad (3.17)$$

and, since $\epsilon + p/\rho = \epsilon + p dV$ is just the heat function per unit mass w , we have

$$d(\rho\epsilon) = \epsilon d\rho + \rho d\epsilon = w d\rho + \rho T ds \quad (3.18)$$

where we have also used $V = 1/\rho$ and $dV = -d\rho/\rho^2$. So we can write for the change in the internal energy of the fluid:

$$\frac{\partial(\rho\epsilon)}{\partial t} = w \frac{\partial\rho}{\partial t} + \rho T \frac{\partial s}{\partial t} = -w \nabla(\rho \nabla) - \rho T \mathbf{u} \cdot \nabla s \quad (3.19)$$

where equation 3.12 has been used to replace $\partial s/\partial t$.

Combining equations 3.16 and 3.19 we get

$$\frac{\partial}{\partial t} \left(\frac{1}{2} \rho u^2 + \rho\epsilon \right) = - \left(\frac{1}{2} u^2 + w \right) \nabla(\rho \mathbf{u}) - \rho \mathbf{u} \cdot \nabla \left(\frac{1}{2} u^2 + w \right) \quad (3.20)$$

and finally

$$\frac{\partial}{\partial t} \left(\frac{1}{2} \rho u^2 + \rho\epsilon \right) = -\nabla \left[\rho \mathbf{u} \left(\frac{1}{2} u^2 + w \right) \right] \quad (3.21)$$

Equation 3.21 can be understood as the conservation of energy in each volume element as it moves in the fluid, so that the energy carried by a fluid element is $\frac{1}{2} u^2 + w$.

3.2 Hydrodynamical Instabilities Related to Shell Fragmentation

An instability is defined in a physical system as the unbounded growth of initially small perturbations imposed on an equilibrium state. Fluid instabilities are many times identified by the morphology of the system on which they are developing.

In the following Sections we will illustrate fluid instabilities relevant to the expansion and collision of shock waves, such as the Non-linear Thin Shell Instability (NTSI), the Kelvin-Helmholtz Instability (KH) and the Thermal Instability (TI).

We will not provide the full derivation of the perturbation equations or the solutions here, since such a lengthy analysis is outside the scope of this thesis. We will rather introduce the methodology and the assumptions that go into deriving the results, which are essential in order to fully understand the results of our work, contained in the following Chapters. The rigorous derivations of the instabilities can be found in the references mentioned in the text.

3.2.1 The Non-linear Thin Shell Instability

This instability is very similar to the well-known Rayleigh-Taylor instability, which occurs when a dense fluid is accelerated by a more rarefied fluid. In this case, however, the instability occurs without the involvement of gravity, when the surface of a shock, bounded on one side by thermal pressure and on the other by ram pressure, is perturbed by a ripple.

Let the spherical shock under consideration have an outer radius R_s and a thickness h , so that, the inner radius denoted by R_i , $h = R_s - R_i$. The shock is expanding with a velocity V_s in a uniform medium of density ρ_E and is driven by a medium of thermal pressure P_i and negligible density (infinite sound speed). At this point we introduce the thin-shell approximation, which significantly simplifies the derivation of the equations:

$$\frac{h}{R_s} < kh \ll 1 \quad (3.22)$$

$$\frac{\partial}{\partial t} \ll \frac{c_s}{h} \quad (3.23)$$

where k is the wavenumber of the perturbation. Condition 3.23 essentially says that we want the evolution of the perturbations to be much faster than the sound crossing time of the shock thickness, so that the shell reacts quasi-statically to the perturbation.

The equations of hydrodynamics, namely the continuity equation 3.4 and the Euler equation 3.10 have already been introduced in section 3.1. For convenience, though, instead of the density ρ , the velocities u_x , u_y and u_z and the pressure P , in this analysis here the variables used are the surface density σ , the radial shock velocity V_r and the tangential shock velocity \mathbf{V}_T :

$$\sigma = \frac{1}{R_s^2} \int_{R_i}^{R_s} \rho r^2 dr \quad (3.24)$$

$$V_r = \frac{1}{\sigma R_s^2} \int_{R_i}^{R_s} \rho r^2 u_r dr \quad (3.25)$$

$$\mathbf{V}_T = \frac{1}{\sigma R_s^2} \int_{R_i}^{R_s} \rho r^2 \mathbf{u}_t dr \quad (3.26)$$

In the absence of perturbations \mathbf{V}_T vanishes.

The shock boundary conditions are:

$$[\rho \mathbf{u}] = 0 \quad (3.27)$$

$$[P + \rho u^2] = 0 \quad (3.28)$$

$$\left[\mathbf{u} \left(\frac{1}{2} \rho u^2 + \frac{\gamma}{\gamma - 1} P \right) + \mathbf{F} \right] = 0 \quad (3.29)$$

The detailed derivation of the thin-shell instability, as well as the contents of Section 3.2.1, can be found in Vishniac (1983).

where \mathbf{u} is now the fluid velocity relative to the shock, \mathbf{F} is the radiative energy flux and the square brackets denote differences across the shock. For an adiabatic shock $\mathbf{F} = 0$.

Following the definitions of the new variables, 3.24-3.26, that is, integrating the equations of hydrodynamics 3.4 and 3.10 across the shock and applying the shock jump conditions 3.27-3.29 as boundary conditions, the evolution equations for σ , V_r and \mathbf{V}_t are obtained:

$$\frac{\partial \sigma}{\partial t} = -2 \frac{V_s}{R_s} \sigma + \rho_E V_s - \sigma (\nabla_{\mathbf{T}} \cdot \mathbf{V}_{\mathbf{T}}) \quad (3.30)$$

$$\frac{\partial V_r}{\partial t} = -\frac{1}{\sigma} (\rho_E V_s V_r - P_i) \quad (3.31)$$

$$\frac{\partial \mathbf{V}_{\mathbf{T}}}{\partial t} = -\frac{\rho_E \mathbf{V}_s}{\sigma} \mathbf{V}_{\mathbf{T}} - \frac{V_s}{\mathbf{R}_s} \mathbf{V}_{\mathbf{T}} + \frac{\mathbf{V}_s}{\sigma} \mathbf{u}_{\mathbf{T}}(\mathbf{R}_s) \rho_E - \int_{R_i}^{R_s} \frac{(c_s^2 r^2 \nabla_{\mathbf{T}} \rho) dr}{\sigma R_s^2} \quad (3.32)$$

where $\nabla_{\mathbf{T}}$ stands for tangential derivatives, $\mathbf{u}_{\mathbf{T}}(\mathbf{R}_s)$ is the tangential velocity of the fluid at the shock surface, as imposed by the boundary conditions, and V_s is the velocity of the shock surface. In the derivation of equation 3.30 one assumes there is no matter flux through the inner boundary, that is, all the matter swept up by the shock as it propagates stays on its surface.

The first term of equation 3.30 just states the obvious fact that, if the mass in the shell remains the same, the surface density of the shell decreases as its radius increases. The second term is the increase in surface density caused by material the shock accretes as it propagates in the surrounding medium. The last term describes the mass transfer on the shell due to bulk tangential motions.

Equation 3.31 describes the change of the radial velocity of the shell as a result of the pressure difference at its outer surface, namely the ram pressure of the surrounding medium $\rho_E V_s V_r$ and at its inner surface, namely the thermal pressure P_i provided by the hot gas driving the shock.

In deriving equation 3.32 and, in fact, for the rest of Vishniac's analysis of this instability, the assumption is made that the shock velocity is equal to the radial velocity: $V_s = V_r$, meaning that the motion of the shock is dominated by its radial expansion and not by tangential motions within it. This stems from the quasi-static assumption 3.23 and simple dimensional arguments.

Equation 3.32 is of particular interest for the study of this instability. The first term on the right-hand side is similar to the second term of equation 3.30, expressing the decrease in tangential motions by the accretion of material from the surrounding medium. The second term just states the decrease in the tangential velocity as the radius of the shock increases. The third term tells us that the accreted material can only be accelerated in the direction of the shock front motion. Using the shock jump conditions, at the same time replacing the pressure at the outer boundary of the shock with the ram pressure, the last term can be rewritten and equation 3.32 reads:

$$\frac{\partial \mathbf{V}_{\mathbf{T}}}{\partial t} = -\frac{\rho_E \mathbf{V}_s}{\sigma} \mathbf{V}_{\mathbf{T}} - \frac{V_s}{\mathbf{R}_s} \mathbf{V}_{\mathbf{T}} - \frac{c_s}{\sigma} \nabla_T \sigma - \frac{P_i}{\sigma} \nabla_T R_s \quad (3.33)$$

where essentially the last two terms of equation 3.32 have been replaced by a term expressing the effects of gradients in the surface density and a term due to changes in the inner surface of the shock. It might seem surprising then, that this term contains R_s instead of R_i . The detailed derivation omitted here, this is justified by the fact that irregularities that come from

variations in the shell thickness are of higher order than irregularities coming from the bulk motion of the shock.

It can be additionally shown that, if the inner thermal pressure balances the outer ram pressure almost exactly, the term with $\nabla\sigma$ in equation 3.33 can be omitted. Now we have two terms, one due to mass accretion and one due to the curvature of the shell, plus one term (the last one), which accelerates material into lagging regions of the shell.

The appearance of this term in the equations is what causes the instability, in an analysis that we will not include in this thesis. Figure 3.1, however, illustrates how an instability might occur due to the presence of this term. The pressures acting on the two surfaces of the shell are of different nature. The inner surface is supported by the isotropic thermal pressure, but the outer surface of the shock is supported by ram pressure, which always acts on a direction normal to the surface. This means that, if there is a ripple on the surface of the shell, the thermal pressure will push material sideways on the ripples. The ram pressure cannot balance this motion, since it has no component in that direction. The result will be, to first order, a tangential force on the shock surface, which will depend on the angle of obliqueness and on the internal pressure.

The derivation of the perturbation equations from this point is straightforward. Here we will just mention that, for example, for an isothermal shock and for a perturbation expressed in the form of spherical harmonics, the shell will be unstable and fragment on scales $6.4 < l < 3M^2$, where l the azimuthal mode of the perturbation and M the Mach number of the shock expansion velocity relative to the internal sound speed of the shock. The smallest wavelengths are defined by the "thin-shell" assumption and the largest wavelengths, comparable to the shock radius, are stabilized by the bulk motion of the shock. Additional effects that can stabilize or destabilize the shock are magnetic fields and the consideration of the thickness of the shock. The growth rate of the unstable modes is roughly $c_s k (k\Delta)^{1/2}$ where c_s the sound speed, k the wavenumber along the shock, and Δ the amplitude of the initial perturbation.

We should also note that, although the analysis quoted here is for the linear regime, the effects we are interested in when we study this problem numerically are related to the non-linear growth of this instability, when the perturbations affect the expansion of the shock and the quasi-static approximation is no longer valid. That is why in this text we quote this type of instability as the "Non-linear Thin Shell instability". However, the above analysis is useful because it shows us why there is an instability in the first place and what its first-order effects are, which offers useful insight in the problem of shell fragmentation. This instability will be discussed further in the text, since it is very relevant to our results.

3.2.2 The Kelvin-Helmholtz Instability

In Section 3.2.1 it was shown that when a spherical shock expands in a uniform medium, ripples on its surface can cause tangential motions of the material in lagging regions. This type of shear motion can give rise to another well-studied dynamical instability, called the Kelvin-Helmholtz instability.

The Kelvin-Helmholtz instability occurs when a stratified, heterogeneous fluid with the different layers in relative motion is perturbed. Its morphological signature are characteristic eddies, like the ones shown in Figure 3.2. In this Section we are going to present results relevant to the case of an inviscid fluid, ignoring for sake of brevity the (stabilizing) effects of

A rigorous derivation of the KH instability (Section 3.2.2) can be found in Chandrasekhar (1961).

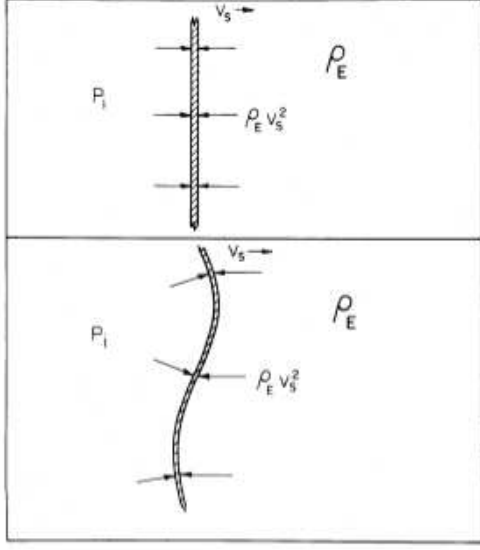


Figure 3.1: Illustration of the thin shell instability, from Vishniac (1983) (Figure 1 of that paper). The different nature of the thermal and the ram pressure cause ripples on the surface of the shock to grow by tangential motions of the material towards lagging regions.

surface tension and magnetic fields.

Using Cartesian coordinates, let the equilibrium configuration be that of a stratified fluid with density $\rho_0(z)$ a function of height z , and a streaming velocity along the x -direction, $u_{x0}(z)$ also a function of z . Then the hydrodynamic variables can be expressed as:

$$\begin{aligned}
 \rho &= \rho_0(z) + \delta\rho \\
 p &= \delta p \\
 u_x &= u_{x0}(z) + \delta u_x \\
 u_y &= \delta u_y \\
 u_z &= \delta u_z
 \end{aligned} \tag{3.34}$$

Inserting the expressions 3.35 for the variables in the equation of continuity 3.4 and the Euler equation 3.10 and neglecting second order terms yields:

$$\rho_0 \frac{\partial \delta u_x}{\partial t} + \rho_0 u_{x0} \frac{\partial \delta u_x}{\partial x} + \rho_0 \delta u_z \frac{d u_{x0}}{d z} = - \frac{\partial \delta p}{\partial x} \tag{3.35}$$

$$\rho_0 \frac{\partial \delta u_y}{\partial t} + \rho_0 u_{x0} \frac{\partial \delta u_y}{\partial x} = - \frac{\partial \delta p}{\partial y} \tag{3.36}$$

$$\rho_0 \frac{\partial \delta u_z}{\partial t} + \rho_0 u_{x0} \frac{\partial \delta u_z}{\partial x} = - \frac{\partial \delta p}{\partial z} - g \delta \rho \tag{3.37}$$

$$\frac{\partial \delta \rho}{\partial t} + u_{x0} \frac{\partial \delta \rho}{\partial x} = - \delta u_z \frac{d \rho}{d z} \tag{3.38}$$

$$\frac{\partial \delta u_x}{\partial x} + \frac{\partial \delta u_y}{\partial y} + \frac{\partial \delta u_z}{\partial z} = 0 \tag{3.39}$$

where a term due to a gravitational acceleration $\mathbf{g} = g\hat{z}$ has been included in equation 3.37 and equation 3.39 expresses the incompressibility of the perturbation.

Looking for perturbations of the form:

$$\exp [i (k_x x + k_y y + \omega t)] \tag{3.40}$$

equations 3.35-3.39 become:

$$i\rho_0(\omega + k_x u_{x0})\delta u_x + \rho_0 \frac{du_{x0}}{dz}\delta u_z = -ik_x \delta p \quad (3.41)$$

$$i\rho_0(\omega + k_x u_{x0})\delta u_y = -ik_y \delta p \quad (3.42)$$

$$i\rho_0(\omega + k_x u_{x0})\delta u_z = -\frac{d\delta p}{dz} - g\delta\rho \quad (3.43)$$

$$i(k_x \delta u_x + k_y \delta u_y) = \frac{d\delta u_z}{dz} \quad (3.44)$$

Now by multiplying equation 3.41 by $-ik_x$ and equation 3.42 by $-ik_y$ and add the resulting equations, replacing at the same time $k^2 = k_x^2 + k_y^2$ and making use of equation 3.44, one obtains:

$$i\rho_0(\omega + k_x u_{x0})\frac{d\delta u_z}{dz} + i\rho_0 k_x \frac{du_{x0}}{dz}\delta u_z = k^2 \delta p \quad (3.45)$$

and from equations 3.43 and 3.44:

$$i\rho_0(\omega + k_x u_{x0})\delta u_z = -\frac{d\delta p}{dz} - ig\frac{d\rho}{dz} \quad (3.46)$$

By eliminating δp from equations 3.45 and 3.46 the following equation is obtained:

$$\frac{d}{dz} \left[\rho_0(\omega + k_x u_{x0})\frac{d\delta u_z}{dz} - \rho_0 k_x \frac{du_{x0}}{dz}\delta u_z \right] - k^2 \rho_0(\omega + k_x u_{x0})\delta u_z = gk^2 \frac{d\rho_0}{dz} \frac{\delta u_z}{\omega + k_x u_{x0}} \quad (3.47)$$

The condition for instability is derived by applying appropriate boundary conditions and considering the specific form of the equilibrium configuration, functions $\rho_0(z)$ and $u_{x0}(z)$.

The simplest assumption we can make for the equilibrium flow is that of essentially two fluids, one of density ρ_1 and velocity u_{x1} and one of density ρ_2 and velocity u_{x2} , superimposed on each other at $z=0$. (A similar configuration is shown in Figure 3.2).

The boundary conditions at $z=-d$ and $z=d$ (for a system of total size $2d$ along the z direction) are just that the vertical components of the fluid velocities vanish on those surfaces. Additionally, we should ask that the components of the fluid velocities normal to their contact surface vanish. In other words, the assumption here is that the two fluids do not mix. Omitting the intervening algebra, we directly present the condition for instability (modes growing exponentially in time), in the absence of surface tension:

$$k > \frac{g(\alpha_1 - \alpha_2)}{\alpha_1 \alpha_2 (u_{x1} - u_{x2})^2} \quad (3.48)$$

where $\alpha_1 = \rho_1/(\rho_1 + \rho_2)$ and $\alpha_2 = \rho_2/(\rho_1 + \rho_2)$. Interestingly, relation 3.48 states that, if one ignores gravity, all wavenumbers are unstable to the Kelvin-Helmholtz instability. The growth rate of the instability, for a step function in the velocity, is $k\Delta v$, where k the unstable wavenumber and Δv is the velocity difference between the two layers.

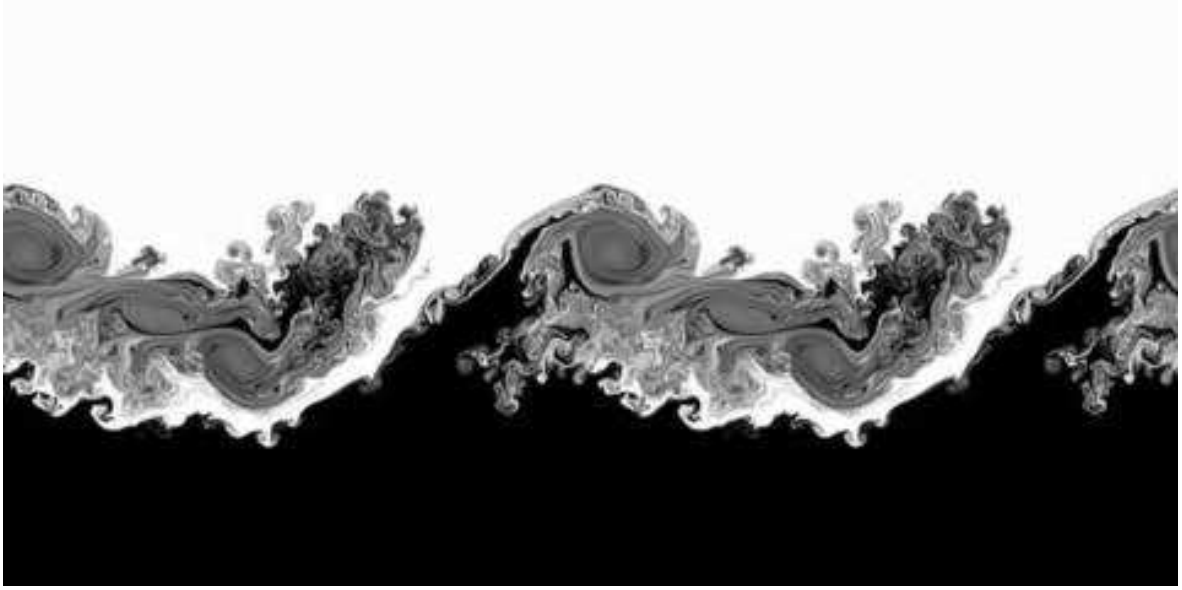


Figure 3.2: Simulated KH instability. A perturbation on the contact layer between two fluids of different density, shown here in black and white color, moving along the horizontal direction relative to each other, grows to give characteristic eddies like the ones shown in this figure. This configuration is already in the nonlinear regime of the instability growth. (Image from wikimedia.org)

3.2.3 The Thermal Instability

The Thermal Instability has already been presented in Section 2.6.1 in a qualitative way. Figure 2.6 provides a schematic illustration of how this instability works. Here we will give some dimensional arguments of when the instability takes place and what its overall behavior is.

Let

$$L(\rho, T) = 0 \quad (3.49)$$

define the heating-cooling equilibrium curve of the gas, where $L(\rho, T)$ represents the energy gains minus the energy losses of the gas per unit mass per unit time.

A perturbation of density and temperature is introduced, such that some thermodynamic quantity A , the pressure for example, remains constant. Then the entropy of the gas will change by an amount δS and the heating-cooling function L will change by an amount δL :

$$\delta L dt = -Td(\delta S) \quad (3.50)$$

where changes are to be calculated with A constant. Then the criterion for instability is

$$\left(\frac{\partial L}{\partial S} \right)_A > 0 \quad (3.51)$$

in other words, there is an instability if the gain-loss function L is a monotonous function of the entropy, so that changes in the entropy due to perturbations always cause a response of the same sign from the heating-cooling function and the perturbation can grow. Assuming

The contents of Section 3.2.3, as well as a full derivation of the TI can be found in Field (1965).

an ideal gas, for an isochoric perturbation $T dS = C_V dT$ and for an isobaric perturbation $T dS = C_P dT$. Then one obtains two criteria for the instability, an isochoric and an isobaric one:

$$\left(\frac{\partial L}{\partial S}\right)_\rho < 0, \text{ (isochoric)} \quad (3.52)$$

$$\left(\frac{\partial L}{\partial S}\right)_P = \left(\frac{\partial L}{\partial T}\right)_\rho - \frac{\rho_0}{T_0} \left(\frac{\partial L}{\partial \rho}\right)_T < 0, \text{ (isobaric)} \quad (3.53)$$

Criterion 3.52 is in principle incompatible with the force equation, because isochoric temperature variations will cause changes in the density, which then cannot be assumed constant. Condensations can be shown to be dominated by the isobaric condensation, which is compatible with the force equation. This can also be derived by a more detailed treatment of the instability.

Burkert & Lin (2000) showed that the growth rate of the thermal instability does not depend on the size of the perturbation (ie the wavenumber), but is rather determined by the local cooling time. In particular, the growth of a perturbation is decided by the transition from isobaric to isochoric cooling. This implicitly means that the smallest perturbations will grow first. The smallest unstable scale, according to their analysis, is decided by thermal conduction. In the discussion of our results we will comment more on the role of thermal conduction and its meaning with respect to our findings.

3.3 The instabilities combined

In the context of shell fragmentation it is very useful to study the effects of all the aforementioned instabilities simultaneously, since each of them will contribute to the dynamics of the formed phases, if any. We naturally expect, however, that each instability will be dominant in different regimes, according to the size of the shock and the general properties of the gas.

Heitsch et al. (2008a) explored precisely this subject, separating the phase space of the gas into different regimes. Figure 3.3 from their paper illustrates the result:

To visualize this result, in Figure 3.4 we plot contours of the gas temperature for an idealized setup, designed to study the fragmentation of a shock due to these three instabilities. In this setup, a very thin slab between two infinite, high-Mach flows is perturbed. This is expected to trigger the NTSI and in turn, the TI and the KHI. The Figure shows the results of two-dimensional hydrodynamical simulations of this setup after the instabilities have had significant time to develop. Shown on the left is the result of a Mach 1 flow and on the right the result of a Mach 3 flow. In accordance with previous findings, we see that different flow Mach numbers lead to slightly different results: Although both shocks are fragmenting, the one on the left shows more clumpy structure, signature of the TI, while the shock on the right is more violently disturbed by the NTSI, as indicated by the large finger-like structures growing perpendicularly to the slab.

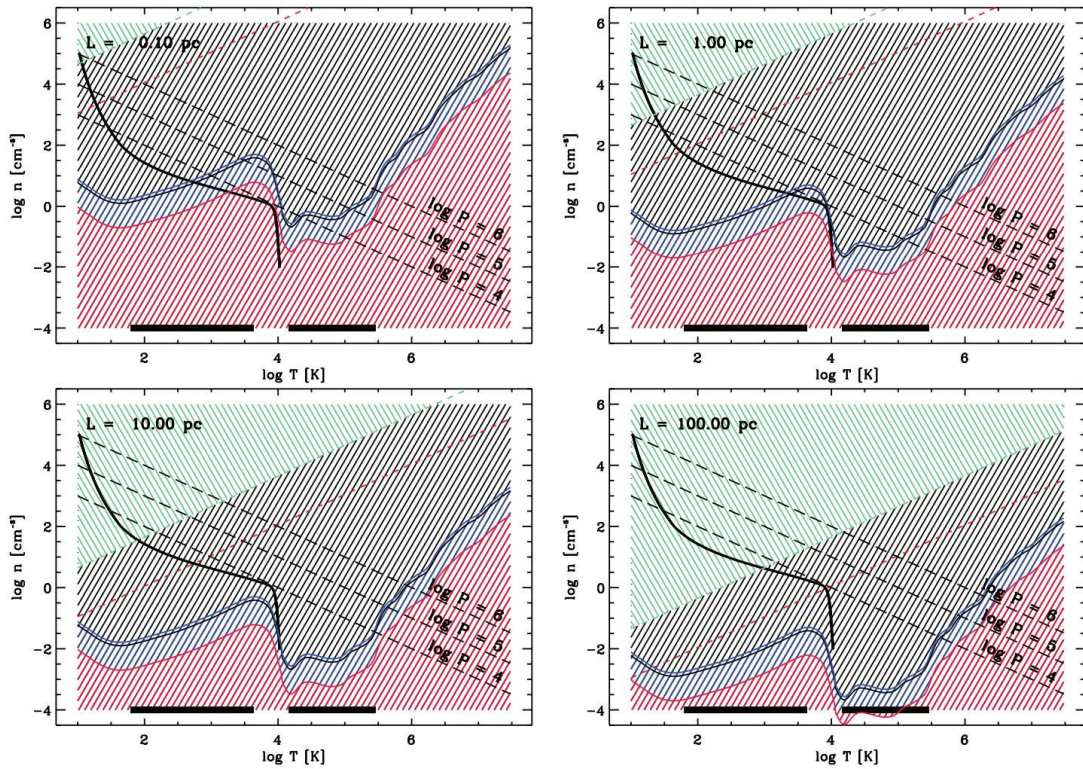


Figure 3.3: Instability regimes in density and temperature space. The solid black line shows the cooling-heating equilibrium curve. Cooling instability causes fragmentation in the regions with positive slope and gravity is important in the regions with negative slope. Red hatching shows where dynamics (KHI, NTSI) dominates over cooling and blue hatching shows where the TI dominates dynamics. (Figure and caption from Heitsch et al. (2008a))

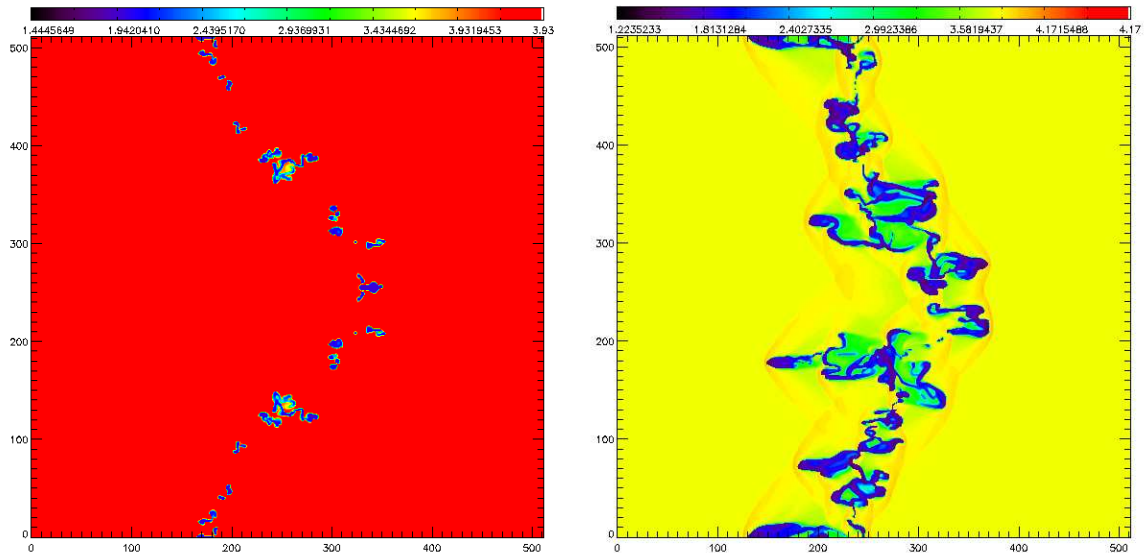


Figure 3.4: Simulations of a perturbed slab, bounded on each side by an infinite flow. On the left, a Mach 1 flow. On the right, a Mach 3 flow. The colors indicate different contour levels of the logarithm of temperature. The physical scale is of 44 pc at each direction.

3.4 Some comments on turbulence

Considering now a non-ideal fluid, that is, a fluid the kinematic viscosity of which is not negligible, and also assuming incompressibility of the fluid flow, the equations of hydrodynamics 3.4 and 3.10 become:

$$\nabla \cdot \mathbf{u} = 0 \quad (3.54)$$

$$\frac{\partial \mathbf{u}}{\partial t} + \mathbf{u} \cdot \nabla \mathbf{u} = -\nabla p + \nu \nabla^2 \mathbf{u} \quad (3.55)$$

where ν is the kinematic viscosity of the fluid. Equations 3.54 and 3.55 are usually referred to as the Navier-Stokes equations.

In principle, the Navier-Stokes equations, supplemented with appropriate boundary and initial conditions, include all the information we need in order to predict the behavior of a fluid flow. However, even from everyday life, we are aware of flows which behave in a highly unpredictable manner, such as the smoke of a cigarette as it rises in the air, or the flow of water behind a boat. These are examples of flows where the pattern changes rapidly, showing a dynamical, almost chaotic behavior. These kind of flows are called turbulent flows.

The study of turbulence has puzzled theoretical and experimental physicists for centuries, for the obvious reason that, in most cases, there appears to be no way to predict the flow patterns seen in experiments directly from the Navier-Stokes equations, even when we know the boundary and initial conditions with high accuracy. Fortunately, however, it is possible to formulate hypotheses based on the experimental data and then, from equations 3.54 and 3.55 derive laws that can help predict properties of the flows.

One very important parameter in the study of turbulent fluid flows is the Reynolds number. It is defined as

$$R = \frac{L V}{\nu} \quad (3.56)$$

where L and V are a characteristic length and a characteristic velocity of the system under study, respectively. It can be shown that the Reynolds number is in fact the only control parameter for a self-similar, incompressible flow, that is, a flow with defined geometrical shape. A well-known example of such a flow, the flow behind a solid circular cylinder, has been studied extensively both in experiments and in simulations. Such studies show that the transition from a laminar (ordered) flow to a turbulent flow is only controlled by the Reynolds number. As the Reynolds number increases, the flow gradually loses its symmetries, until it eventually becomes turbulent.

For high Reynolds numbers, when the fluid is well into the turbulent regime (a state usually referred to as "fully developed turbulence") there are two well-established experimental laws: The two-thirds law and the law of finite energy dissipation.

The two-thirds law states that, in a turbulent flow of very high Reynolds number, the mean square velocity increment, $\langle (\delta u(l))^2 \rangle$ between two points, separated by a distance l , behaves as the two-thirds power of the distance:

$$\langle (\delta u(l))^2 \rangle \propto l^{2/3} \quad (3.57)$$

The contents of Section 3.4 can be found in Frisch (1996). The phrasing of the experimental laws and theoretical hypotheses has been quoted almost word for word from that text for exactness.

The law of finite energy dissipation says that, if in an experiment on turbulence all the control parameters are kept the same and only the viscosity is varied, brought to the lowest value possible, then the energy dissipation per unit mass of the fluid, dE/dt , behaves in a way consistent with a finite positive limit ϵ .

These two experimental laws have been included in the form of three hypotheses, in order to derive the famous Kolmogorov (1941) theory for turbulence. This theory, in accordance to what we explained above, can only predict some statistical aspects of the flow, under certain conditions. It is, however, the closest we have to a theoretical description of turbulence.

The first hypothesis is formed to reconcile the apparent inconsistency of the mechanisms that generate turbulence with the flow symmetries. The scale-invariance typically observed in turbulent flows must also be reconciled with potential boundary effects. Then the hypothesis is made that, in the limit of infinite Reynolds number, all the possible symmetries of the Navier-Stokes equations, usually broken by the mechanisms producing the turbulent flow, are restored in a statistical sense, at scales small compared to the integral scale and away from the boundaries.

The term "integral scale" above defines the length scale on which the turbulence driving mechanism operates. This, in the case of the flow past a cylinder, for example, would be the diameter of the cylinder. According to the first hypothesis then, the scales for which the Kolmogorov theory is valid are always smaller than the integral scale, so that we do not have to worry about effects due to the distance from the turbulence driver or boundary effects of the fluid.

The second hypothesis is necessary in order to explicitly express the scale invariance of turbulence. Since in principle there are infinite possibilities for the scaling exponent of the flow, giving rise to infinite similarity groups. Under the same assumptions as the first hypothesis, the turbulent flow is self-similar, in other words it possesses a single scaling exponent $h \in \mathbb{R}$ such that

$$\delta \mathbf{u}(\mathbf{r}, \lambda \mathbf{l}) = \lambda^h \delta \mathbf{u}(\mathbf{r}, \mathbf{l})$$

The third and final hypothesis that goes into the Kolmogorov (1941) theory is that, under the same assumptions as in the first hypothesis, the turbulent flow has a finite, non-vanishing mean rate of energy dissipation, ϵ per unit mass.

Using these hypotheses, Kolmogorov derived the first and only exact result obtained so far to describe a turbulent flow, his famous "four-fifths law". Defining the longitudinal structure function of order p as

$$S_p(l) \equiv \langle (\delta u_{\parallel(l)})^p \rangle \quad (3.58)$$

we can now express this law: In the limit of infinite Reynolds number, the third-order longitudinal structure function of homogeneous isotropic turbulence, evaluated for length intervals l small compared to the integral scale, is given in terms of the mean energy dissipation per unit mass, ϵ (assumed to be finite and non-vanishing) by

$$\langle (\delta u_{\parallel}(\mathbf{r}, \mathbf{l})^3) \rangle = -\frac{4}{5} \epsilon l \quad (3.59)$$

Equation 3.59 is not only an exact, non-trivial result of the Navier-Stokes equations, but it can also be shown to stand, to an order of magnitude approximation, also for compressible flows.

Using the self-similarity hypothesis and dimensional arguments, it can be shown that Kolmogorov's four-fifths law implies a power-law energy power spectrum in Fourier space:

$$E(k) \sim \epsilon^{2/3} k^{-5/3} \quad (3.60)$$

Relation 3.60 is an important scaling law for turbulence and we will be using it in our simulations.

Another interesting result of dimensional analysis relates to the numerical resolution necessary for modelling a turbulent flow. Using the velocity u_0 and the length l_0 at the integral scale, the expression with dimensions of energy dissipation of unit mass is $\epsilon = u_0^3/l_0$. The dissipation scale of turbulence, expected to happen at the viscous scale from molecular interactions, is $\eta = \left(\frac{\nu^3}{\epsilon}\right)^{1/4}$. Then the ratio of the integral scale to the dissipation scale will be

$$\frac{l_0}{\eta} \sim \left(\frac{\nu^3}{l_0 u_0^3}\right)^{-1/4} = R^{3/4},$$

a function of the Reynolds number. This means that, for example, in order to simulate a flow of Reynolds number, say, 10000, we need at least 1000 grid cells per integral scale.

Previous Work

4.1 Molecular Cloud Formation

In the previous Chapters we introduced some general features of the ISM as they are known from observations, as well as the basic theoretical background necessary to understand the gas physics relevant to the dynamics of the ISM. Here we give the motivation for the work in this thesis, which focuses on the formation mechanisms of the CNM and potentially molecular clouds as well.

Due to its very high density, molecular gas amounts to only a small fraction of the volume of the Galactic interstellar medium, but it dominates interstellar mass (Ferrière, 2001). More specifically, only 1-2% of the gas volume in the Galactic disk is in the molecular phase, but it makes up about 50% of the total gaseous mass.

In Chapter 2 we mentioned that this phase of the interstellar medium exists in galaxies in highly irregular clouds, with very clumpy, almost fractal structure. The large-scale morphology of these clouds is very filamentary, according to observations in different wavelengths (Schneider & Elmegreen, 1979; Lada et al., 1999; Hartmann, 2002; Lada et al., 2007; Molinari et al., 2010), mainly capturing CO transitions and dust absorption or emission and thus probing slightly different gas temperatures and densities. The internal density distribution of molecular clouds is extremely hierarchical, with large, diffuse structures hosting dense cores. Molecular clouds, as well as the dense cores in their interior, show a mass distribution that can be very well described by a power-law. For the masses of molecular clouds in our Galaxy the power-law index is about -1.7 (ie Parmentier (2011)), while for the prestellar core mass function the slope is shallower, of about -1.3 (ie Alves et al. (2007)). This behavior indicates a very dynamical nature of the interstellar molecular gas. Explaining these morphological features is the main driver of this work.

Nevertheless, maybe the most important fact about molecular clouds is that they are the sites of all observed star formation. In fact, there is a very well-known correlation of the column density of molecular gas with the star formation rate of a galaxy at large scales

This chapter is largely an adaptation of the introduction section of Ntormousi et al. (2011).

(Wong & Blitz, 2002; Kennicutt et al., 2007). Evidently, they must become gravitationally unstable at some stage of their evolution. On the other hand, a typical molecular cloud mass is about $10^{4-5} M_{\odot}$, with a typical temperature of 50 Kelvin, which makes its collapse time under its own gravitation very short. Any model aiming at explaining star formation should then account for the fact that, not only will such a cloud give several stars of typical masses around $1 M_{\odot}$, instead of a single, $10^{4-5} M_{\odot}$ object, but it will form them at a gas-to-stars conversion efficiency of only a few percent (Zuckerman & Evans, 1974).

There are many ideas as to why this should be so. One possible solution is that these clouds be sustained by strong internal motions, which can provide a support against gravitational collapse in the form of an additional internal pressure. Luckily, this view is also supported by the large non-thermal line widths typically observed in molecular clouds, which do indicate internal supersonic turbulence (Falgarone & Phillips, 1990; Williams et al., 2000). Turbulence is also an elegant mechanism to fragment the cloud in smaller clumps, which can decouple from the rest of the cloud and become gravitationally unstable to give lower mass objects (Larson, 1981; Padoan, 1995; Klessen, 2001).

The interpretation of the aforementioned properties of molecular clouds in combination is a very challenging task, but it can be somehow alleviated by seeking a common characteristic to them, one they could inherit from the cloud formation process. If we identify this common quality as non-linearity, then a natural formation mechanism for molecular clouds is a combination of fluid instabilities (Burkert, 2006).

One general example of an environment that would seed a non-linear fluid evolution, and at the same time could assemble the large amounts of gas necessary for the formation of molecular clouds are large-scale converging atomic flows, an idea proposed by Ballesteros-Paredes et al. (1999) and Hartmann et al. (2001) to explain the fact that stellar populations in local star-forming clouds have age spreads that are significantly smaller than the lateral crossing time of the cloud. Such flows could in principle be anything from expanding shells (Elmegreen & Lada, 1977a; McCray & Kafatos, 1987a), to colliding shells (Nigra et al., 2008), or flows generated by large-scale gravitational instabilities (Yang et al., 2007; Kim & Ostriker, 2002, 2006).

Pringle et al. (2001) proposed an alternative mechanism for molecular cloud formation by agglomeration of gas which is already molecular. Although the formation of large clouds from smaller, already molecular clumps is a possible scenario (Dobbs et al., 2011), there is still no observational evidence for the existence of a large molecular gas reservoir in the ISM outside giant molecular clouds.

Heitsch et al. (2006, 2008a) studied the formation of cold and dense clumps between two infinite flows which collide on a perturbed interface. Their study showed that cold structure can arise even from initially uniform flows if the conditions favor certain fluid instabilities, such as the Non-linear Thin shell instability (NTSI, Vishniac (1994)), the Thermal Instability (Field, 1965) and the Kelvin-Helmholtz instability. We will discuss each of them in detail in the following chapter.

Vázquez-Semadeni et al. (2006, 2007) used colliding cylindrical flows of tens of parsecs length, adding random velocity perturbations to the average flow velocity. This allowed them to study star formation efficiencies and the fates of individual clouds.

These numerical experiments have investigated the mechanisms which lead to the condensation and cooling of atomic to molecular gas and which cause the complex structure of the resulting clouds, independent of the specific mechanism driving the flows. In a further improvement of these models, in this work we study the possibility for cold structure formation from colliding flows of limited thickness. Specifically, we model the expansion and collision of

thin shells, created by wind- and supernova-blown superbubbles numerically and study the formed structures.

4.2 Shell fragmentation and collapse

Stellar feedback is a very powerful source of thermal and turbulent energy in the Interstellar Medium (ISM). Young massive stars, namely stars of O and B spectral types, produce ionizing photons, expel large amounts of mass in winds and end their lives in supernova explosions, all processes which shape the matter around them in shells and cavities. Young OB associations, as groups of between 10 and 100 such stars are commonly called, will create giant shell-like shocks in their surrounding space from the combined effect of their member stars. Such shells have been repeatedly observed in our Galaxy in various wavelengths (Heiles, 1979, 1984; Ehlerová & Palouš, 2005; Churchwell et al., 2006).

These shells are potentially unstable to non-radial perturbations as they expand, as shown by various analytic studies of thin, shock-bounded or pressure-bounded slabs (Vishniac, 1994; Vishniac & Ryu, 1989). Vishniac's analytical work on shell fragmentation has been briefly presented in section 3.2.1. On the other hand, perturbations on large, self-gravitating shells are able to grow to the point where they can collapse to form stars (Elmegreen, 1994; Whitworth et al., 1994), a scenario usually referred to as the "collect-and-collapse" model. This process has been proposed as a trigger of star formation in many environments (Elmegreen & Lada, 1977b; McCray & Kafatos, 1987b).

An extensive numerical study of the instability of expanding shells, taking into account nonlinear effects and the different parameters entering the shell expansion was presented in a series of papers by Dale et al. (2009), Wunsch et al. (2010) and Dale et al. (2011). The focus of that work being only the gravitational instability of the shells, it is interesting to carry out an analysis of shell fragmentation due other instabilities, such as the Non-linear Thin Shell Instability (Vishniac, 1983) for comparison. This is one of the numerical experiments contained in this thesis.

Giant shells are expected to collide with each other as neighboring stellar associations evolve (de Avillez & Breitschwerdt, 2004; Nigra et al., 2008), but whether or not these collisions happen before or after the shell has had time to fragment and gravitationally collapse is not clear. If the shells were to collide before star formation had occurred on their surface, the collision could trigger a phase change from the atomic gas gathered by the shocks to molecular gas, thus forming molecular clouds by the mechanism described briefly in the previous Section. The detailed processes which lead to this phase transition will become clearer in the following Chapter.

Numerical Method

5.1 Solving the equations of hydrodynamics on a grid

In order to solve the equations of hydrodynamics numerically, they need to be discretized in space and in time. There are various approaches to this problem, depending on the choice of the form of the equations and on the details of the numerical integration scheme. Here we will briefly discuss the Eulerian class of methods because it contains the algorithm we have used in our work. Eulerian methods discretize space on a mesh, usually Cartesian, and follow the evolution of fluid variables on the fixed locations of the grid points.

In principle, this class of methods first calculates the spatial derivatives that appear in the equations of hydrodynamics, treating them at the right-hand side of the equations, and then advances these quantities in time by a discrete step dt , treating the temporal derivatives as the left-hand side of the equations.

It is easy to understand that, when studying the propagation of a fluid on a grid, there is a point in the calculation at which the flux of material across the grid cell surfaces needs to be calculated. This is how the advection terms can be approximated in the grid configuration. The foundation for the class of methods we are going to be discussing here is the so called "Riemann problem".

The Riemann problem is defined for an initial state of the fluid where all the variables are strictly constant for, say, positive x and strictly constant for negative x , but their values change at $x = 0$: $q_i = q_L$ for $x < 0$ and $q_i = q_R$ for $x > 0$, where q_i represent each of the hydrodynamic variables. It is now obvious how this problem relates to solving the equations of hydrodynamics on a grid; at the smallest scales, each grid cell contains a state of the fluid which is constant across its length. The neighboring grid cell will, in principle, contain a different (constant) state of the fluid and the Riemann problem is perfectly defined at their boundary.

In order to solve the Riemann problem for hydrodynamics, one needs to rewrite the

The short introduction to the Riemann problem contained in Section 5.1 is from "Finite Volume Methods for Hyperbolic Problems" by Randall LeVeque.

equations 3.4, 3.10 and 3.21 in a matrix form:

$$\frac{\partial}{\partial t} \begin{pmatrix} \rho \\ u_x \\ e \end{pmatrix} + \begin{pmatrix} u_x & \rho & 0 \\ \frac{1}{\rho} \left(c^2 - \frac{P}{\rho} \Gamma \right) & u_x & \Gamma \\ 0 & \frac{P}{\rho} & u_x \end{pmatrix} \frac{\partial}{\partial x} \begin{pmatrix} \rho \\ u_x \\ e \end{pmatrix} = 0 \quad (5.1)$$

where we have written the equations only for one component of the velocity, u_x , e is the total energy per unit mass of the fluid element, $\Gamma = \rho \left(\frac{\partial}{\partial e} \right)_\rho$ is called the "Grüneisen exponent" and $c^2 = \left(\frac{\partial P}{\partial \rho} \right)_e + \frac{P}{\rho^2} \left(\frac{\partial P}{\partial e} \right)_\rho$ is the sound speed. This form of the equations makes it a lot easier to search for the eigenvectors of the system.

From a calculation we will omit here we get three eigenvectors, each representing a quantity called a "Riemann invariant". A numerical solver will have to calculate these quantities at the cell interfaces. The solution can be pictured as waves propagating in the fluid contained in a grid cell. One class of waves contains the information for the propagation of the fluid itself and two are sound waves, one moving in the positive and one in the negative x-direction. The discrete step for advancing the equations in time will be decided on the condition that these waves not have time to cross the cell length in one timestep.

This is actually the basis for a numerical method called the Godunov method. In this method, a grid is defined by the centers of its cells. If we imagine that the x-direction has been discretized, then the state of the gas q_i^n at time step t_n is known at the locations x_i , the centers of N intervals on the one-dimensional space we are considering. The cell interfaces are then $x_{i+1/2}$, each between x_i and x_{i+1} . The Riemann problem can be solved at each one of these intervals to give the transition of the fluid from one cell to the next. The time step for the numerical code will be chosen such that solutions from neighboring cells not overlap:

$$\Delta t \leq \min(\Delta t_i) \quad (5.2)$$

where

$$\Delta t_i = \frac{x_{i+1/2} - x_{i-1/2}}{\max(\lambda_{i-1/2, k+}) - \min(\lambda_{i+1/2, k-})} \quad (5.3)$$

and $\lambda_{i-1/2, k+}$ denotes the maximum positive eigenvalue of the matrix in equation 5.1 at interface $x_{i-1/2}$ and $\lambda_{i+1/2, k-}$ the most negative eigenvalue at interface $x_{i+1/2}$. This criterion is essentially a mathematical expression for what we described in words above: The timestep should be smaller than the time it takes the fastest waves to cross a cell length, so that the solutions do not overlap.

In Godunov schemes, in short, the solution advanced in time at position x_i from time step t_n to t_{n+1} is given by

$$q_i^{n+1} = q_i^n + \Delta t \frac{F_{i+1/2}^n - F_{i-1/2}^n}{x_{i+1/2} - x_{i-1/2}} \quad (5.4)$$

where $F_{i+1/2}^n$ and $F_{i-1/2}^n$ are the fluxes calculated at the cell interfaces by solving the Riemann problem.

For the numerical simulations in this work we have used the publicly available RAMSES code (Teyssier, 2002), a Eulerian Cartesian code using a Godunov scheme to solve the equations of hydrodynamics. The code has Adaptive Mesh Refinement (AMR) capabilities, of which we have made use in some of the simulations in this thesis and which we will shortly

discuss in the following Section. We will introduce the general features of the code, as presented by its author, as well as adaptations we have made to selected modules to simulate physics specific to our purpose.

5.2 The RAMSES code

The RAMSES code has been designed to treat problems relevant to cosmology, so it contains both an N-body solver, used to calculate the gravitational interaction of collisionless components such as dark matter and stars, and a hydrodynamics solver with AMR capabilities in order to capture the full dynamical range of cosmological systems.

In this work we have not made use of the N-body solver of the code at all, so we will not discuss it further. AMR, on the other hand, can be a very useful tool when studying the physics of the ISM. It is evident from what we have discussed so far that the scales relevant to the study of interstellar gases range from galactic (kpc), to scales where protostellar disks are found (10^{-3} pc). Evidently, the resolution required to capture the evolution of the gas in all of these scales at once is enormous, making such simulations prohibiting.

Fortunately, in a numerical simulation of such a structured system, the resolution does not have to be as high in all regions of the computational domain. For instance, the evolution of the gas within a supernova shell are much more dynamical and structured than inside the hot gas bubble. AMR gives us the possibility to resolve only the regions of interest in our simulations, and to let the code decide which these regions are as the simulation advances. In this way our simulation becomes much more efficient and requires less resources.

In order to achieve AMR, the code is not structured on a basis of single cells, but rather uses "octs", groups of 2^{dim} cells grouped together as the elements of computation, dim denoting the number of dimensions of the simulation. Each oct group belongs to a level of refinement l , which is advanced in time independently.

When certain criteria are fulfilled at refinement level l , say, then an oct is divided into its components and the evolution of the fluid variables is not followed on level $l + 1$. Of course, the actual implementation of this process in the code is more complicated, due to the necessary optimization for parallelization and for higher performance in general.

The criteria for the refinement of the grid can be geometrical, they can be based on the gradients of hydrodynamical quantities, or can relate to the mass contained in an oct. We will discuss this in more detail in Chapter 8.

The equations of hydrodynamics are solved in the code in their conservative form:

$$\frac{\partial \rho}{\partial t} + \nabla \cdot (\rho u) = 0 \quad (5.5)$$

$$\frac{\partial(\rho u)}{\partial t} + \nabla(\rho u \times u) + \nabla P = -\rho \nabla \phi \quad (5.6)$$

$$\frac{\partial(\rho e)}{\partial t} + \nabla \cdot [\rho u(e + p/\rho)] = -\rho u \cdot \nabla \phi \quad (5.7)$$

with the fluid pressure defined as $p = (\gamma - 1)\rho(e - \frac{1}{2}u^2)$, γ is the adiabatic index and ϕ the gravitational potential. Equation 5.7 conserves energy exactly, if we ignore the term due to

Here we limit ourselves to the parts of the code we have used. A detailed description of the code and its full capabilities can be found in Teyssier (2002).

gravity. In Section 5.3 we will discuss additional sources and sinks of energy relevant to our work.

5.3 Sources and sinks of energy

5.3.1 Implementation of a new cooling and heating module

In Chapter 2 we introduced the cooling and heating processes of interstellar gas and we explained that they are of extreme importance for the formation of phases in the ISM. It is therefore essential that we include these processes in our simulations.

The cooling-heating function follows Wolfire et al. (1995) and Dalgarno & McCray (1972) in the low temperature regime ($T < 25000K$) and Sutherland & Dopita (1993) in the high-temperature ($25000K < T < 10^8K$) regime. The cooling and heating rates have been discussed in Section 2.6.2 and are shown in Figure 2.8 as a function of density and temperature.

At each timestep of a refinement level and for each cell, the code calculates the gains and losses of the gas from this tabulated function, according to the state of the gas in the cell. Then it adds or subtracts the appropriate energy from that cell before advancing the solution in time. The timestep has to be adjusted accordingly, so that the cell does not acquire a negative temperature when the cooling rates are very high.

5.3.2 Implementation of a winds

In this work we are studying the impact of hot gas from young massive stars to the surrounding gas and the triggered formation of structured, cold gas.

The implementation of the energy and mass feedback from such stars for RAMSES has been done by Katharina Fierlinger as part of her PhD work, so here it will only be shortly presented. The model for the feedback from massive stars is provided from Voss et al. (2009). The population synthesis model presented therein provides the energy and mass injection from an "average star" of an OB association with time. Such a star represents an entire population according to a stellar Initial Mass Function, in that its feedback includes the contributions from stars of all spectral types.

Figure 5.1 shows the energy and mass injection rate from one such star with time, from the combined effects of stellar winds and supernova explosions.

The domain where feedback is active is defined as a circular region where the cells receive an extra energy and mass at the beginning of their time step. That energy and mass, taken from a tabulated form of the data shown in Figure 5.1 are weighted according to the number of stars the OB association is assumed to contain and to the portion of the cell that is found inside the region. More details on the wind implementation in RAMSES can be found in Fierlinger et al. (2011, in prep.)

5.4 Creating turbulent initial conditions

In order to achieve a turbulent initial condition for the diffuse medium, we set up a turbulent velocity field according to Mac Low et al. (1998), that is, we introduce Gaussian random perturbations in Fourier space, in a range of wave numbers from $k = 1$ to $k = 4$.

The root mean square (rms) Mach number of the turbulent flow is chosen close to unity, so that the turbulent kinetic energy of the gas is equal to its thermal energy. The energy

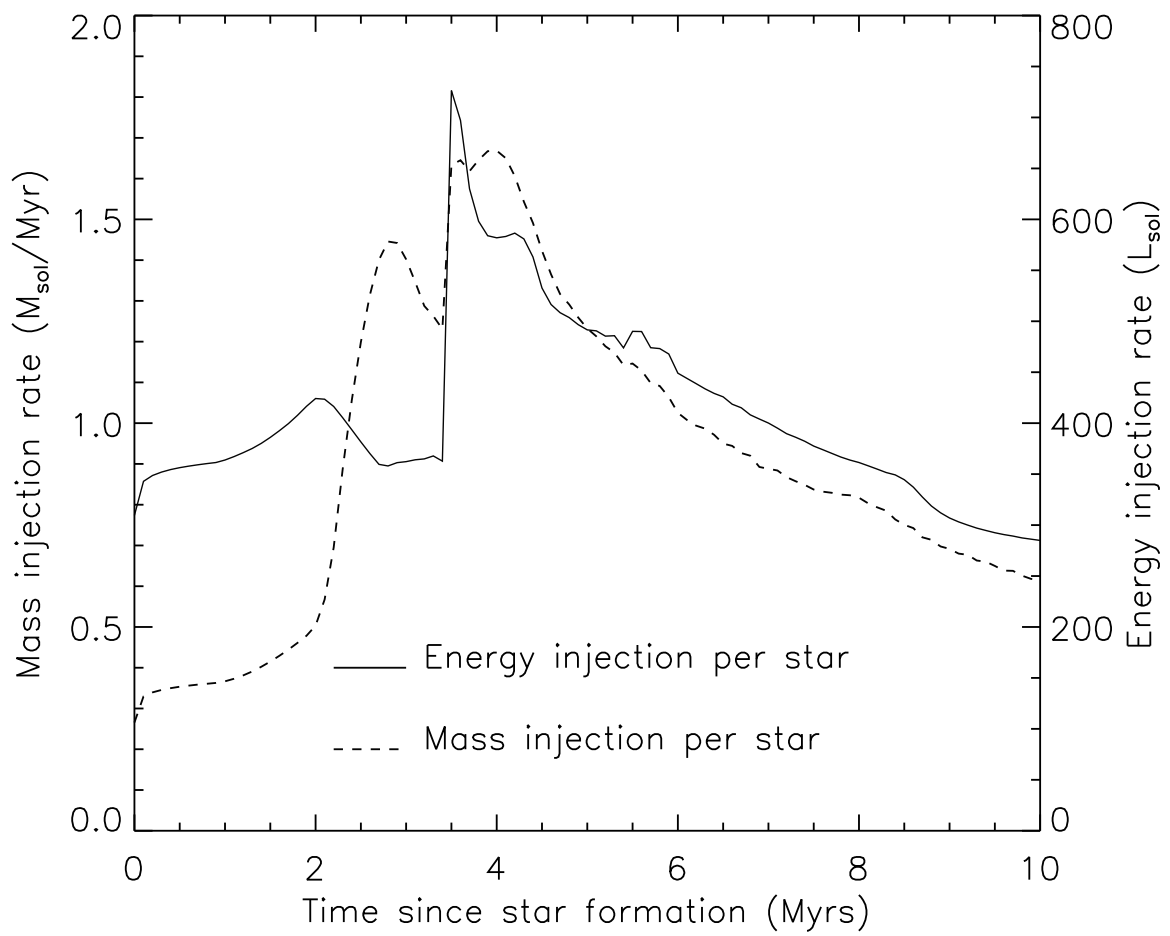


Figure 5.1: Time dependence of the wind properties for an "average star". The solid line shows the energy injection rate in units of solar luminosity and the dashed line shows the mass injection rate in solar masses per Myr. The data are from Voss et al. (2009)

equipartition assumption between thermal and turbulent kinetic energy is consistent with the turbulent velocity dispersions calculated for Galactic HI (Verschuur, 2004; Haud & Kalberla, 2007).

After this initial velocity field is calculated, it is introduced as an initial condition to the code, using a uniform hydrogen density of $n_H = 1/cm^3$ and temperature $T=8000$ K. The evolution of the gas is followed isothermally and with periodic boundary conditions until the density-weighted power spectrum of the turbulent velocity field has a power-law slope close to Kolmogorov (1941) and the density field loses the signature of the initial conditions. During this time the Mach number is kept constant by driving.

The resulting velocity, density and pressure structure is used as an initial condition for the simulations of bubble expansion.

In these calculations the driving of turbulence in the diffuse medium has been neglected, since the turbulence crossing time for our computational domain ($t_{cr} \simeq 86$ Myrs) is much longer than the entire simulation. We can therefore safely assume that there are no significant energy losses due to dissipation on this time scale.

5.5 Simulation setup

We simulate a region of physical size equal to 500^2 pc², with a resolution of 4096 points at each dimension. This yields a spatial resolution of about 0.1 pc. An 8192^2 resolution run has also been performed but, due to its high computational cost, only for limited integrations and for testing some resolution effects. Although a 0.1 pc resolution is not sufficient to resolve the smallest structures in the ISM (see for example, discussion in Hennebelle & Audit (2007a)), many of the clumps which form in these simulations can still be resolved adequately. Structures that fall near our resolution limit are not taken into account in our analysis.

As an initial condition we use either a uniform or a turbulent diffuse medium, of hydrogen density $n_H = 1/cm^3$ and temperature $T=8000$ K. In the case of the turbulent medium these are, of course, average quantities. We assume the background to be an ideal monoatomic gas with a ratio of specific heats γ equal to 5/3 and mean molecular weight $\mu = 1.2m_H$.

The metallicity assumed in the simulations is solar. Our initial condition is chosen to lie on a stable point of the heating-cooling equilibrium curve, so that the thermal instability cannot be triggered unless the medium is externally perturbed. Of course, this is not exactly true everywhere for the turbulent case, but density fluctuations are not large enough to lead to a two-phase medium without triggering from the shocks.

In this diffuse medium we insert time-dependent winds that are meant to mimic the combined effects of winds and supernova explosions in young OB associations. We include two wind regions, placed on the edges of the computational domain and we assume them to form simultaneously. We follow their expansion into the diffuse medium until they collide and a turbulent region arises at their interaction region. Reflecting boundaries are used along the x-direction and outflow boundaries along the y-direction.

These calculations include no external gravity field or self-gravity of the gas.

Time zero for the simulation is when star formation starts in the wind areas. The system is evolved in time until boundary effects become potentially important, which is 7 Myrs for both simulations.

Formation of cold filaments from colliding shells

6.1 Shell collision in a uniform diffuse medium

In order to study the expansion of the superbubbles and the development of fluid instabilities relevant to it, we first simulated the two wind regions in a homogeneous diffuse background medium. Figure 6.1 shows two snapshots of the simulation in logarithm of temperature and logarithm of density.

During the expansion of the superbubbles we observe three effects from three different fluid instabilities. The acceleration of the shock leads to the NTSI, which focuses material on fluctuation peaks. These condensations are unstable to the Thermal Instability, so they condense and cool further. The velocity shear caused by the NTSI at the same time also triggers the Kelvin-Helmholtz instability.

As one can see in Figure 6.1, the NTSI develops faster along the x and y axes, where we observe more pronounced "finger-like" structures, characteristic of this instability. This is clearly a resolution effect. Vishniac & Ryu (1989) showed that for an expanding decelerating shock there is a critical overdensity with respect to the post-shock gas above which the shell is unstable. The authors estimated this critical overdensity to be of the order 25 for a wind-blown shock. Since in our simulations we do not resolve the smallest cooling length adequately, gas cannot be condensed into as small a volume as it should be according to its cooling rate. Along the x and y axes though, for a Cartesian grid, the grid cells are closer together than along the diagonals, leading to an effective smaller distance over which the shock can compress the gas in one timestep. Thus along the x and y axes the fluid can be compressed slightly faster, then the critical overdensity can be achieved earlier and the instability arises earlier. As mentioned in previous sections, we have performed a test run with 8192^2 resolution for comparison, but have not been able to suppress this feature. However, the faster growth of

Chapters 6 and 7 are an adaptation of the results section from Ntormousi et al. (2011).

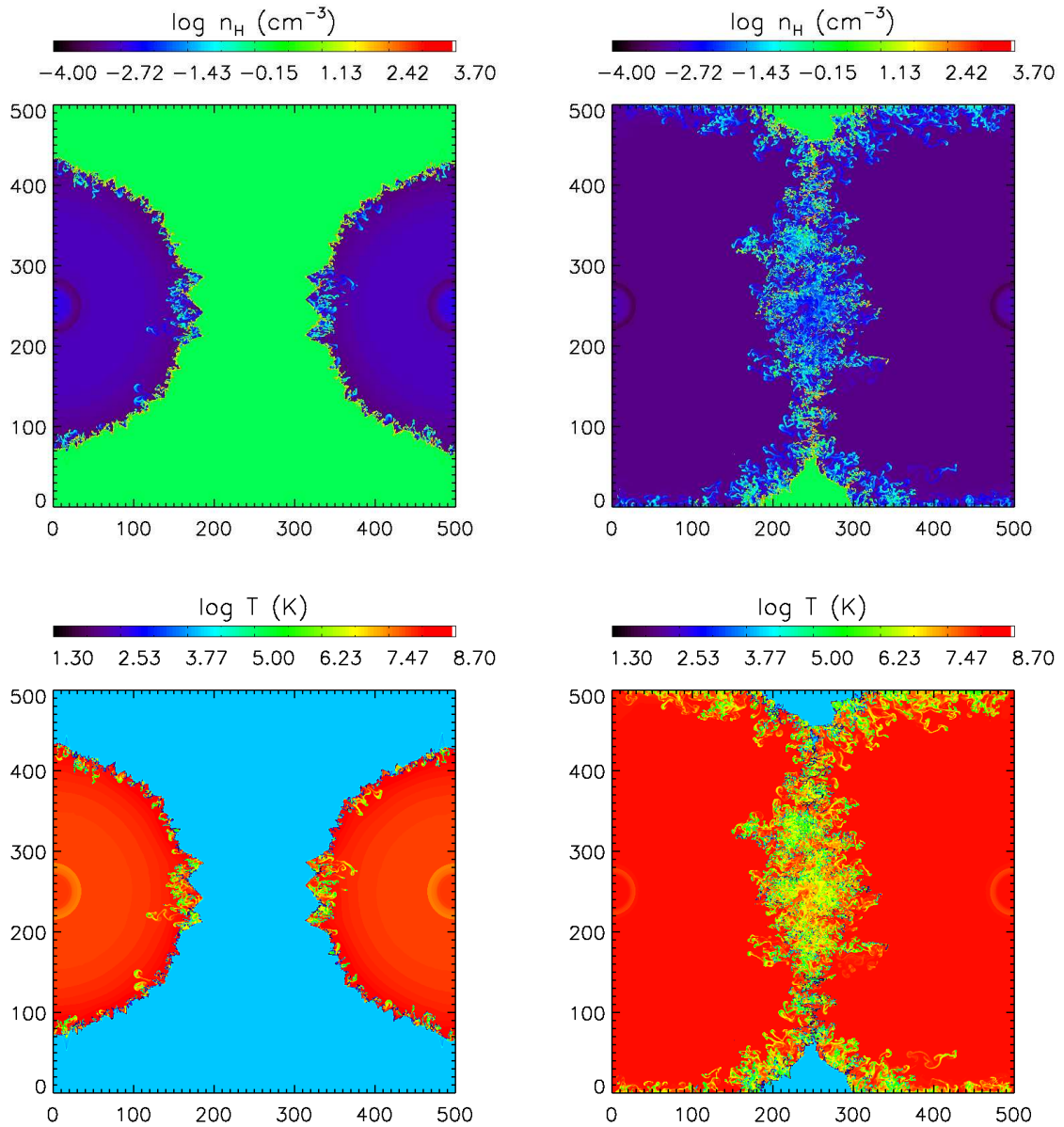


Figure 6.1: Superbubble collision snapshots in a uniform diffuse medium. Plotted on the top panels is the logarithm of the hydrogen number density in $\log(\text{cm}^{-3})$ and on the bottom panels the logarithm of the gas temperature in $\log(\text{K})$. Left: 3 Myrs after star formation, right: 7 Myrs after star formation

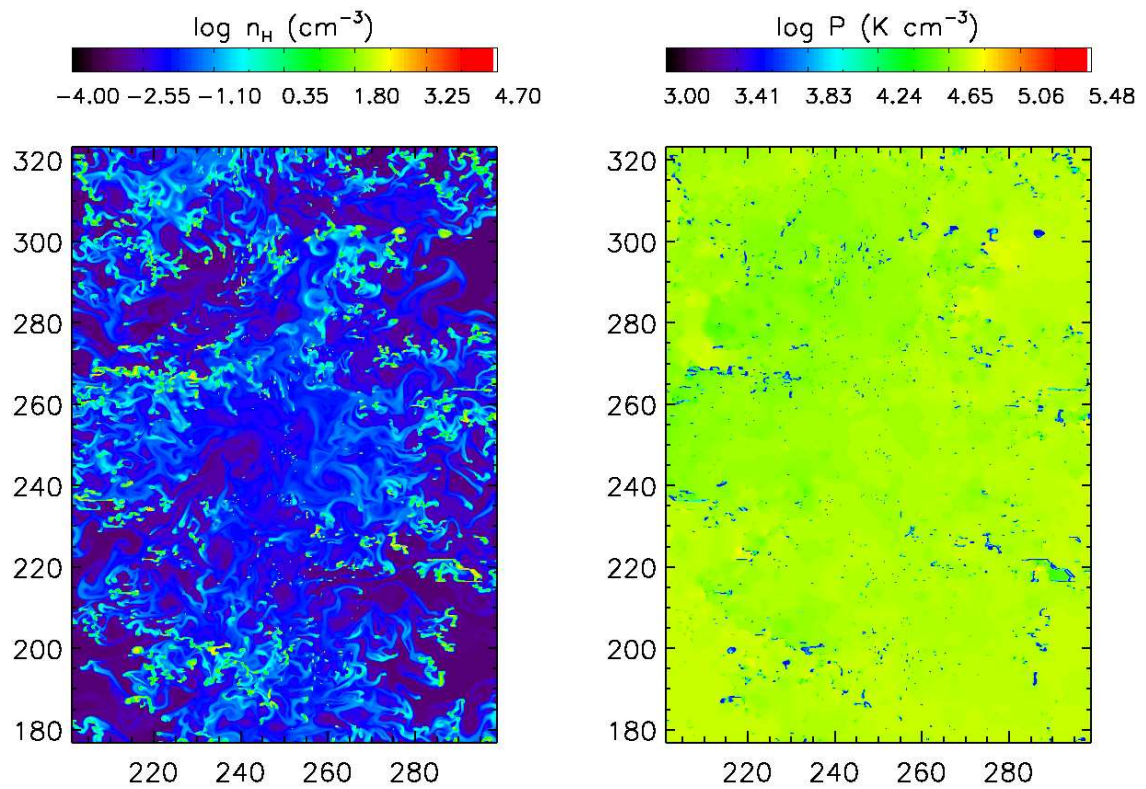


Figure 6.2: Zoom-in of the last snapshot (7 Myrs after star formation) of the uniform diffuse medium run. Plotted on the left is the logarithm of the hydrogen number density in $\log(\text{cm}^{-3})$ and on the right the logarithm of the gas pressure in $\log(\text{K cm}^{-3})$. The axes coordinates are in parsecs.

the instability along these two lines does not affect the average clump formation time and the clump properties in any measurable way.

We mentioned above that the resulting cold and dense structures are a result of the Thermal Instability. However, our simulations do not include thermal conduction and therefore cannot, by definition, fulfill the "Field criterion". This criterion sets the resolution necessary for a proper simulation of the Thermal Instability. It essentially states that, in order to accurately represent the smallest structures created by the TI, one needs to resolve the "Field length", λ_F with at least three grid cells. The Field length is defined as:

$$\lambda_F = \left(\frac{\kappa T}{\rho^2 \Lambda} \right)^{1/2}$$

, where κ is the coefficient of thermal conductivity of the fluid and Λ is the cooling rate of the gas per unit time. Simulations that do not include thermal conduction may be susceptible to artificial phenomena near the resolution limit with no apparent convergence with increasing resolution, since thermal conduction has a stabilizing effect against the Thermal Instability (Koyama & Inutsuka, 2004).

This stabilization is discussed in Burkert & Lin (2000), who studied the Thermal Instability both analytically and numerically for a generic, power-law cooling function. They find that density perturbations below a certain wavelength are always damped by thermal conduction. This wavelength depends on the shape of the cooling function, and in our case would be roughly 4 times the Field length. For typical warm ISM values, that is, a thermal conductivity of about 10^4 ergs cm^{-1} K^{-1} sec^{-1} , a temperature of $T=8000$ K and a hydrogen number density of $n=1$ cm^{-3} , and for a cooling rate of 10^{-26} ergs sec^{-1} , the Field length is about 0.03 pc and four times this length is about our resolution limit. This means that, even though our resolution is marginal for resolving the smallest unstable fluctuations, higher resolution without the explicit inclusion of thermal conductivity would produce artificially small structure. Of course, for lower temperatures and higher densities the Field length is much smaller, so unstable density fluctuations due to Thermal Instability within our clumps are not resolved.

Figure 6.2 shows a close-up of the last snapshot of this run, in logarithm of density and pressure. It is evident from this Figure that all clumps have lower pressures with respect to the rest of the gas.

Clumps are identified by selecting locations with hydrogen number density greater than 50 cm^{-3} and temperature smaller than 100 K and using a friends-of friends algorithm to link such adjacent locations together. This group of cells is then identified as a single clump. The density and temperature threshold is clearly an approximation, to account for the fact that these simulations do not include molecule formation and the cooling function we are using assumes optically thin gas. For the following analysis only structures which contain more than 16 cells are considered. Smaller structures do not contain sufficient information and are disregarded as under-resolved.

Figure 6.3 shows the gas phase diagram at the end of the simulation. The plot shows all the gas in the simulation, color-coded to its corresponding mass fraction in the simulated box. The solid line is the cooling-heating equilibrium curve for the warm and cold gas and the red crosses are average clump properties. As an indication for the gas temperatures, three isotherms have been overplotted. Most of the gas mass seems to be in the cold phase (– see also Figure 6.4), but there is also about 14% of the gas mass in the warm, thermally

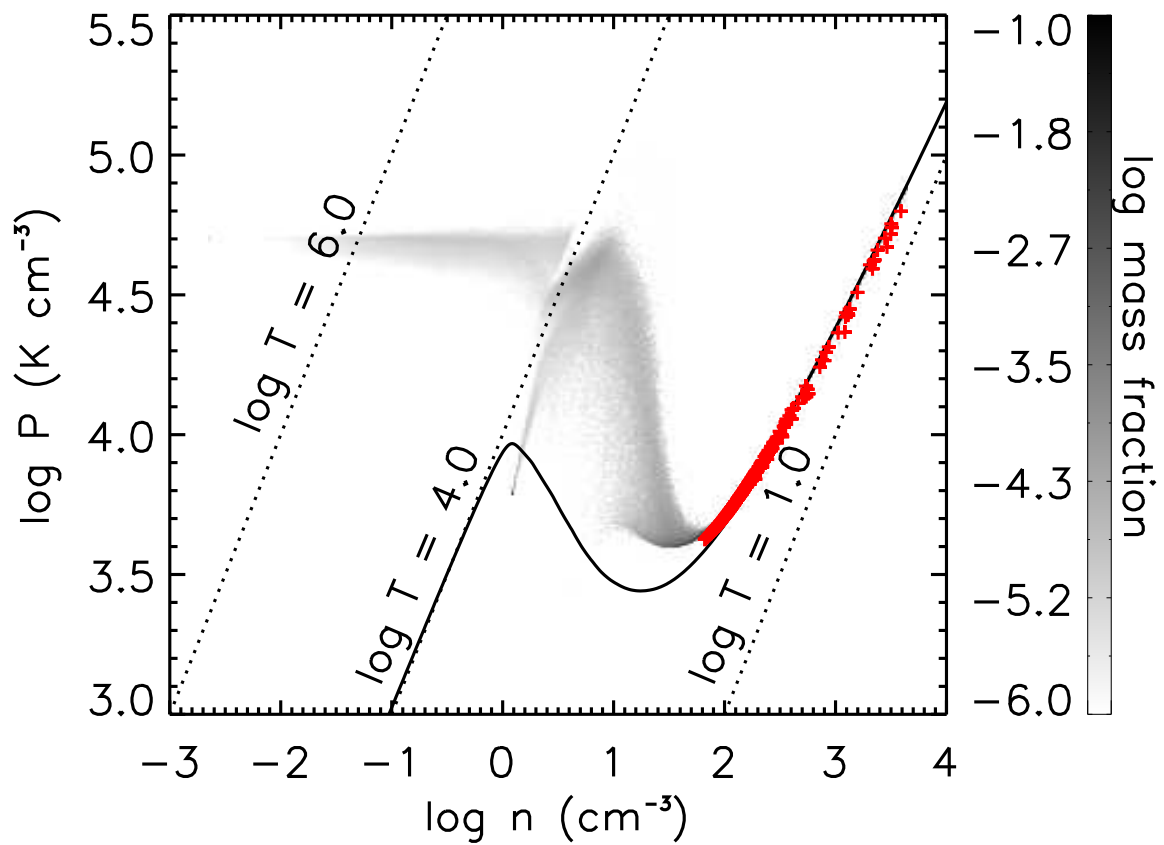


Figure 6.3: Pressure versus hydrogen density of the fluid in the box for the uniform medium run. The plot is from the last snapshot, 7 Myrs after star formation. The gas has been binned and color-coded according to the mass fraction it represents. The solid line is the cooling-heating equilibrium curve for the warm and cold gas and the dashed lines show the locations of three isotherms. Red crosses are average clump quantities.

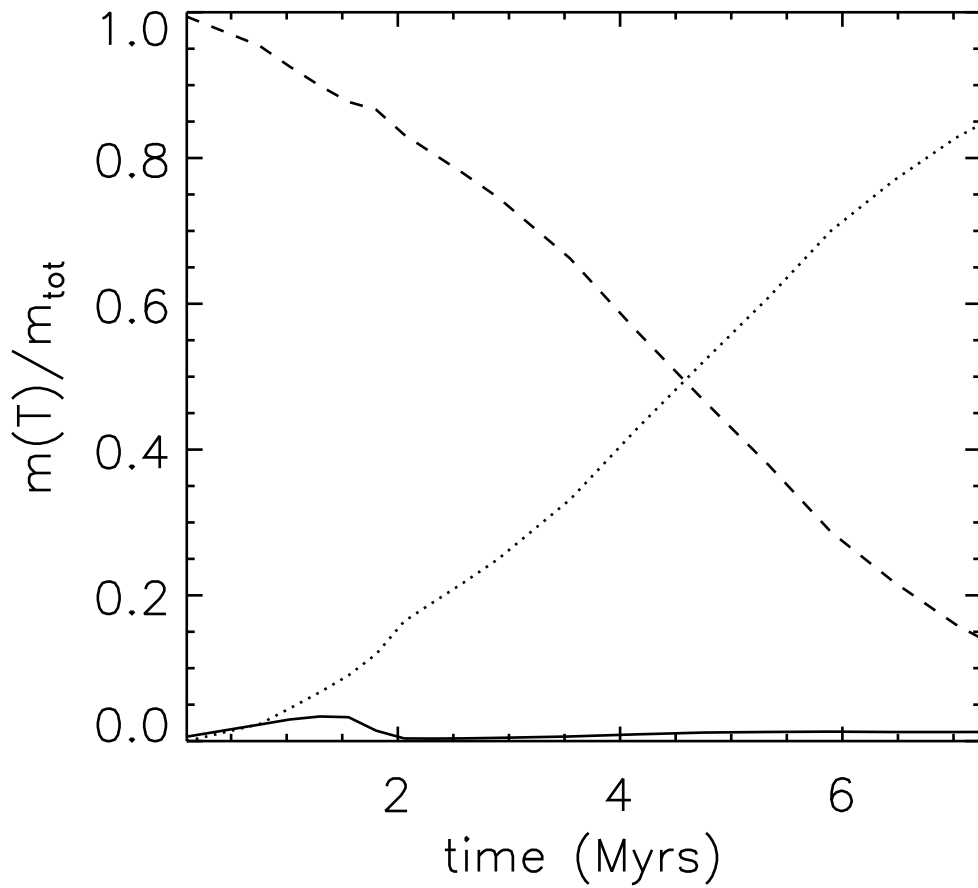


Figure 6.4: Gas fractions with time for the uniform medium run. The dashed curve shows the mass fraction in the warm gas phase, the solid curve shows the mass fraction in the hot gas phase and the dotted curve the mass fraction in the cold phase. (Hot phase: gas with $T \geq 25000K$, warm phase: gas with $100K < T < 25000K$, cold phase: gas with $T \leq 100K$)

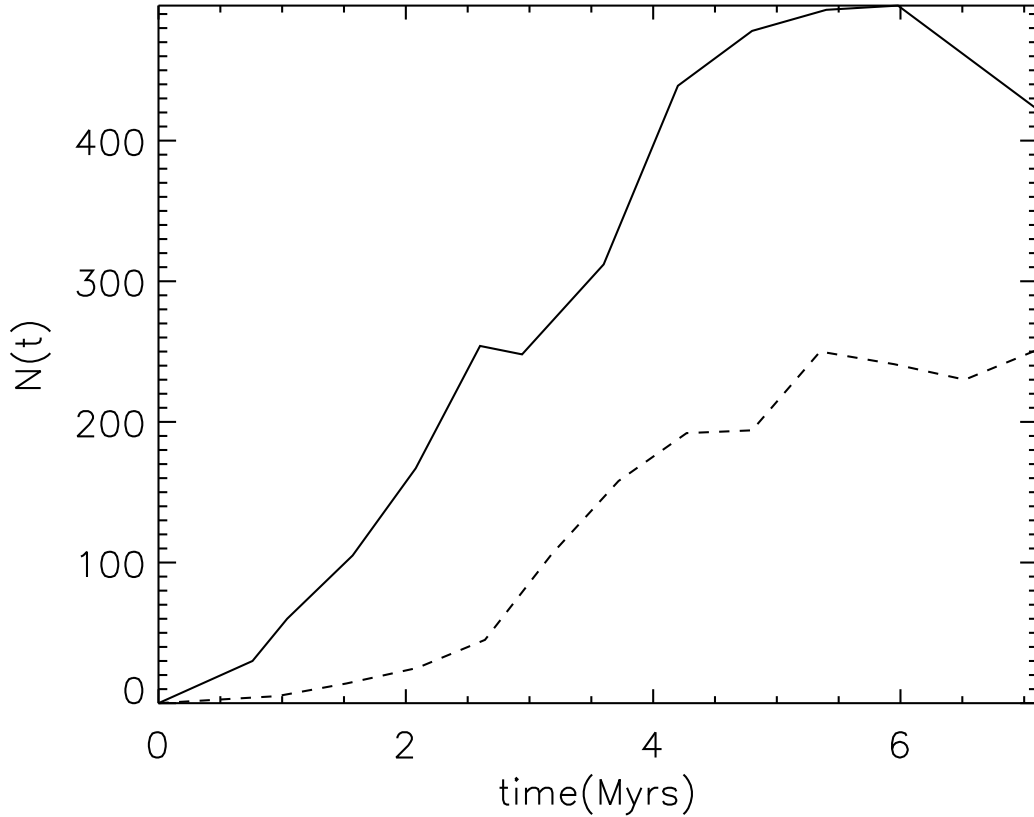


Figure 6.5: Number of identified clumps with time. Clumps were only counted if they included more than 16 dense and cold cells. The solid curve corresponds to the run in a uniform diffuse medium, while the dashed curve to the run in a turbulent diffuse medium.

unstable regime. This gas is pushed from the stable to the unstable regime by the momentum inserted by the wind. Some of this thermally unstable gas is located around the cold clumps, forming a warm corona. We will return to this in the following chapter. The clumps lie on the equilibrium curve, as does the coldest gas, as expected from clumps formed by the Thermal Instability.

Figure 6.4 shows the mass fraction of the gas in each phase of the gas with time. We define cold gas as gas with temperatures $T < 100K$, warm gas to lie in the temperature regime of $100K < T < 25000K$ and hot gas to have temperatures $T > 25000K$. The simulation starts with almost entirely warm gas in the box. As time goes by more and more cold gas is created. Since the hot gas is very dilute, it only amounts to approximately 1 percent of the mass throughout the simulation. In the end of the simulation we have approximately 85 per cent of the mass in cold clumps and 14 percent in the warm phase. The mass injected by the OB association amounts to less than 10^{-5} of the total mass in the domain throughout the simulation.

Figure 6.5 shows the total number of identified clumps with time for each simulation. At the end of this simulation more than 400 clumps have formed. This is not due to the new clumps formed by the TI, but also due to the fragmentation of already existing clumps.

6.2 Shell collision in a turbulent diffuse medium

In the same way as in the case of a uniform medium, here as well we observe the formation of cold and dense structures from the combined action of the NTSI, the Kelvin-Helmholtz and the Thermal Instability. The main difference in this case is the anisotropy caused by the turbulent density and velocity field to the formation of clumps, as illustrated in Figure 6.6. The shell on the left-hand side fragments very early on in some locations, already at less than 1 Myr after star formation, but the shell on the right-hand side fragments much later, at around 3 Myrs after star formation. Rotating the initial conditions by 180 degrees produces the exactly opposite effect.

This is caused by the difference in the background velocity field and is related to the range in which the Vishniac instability exists (Vishniac, 1994). The smallest and largest unstable wavelength both depend on the relative velocity of the shock-bounded slab, in our case the thin expanding shell, and the background medium. Performing a simple test with a uniform background velocity field indicated that the instability indeed grows first where the relative velocity of the shell with respect to the background medium is largest, in agreement with Vishniac's analysis.

Figure 6.7 shows a zoom-in of the last snapshot. The picture here very similar to that in Figure 6.2; the different gas phases are almost in pressure equilibrium and clumps have a thermal pressure almost an order of magnitude lower than their surroundings.

After the NTSI starts to grow, the condensed material immediately becomes thermally unstable and we witness the formation of cold and dense clumps, as in the case of the uniform medium. However, due to the background velocity field, there are now regions where the NTSI has a faster growth rate with respect to that of a static medium. This leads to a larger Kelvin-Helmholtz shear. This is the reason why in this simulation longer filaments are formed compared to the uniform background medium simulation. Some of these structures are shown in Figures 6.9, 6.10 and 6.11. These figures are zoomed-in fractions of the full domain (Figure 6.8).

By following these filaments from their formation to the end of the simulation, we observe that they become increasingly more elongated and they constantly fragment into smaller clumps. Figure 6.11 shows the time evolution of one of these filaments. Before the shells collide, the structure is a small clump of cold gas. During the collision, this clump gets caught in a large-scale shear and becomes more and more elongated until, at the end of the simulation, it has reached a total length of about 100 pc. Note that during the bubble expansion the clump is not located inside the hot bubble, but rather at the edge of the shock.

The anisotropy in the growth rate of the NTSI leads to the formation of much less clumps in this simulation with respect to the uniform background simulation, as illustrated in Figure 6.5.

Figure 6.12 shows the phase diagram of the gas in this simulation, in the same way as Figure 6.3. There are two main differences with respect to the uniform background medium run; First, the pressure at low densities ($n < 0.1 \text{ cm}^{-3}$) is higher than in the uniform medium run. This can be attributed to the additional compression from the turbulence. Second, we note that the clumps in this simulation are at not only at lower pressures with respect to the hot medium than the clumps in the uniform background run, but are also at lower absolute pressures than those clumps. This can be explained by considering the formation mechanism of the clumps in these simulations. Structures created by the Thermal Instability have lower pressures than their surroundings. When Thermal Instability has stopped acting on them,

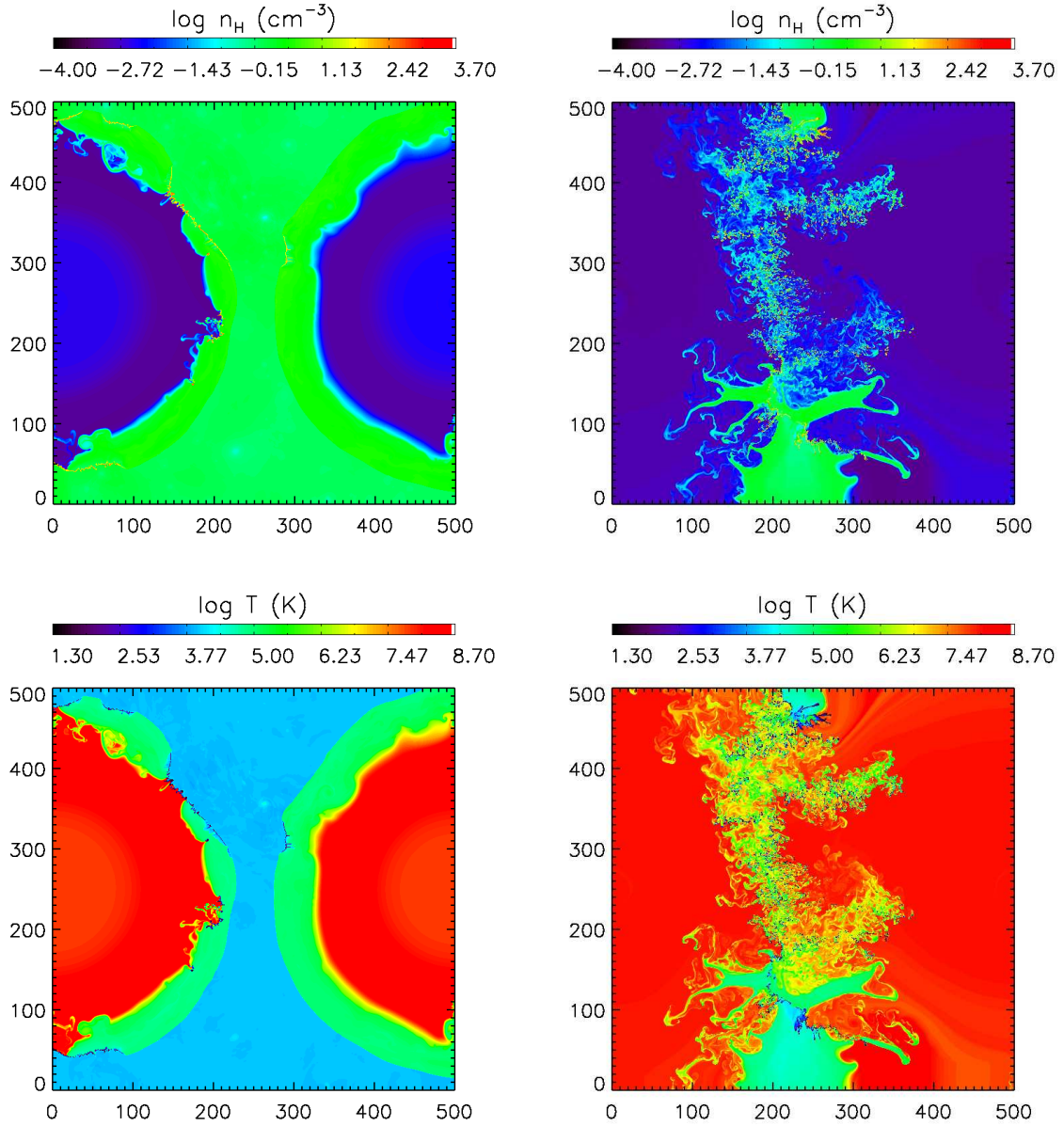


Figure 6.6: Super-bubble collision snapshots in a turbulent diffuse medium. Plotted on the top panels is the logarithm of the hydrogen number density in $\log(\text{cm}^{-3})$ and on the bottom panels the logarithm of the gas temperature in $\log(\text{K})$. Left: 3 Myrs after star formation, right: 7 Myrs after star formation.

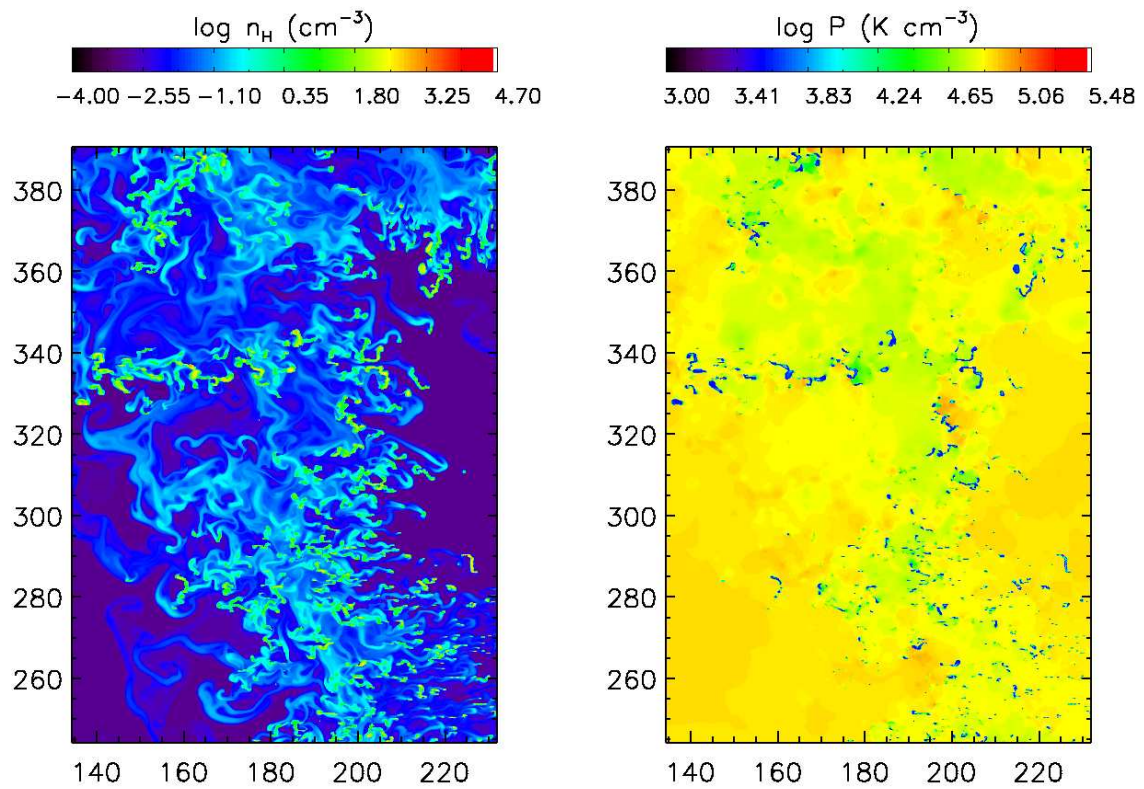


Figure 6.7: Zoom-in of the last snapshot (7 Myrs after star formation) of the turbulent diffuse medium run. Plotted on the left is the logarithm of the hydrogen number density in $\log(\text{cm}^{-3})$ and on the right the logarithm of the gas pressure in $\log(\text{K cm}^{-3})$. The axes coordinates are in parsecs.

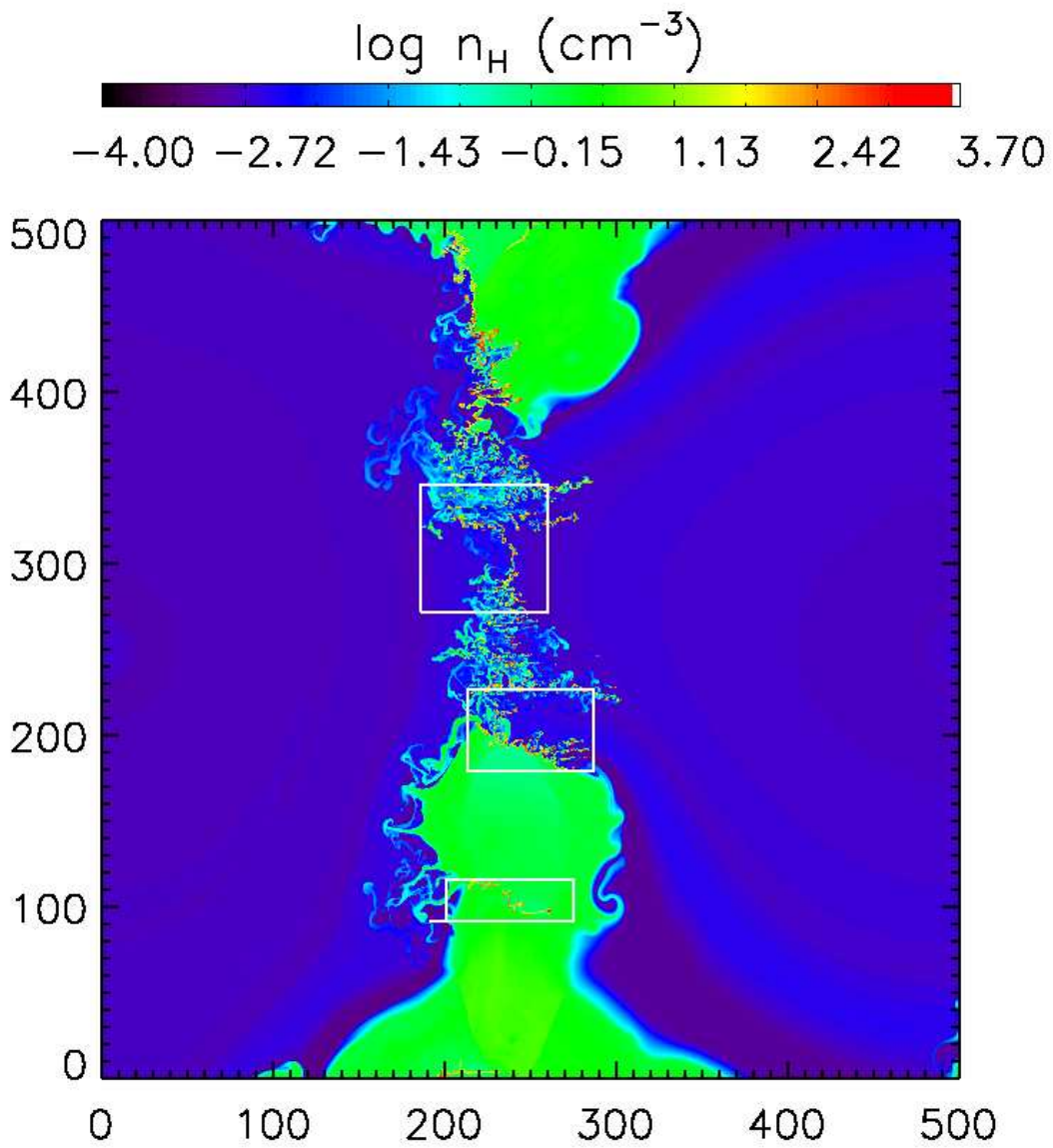


Figure 6.8: Simulation snapshot at $t=5.3$ Myrs after star formation. Plotted here is the logarithm of the hydrogen number density. The axes are marked in parsecs. The black rectangles show the positions of the filaments shown in figures 6.9, 6.10 and the 5.3 Myrs snapshot of figure 6.11

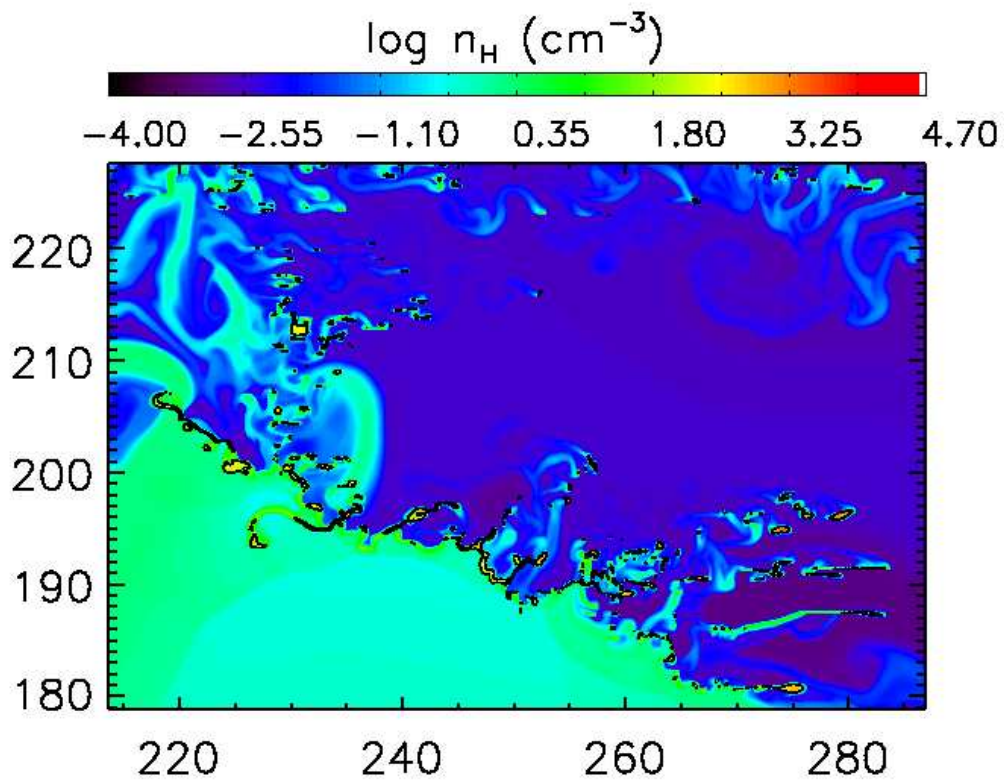


Figure 6.9: A large filament containing several smaller clumps. Plotted here is the logarithm of the hydrogen number density in $\log(\text{cm}^{-3})$. The snapshot corresponds to the white box centered at $x=250$ pc, $y=200$ pc in the $t=5.3$ Myrs snapshot shown in figure 6.8. The axes are marked in parsecs from the axes origin. The black contour corresponds to $n_H = 50\text{cm}^{-3}$

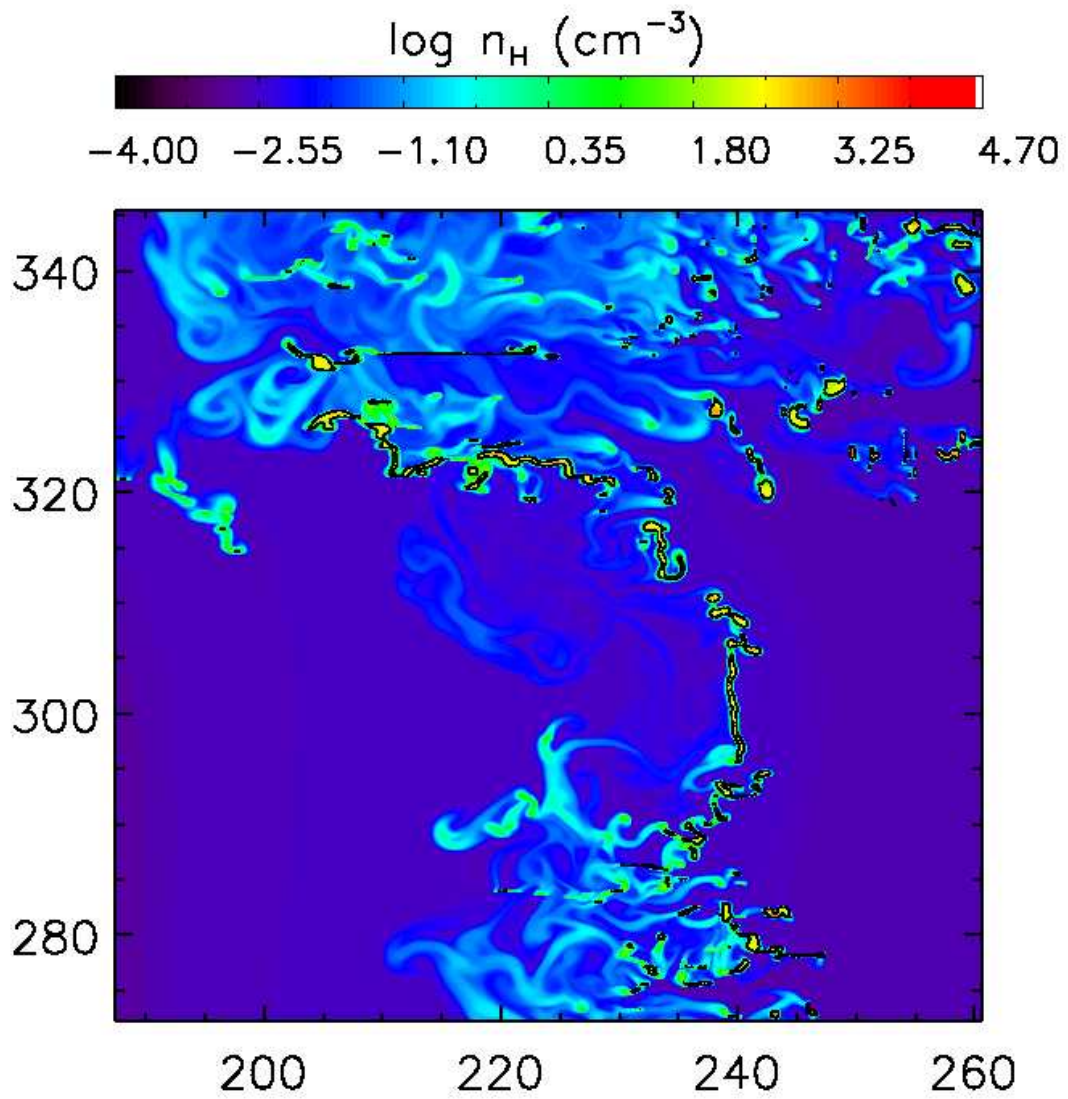


Figure 6.10: As in figure 6.9. The snapshot corresponds to the white box centered at $x=225$ pc, $y=314$ pc in the $t=5.3$ Myrs snapshot shown in figure 6.8.

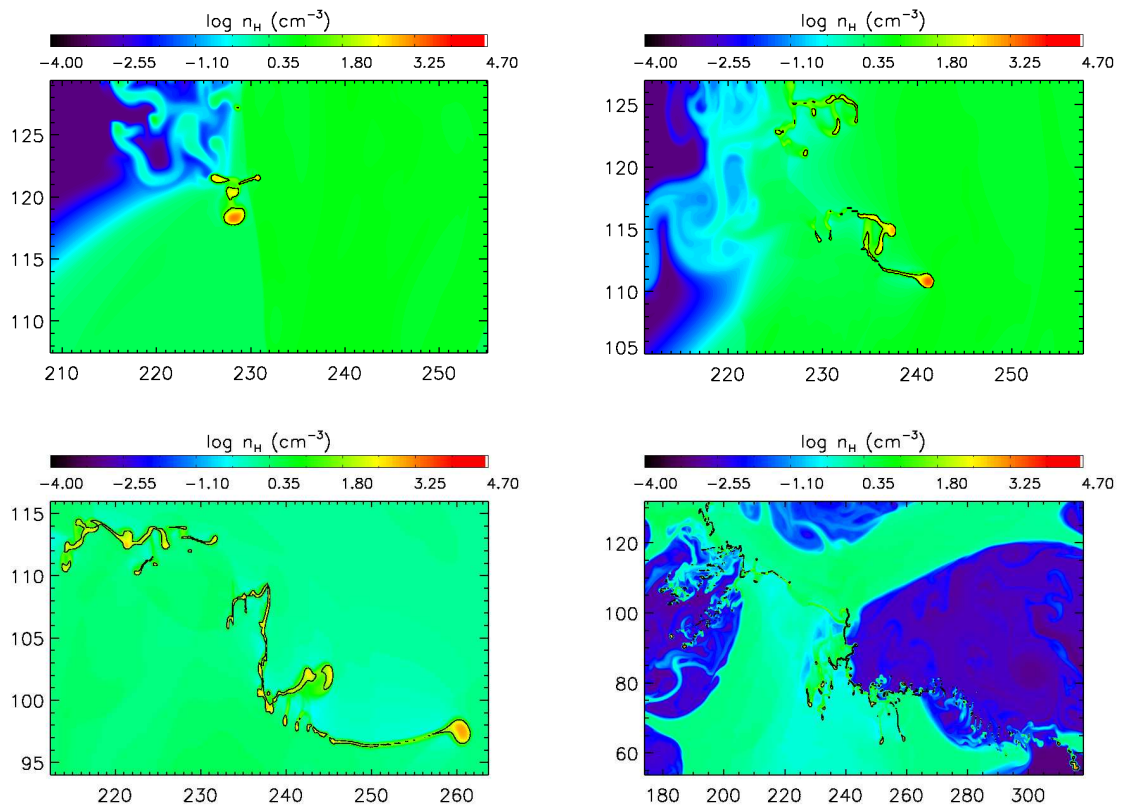


Figure 6.11: Time evolution of a single filament. The plots show logarithm of hydrogen number density. The black contour shows the level $n_H = 50 \text{ cm}^{-3}$. From top left to bottom right: 4.3, 4.6, 5.3 and 7 Myrs after star formation. Note the change in scale between the snapshots.

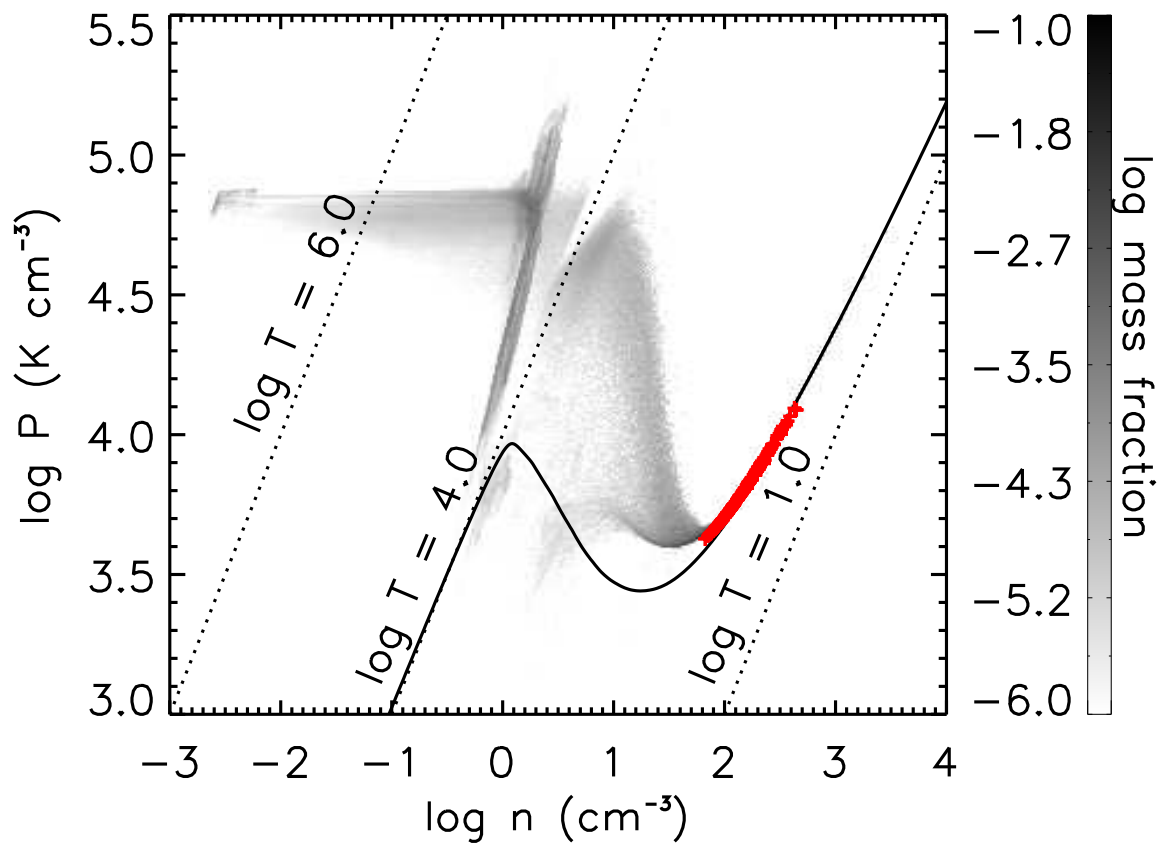


Figure 6.12: Pressure versus hydrogen density of the fluid in the box for the turbulent medium run. The plot is from the last snapshot, 7 Myrs after star formation. The gas has been binned and color-coded according to the mass fraction it represents. The solid line is the cooling-heating equilibrium curve for the warm and cold gas and the dashed lines show the locations of three isotherms. Red crosses are average clump quantities.

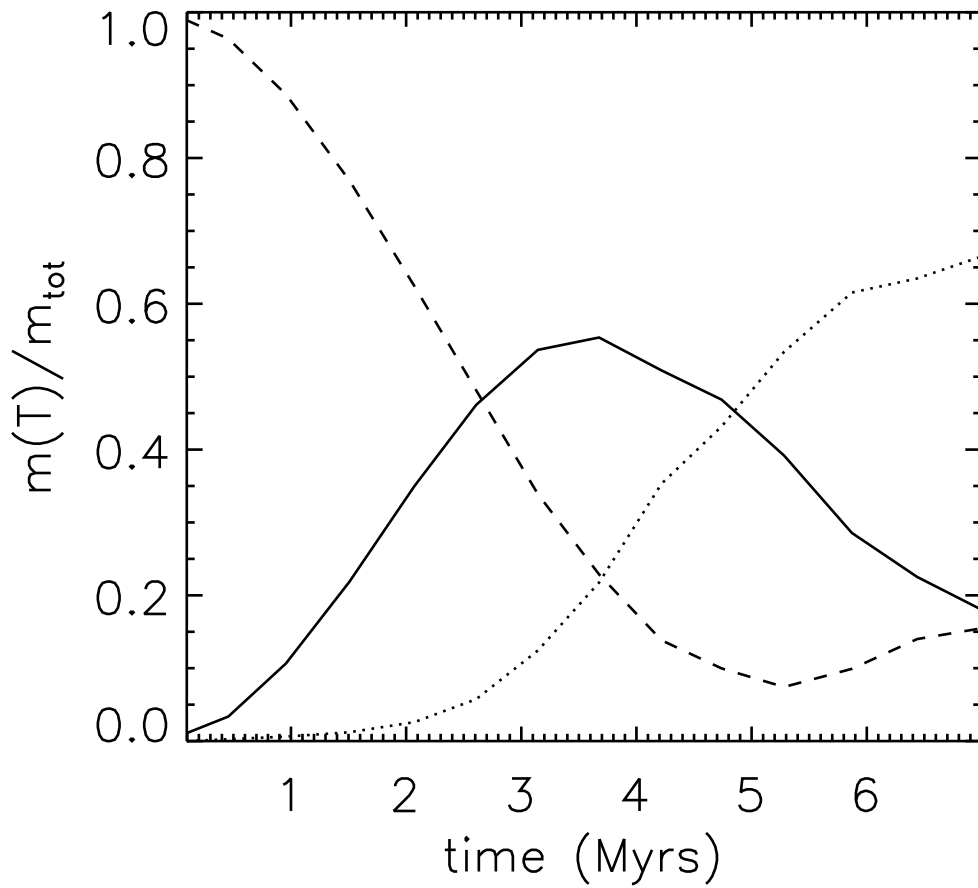


Figure 6.13: Gas fractions with time for the turbulent medium run. The dashed curve shows the mass fraction in the warm gas phase, the solid curves shows the mass fraction in the hot gas phase and the dotted curve the mass fraction in the cold phase. (Hot phase: gas with $T \geq 25000K$, warm phase: gas with $100K < T < 25000K$, cold phase: gas with $T \leq 100K$)

they move towards pressure equilibrium with the surrounding medium in approximately a sound crossing time, c_s/L , where c_s the sound speed and L the typical size of these clumps. For a typical density of 10^{-21} g/cm³ and a typical temperature of 50 K, the sound speed in these clumps is about 0.8 km/sec. At this velocity sound waves will cross a 2 pc long clump in about 0.6 Myrs. In the turbulent diffuse background run, clumps are formed later than in the uniform background run, which means they are less evolved and farther from equilibrium. According to the above calculations, the time difference between clump formation between the two simulations is about 3 sound crossing times, which is enough for many the clumps in the uniform diffuse background simulation to have reached approximate pressure equilibrium with the hot medium.

Figure 6.13 shows the evolution of the mass fractions of the gas in different temperature regimes. Unlike the previous run, in this simulation there is a maximum in the hot gas mass fraction at about 3.5 Myrs after star formation and a later minimum of the warm gas fraction at around 5 Myrs after star formation. This can be explained by the delayed formation of cold gas in this simulation. Until the cold gas is formed, the hot gas just compresses the warm gas. Then the hot gas mass fraction increases, while the warm gas mass fraction decreases. When cold gas starts to form, it quickly dominates the mass, causing the warm and hot mass fractions to drop.

Morphological features of the cold clumps

7.1 General

Figure 6.5 shows that we form hundreds of clumps in each snapshot of the simulations. This makes it very difficult to study each of them in detail, especially since they are constantly merging and splitting. However, we can make some general comments on the morphology of the identified clumps and look into some of their properties.

Clumps are generally at lower pressures with respect to their surrounding gas (– see Figures 7.1, 7.2 7.3 and 7.4). This means that the Thermal Instability is still acting in these regions, causing them to condense further. Two examples of condensing clumps are shown in Figure 7.1. Others (about 11% in the last snapshot of the uniform background run and 16% in the turbulent background run) are rotating. Two examples of rotating structures are shown in Figure 7.2. Rotation is either combined with compression or it introduces a centrifugal force which makes the clump expand. Of the rotating cores in the last snapshots of the uniform and the turbulent background runs, about 25% and about 35% respectively are at the same time condensing and the rest are expanding. In very few cases, less than 1%, the centrifugal force exactly balances the force due to the pressure difference between the interior and the exterior of the clump.

A small fraction of the identified clumps are in pressure equilibrium with their surroundings, at least at their most central parts. These clumps do not tend to host significant internal motions (– Figure 7.4).

All clumps are surrounded by a warm corona which is more dilute than their cold central regions and at an intermediate pressure between their pressure and the one of the surrounding gas. This corona usually surrounds more than one clump, indicating that they are parts of larger structures, such as the ones illustrated in Figures 6.9, 6.10 and 6.11.

In the following we focus on the velocity dispersions, sizes and possible evolution of the clumps.

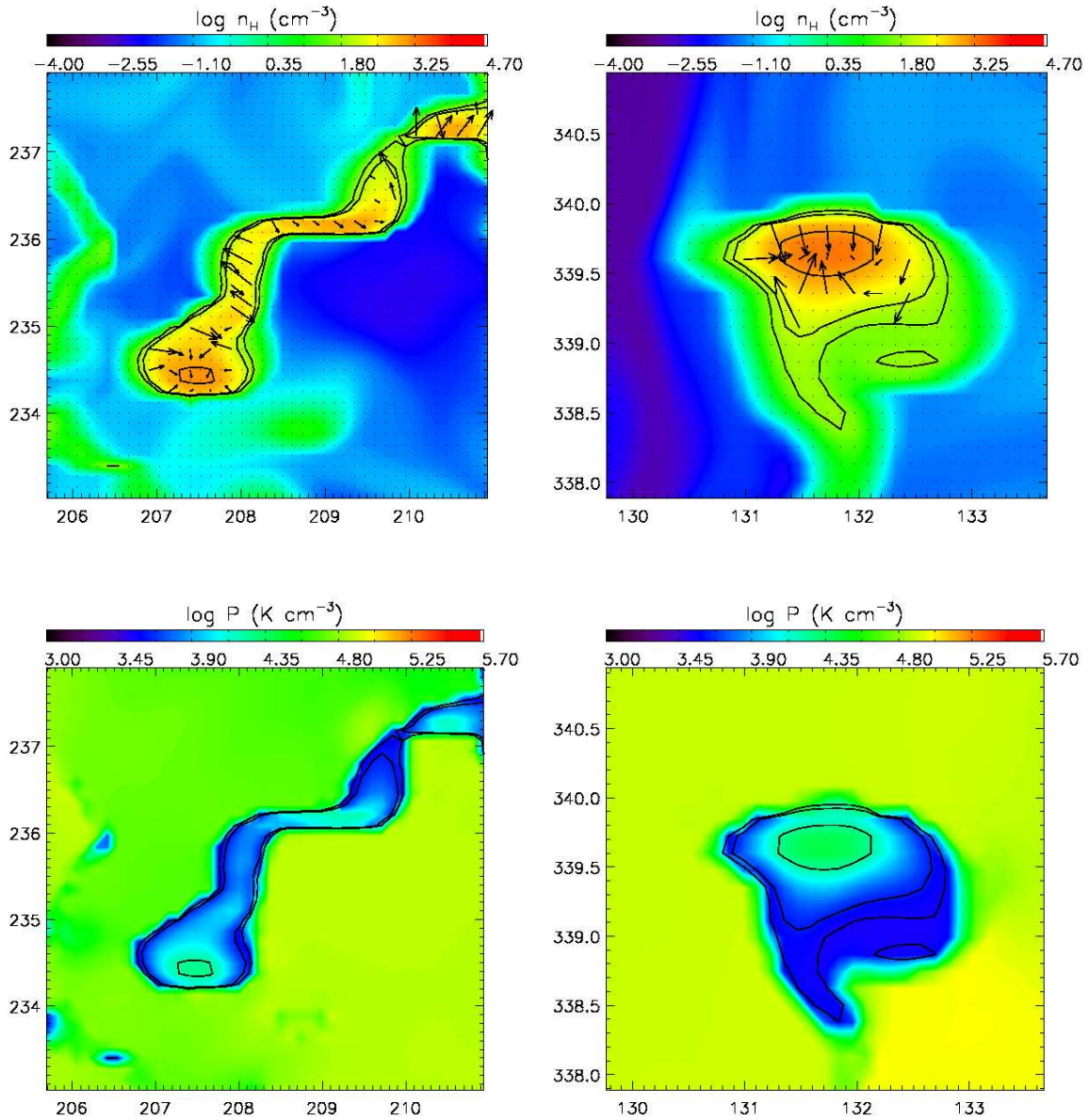


Figure 7.1: Two examples of condensing clouds. Top panels show the logarithm of hydrogen number density in $\log(\text{cm}^{-3})$ and bottom panels show the logarithm of thermal pressure in $\log(\text{K cm}^{-3})$. The black arrows show the velocity field with the mean velocity of the central clump subtracted. Overplotted in black are the contour levels for n_H equal to 50 cm^{-3} , 100 cm^{-3} and 1000 cm^{-3} .

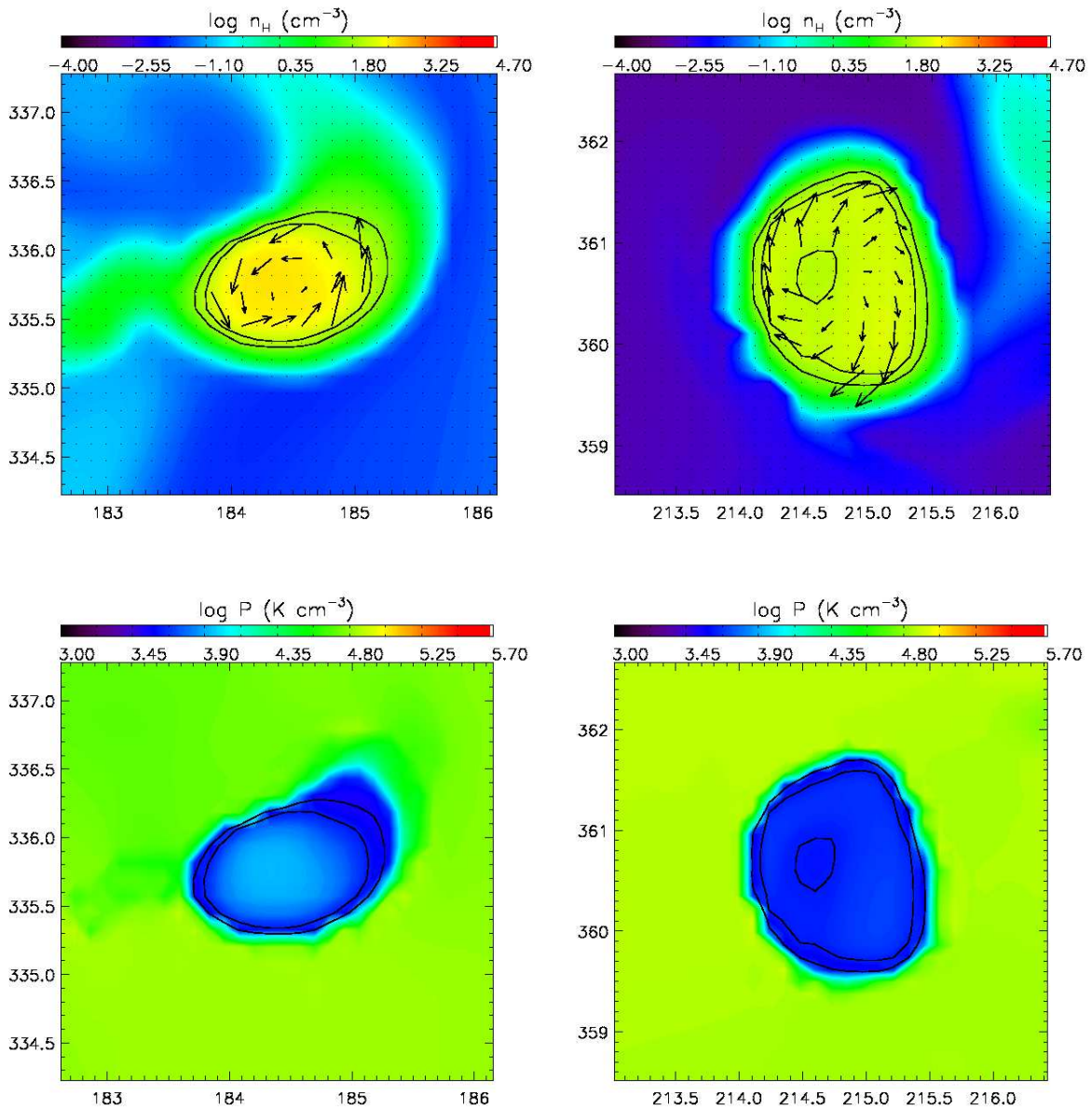


Figure 7.2: Two examples of rotating clumps. Top panels show the logarithm of hydrogen number density in $\log(\text{cm}^{-3})$ and bottom panels show the logarithm of thermal pressure in $\log(\text{K cm}^{-3})$. The black arrows show the velocity field with the mean velocity of the central clump subtracted. Overplotted in black are the contour levels for n_H equal to 50 cm^{-3} , 100 cm^{-3} and 1000 cm^{-3} .

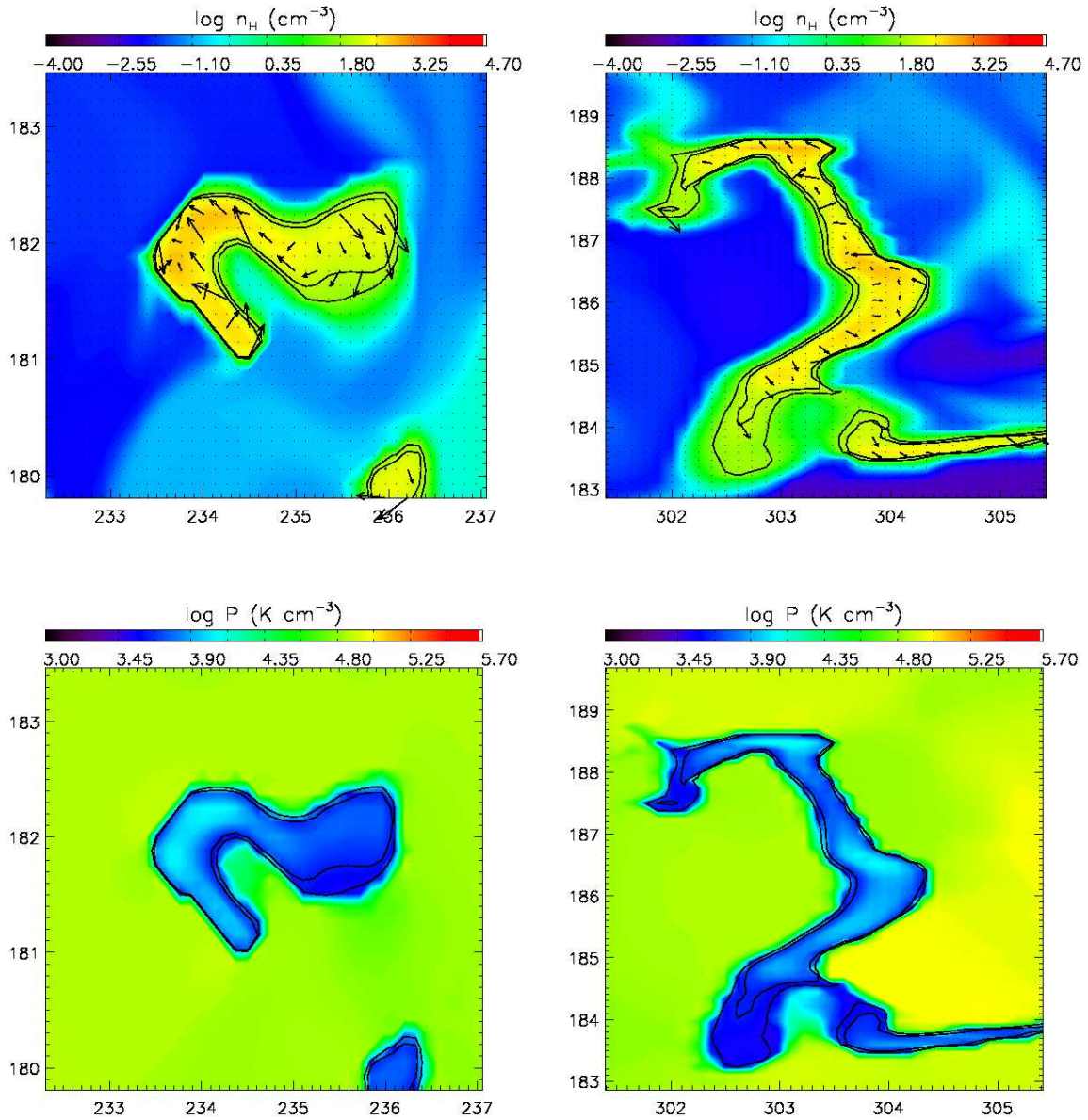


Figure 7.3: Two examples of clumps hosting random motions. Top panels show the logarithm of hydrogen number density in $\log(\text{cm}^{-3})$ and bottom panels show the logarithm of thermal pressure in $\log(\text{K cm}^{-3})$. The black arrows show the velocity field with the mean velocity of the central clump subtracted. Overplotted in black are the contour levels for n_H equal to 50 cm^{-3} , 100 cm^{-3} and 1000 cm^{-3} .

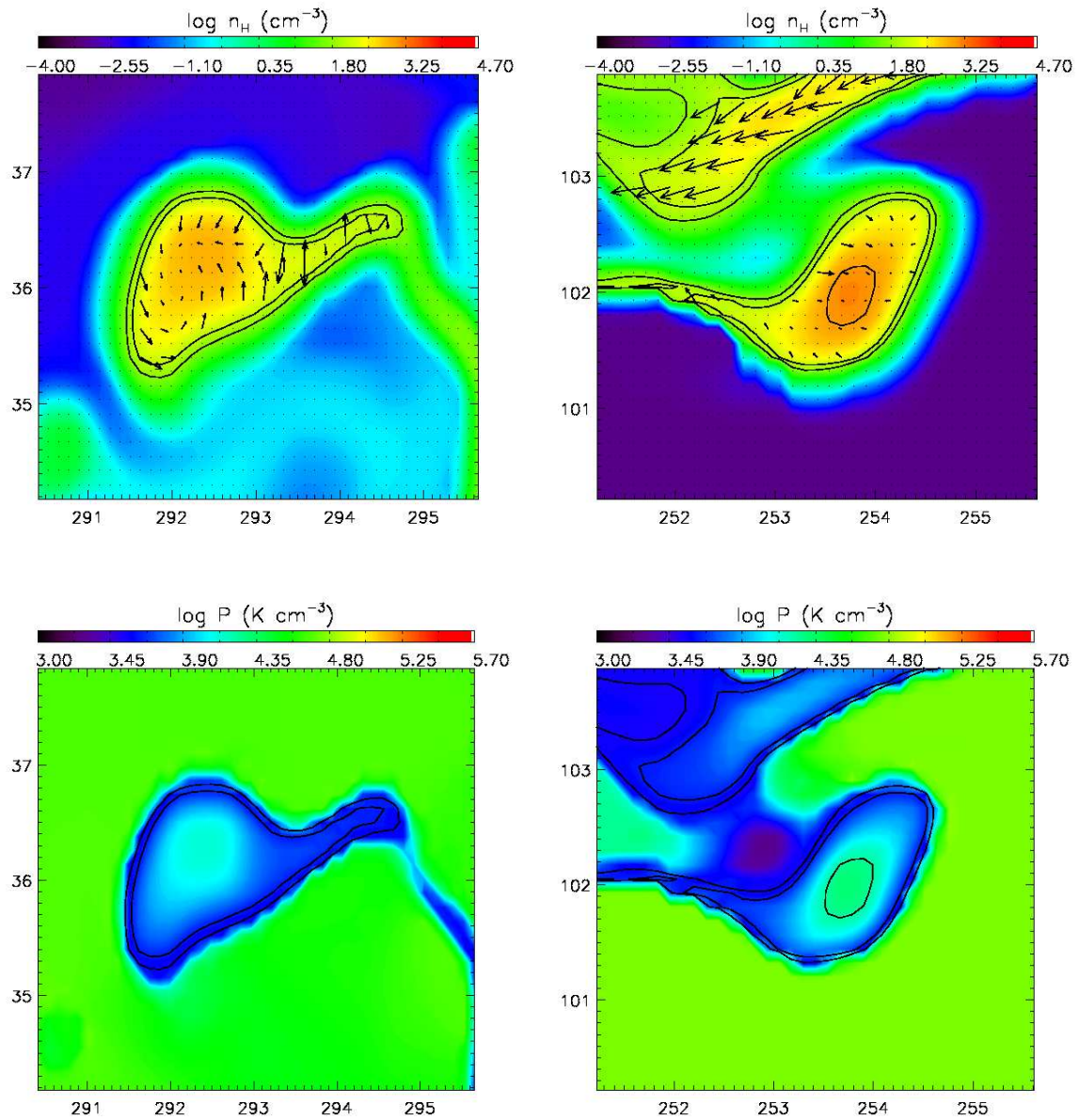


Figure 7.4: Two examples of clumps with small internal velocities. Top panels show the logarithm of hydrogen number density in $\log(\text{cm}^{-3})$ and bottom panels show the logarithm of thermal pressure in $\log(\text{K cm}^{-3})$. The black arrows show the velocity field with the mean velocity of the central clump subtracted. Overplotted in black are the contour levels for n_H equal to 50 cm^{-3} , 100 cm^{-3} and 1000 cm^{-3} .

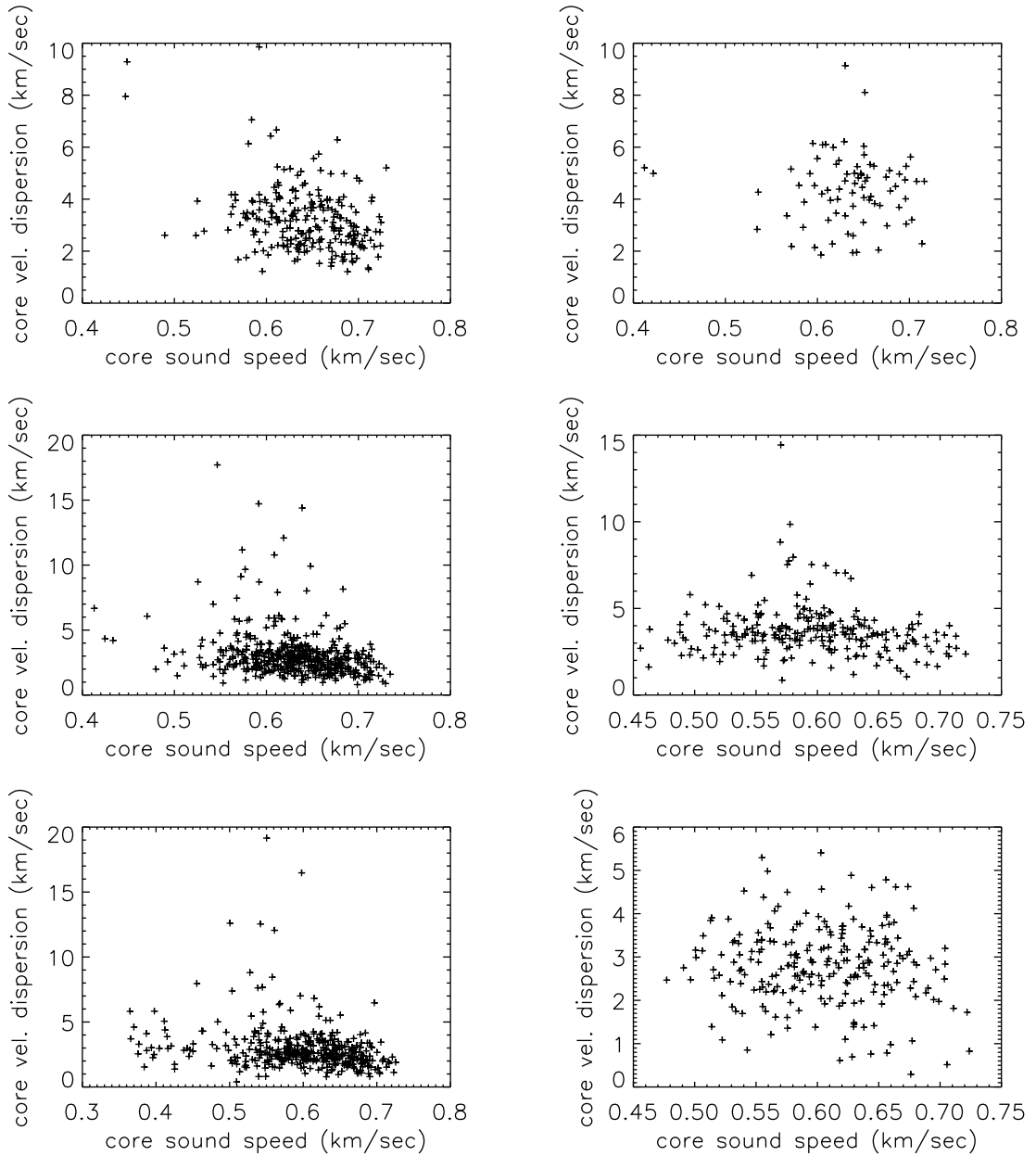


Figure 7.5: Clump internal velocity dispersion versus their sound speed at different times. From top to bottom, 3, 5 and 7 Myrs after star formation. The left panel corresponds to the uniform background medium run, the right panel to the turbulent background medium run.

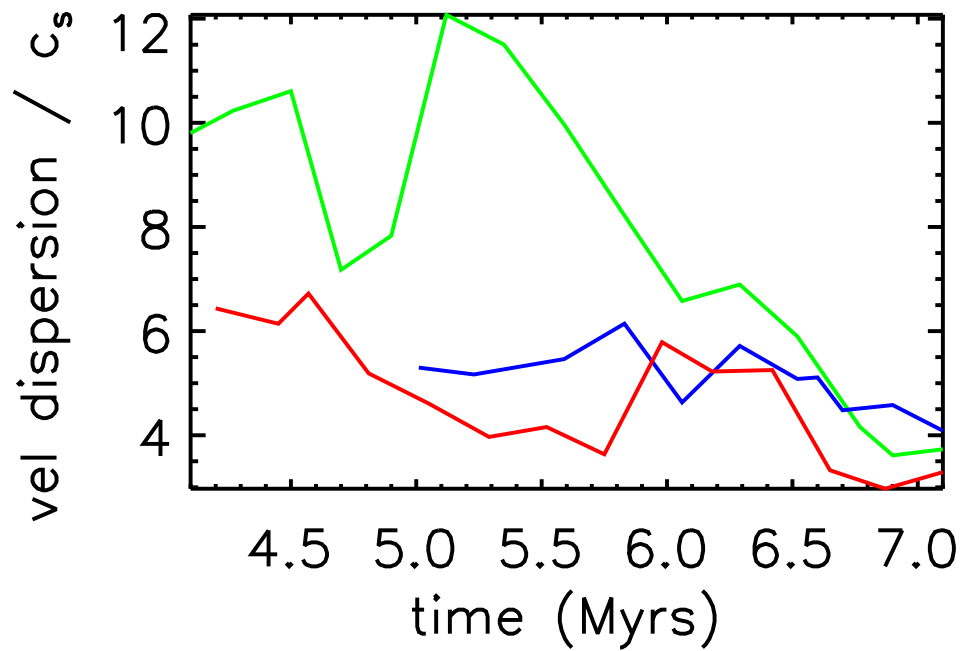


Figure 7.6: Time evolution of the velocity dispersions over sound speed for three isolated cores. The green line corresponds to a condensing clump, the blue line to a rotating clump and the red line to a clump with random motions. The data for each clump begin from the snapshot where we can still identify the clump as being the same.

7.2 Velocity dispersions

Figure 7.5 shows the internal velocity dispersions of the clumps at different times for both simulations. The velocity dispersion in this context is defined as the square root of the variance among all locations which compose the clump. This means that for many clumps a velocity dispersion may indicate rotation, compression, expansion or random motions. As random motions here we define any combination of rotation and compression or expansion. Since the clumps have no significant internal density fluctuations, mass-weighted velocity dispersions are not very different from the ones presented here.

Although many of the formed clumps host supersonic motions in their interior at all times, there is an indication that these motions decrease at later times, as shown in the velocity dispersion plot of the last snapshots. This effect seems slightly more pronounced for the turbulent background run, where the largest internal velocity dispersions have disappeared in the last snapshot.

In the case of compression or expansion, this means that the clumps gradually move to pressure equilibrium with their surrounding gas. In the case of random motions, it indicates that these motions were inherited by the turbulent environment that created the clumps but, in absence of any mechanism to sustain them, they die out. In the case of rotation, though, the situation is a bit more complicated. Rotation could be an effect of the large-scale Kelvin-Helmholtz shear, it can originate from Thermal Instability accretion or can be a result of structures splitting or merging. Angular momentum conservation sustains these motions for longer, so we would only expect them to decrease on a viscous timescale.

In order to study if the decrease in internal velocity dispersion is observable for individual clumps, we tracked some of them back in time and plotted their velocity dispersion evolution. Since dense structures are created all the time and clumps merge or split at each snapshot, it is very difficult to construct an algorithm able to automatically identify a clump in different snapshots. Instead we identified the clumps by eye according to their positions and translational velocities. We focus here on three examples: a rotating clump, a contracting clump and a clump with random internal motions. Their velocity dispersions over their corresponding sound speed as a function of time are shown in Figure 7.6. Since clumps evolve almost isothermally, their sound speed does not vary significantly during the interval shown in the plot. The green line corresponds to a contracting clump, the blue line to a rotating clump and the red line to a clump with random motions. All three clumps show some decrease in velocity dispersion with time. Although we are not able to make a complete study at this stage, we observe that the rotating clump practically maintains the same velocity dispersion throughout its existence, showing only a slight decrease, while the condensing clump and the clump with random motions show a decrease in velocity dispersion. For the condensing clump this decrease is especially pronounced.

7.3 Sizes

Figure 7.7 shows the size distribution of the clumps at different times for both simulations. The sizes are calculated as the square root of the area occupied by the clump. Although we do not form clumps larger than approximately 3 pc, the maximum clump length can reach about 10 pc. This means that structures may have one very large dimension, but they occupy a very small area.

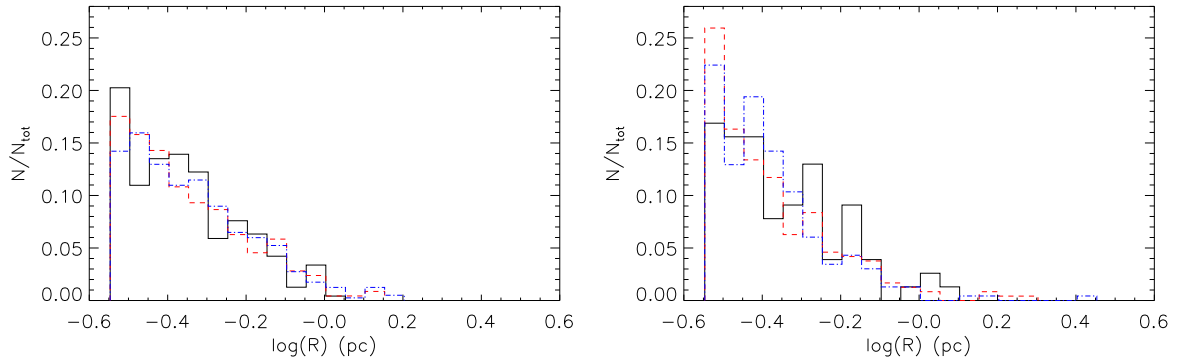


Figure 7.7: Clump size distributions in parsecs at different times. The plot on the left-hand side corresponds to the run in a uniform diffuse medium and the plot on the right to the run in a turbulent diffuse medium. The solid black, dashed red and dash-dotted blue histograms correspond to the 3 Myrs, 5 Myrs and 7 Myrs, respectively.

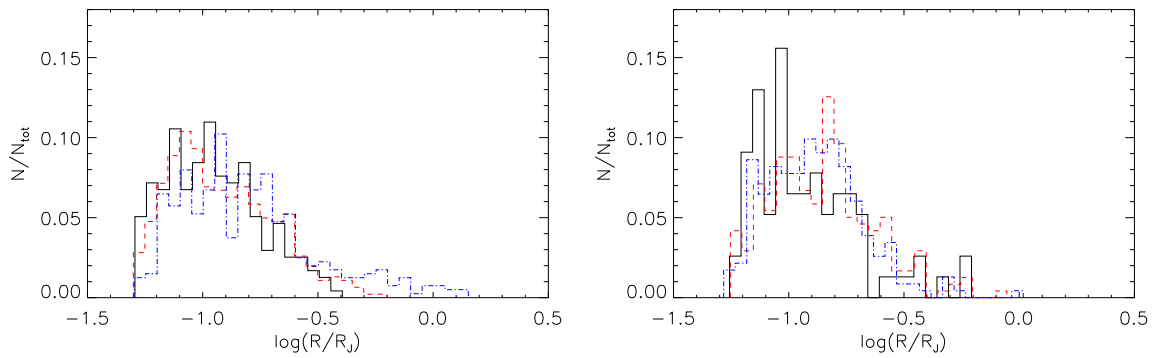


Figure 7.8: Clump size over clump Jeans length distributions at different times. The plot on the left-hand side corresponds to the run in a uniform diffuse medium and the plot on the right to the run in a turbulent diffuse medium. The solid black, dashed red and dash-dotted blue histograms correspond to the 3 Myrs, 5 Myrs and 7 Myrs, respectively.

Figure 7.8 shows the distributions of the ratios of clump sizes over their corresponding Jeans length, at different times. The size distributions of the clumps have a very similar shape and range between the two simulations. As clumps are fairly uniform in density and temperature, their Jeans length does not vary significantly within a single clump. Clumps in general seem to be smaller than their corresponding Jeans length but, as time advances, some of them become large enough to be potentially unstable to gravitational collapse. Of course, as we have not included gravity in these simulations we cannot know if this would actually be the case.

As mentioned earlier, since the formed structures are very filamentary, they are likely to contain more Jeans lengths along a single dimension. Note also that the algorithm we use to find clumps favors the identification of the smallest possible structures as separate entities. As mentioned above however, the clumps we identify are usually parts of larger structures which are dynamically interacting or surrounded by a common warm and more diffuse corona.

7.4 Clump evolution

Although most of the clumps are in low-pressure regions in the simulation, there are some clumps with approximately the same pressure as their surrounding gas. All of the clumps are surrounded by an intermediate pressure corona, which is also thermally unstable.

This, in combination with the fact that clumps show a tendency of decreasing their internal motions with time and that clouds in pressure equilibrium tend to host smaller internal motions leads us to believe that there might be an evolution from clumps out of equilibrium, with strong internal motions to more quiescent clumps.

Figure 7.9 shows the tracks of the same three clumps we traced back in time, on the pressure-density diagram. The dotted line is the cooling-heating equilibrium curve. The cold structures form in an area where cooling dominates, possibly from thermally unstable gas, at the left of the figure. As time goes by they move on the equilibrium curve and gradually increase their density and pressure, always staying on the curve. The timescale of this evolution is about 2-3 Myrs, which corresponds to about 4 - 5 clump sound crossing times.

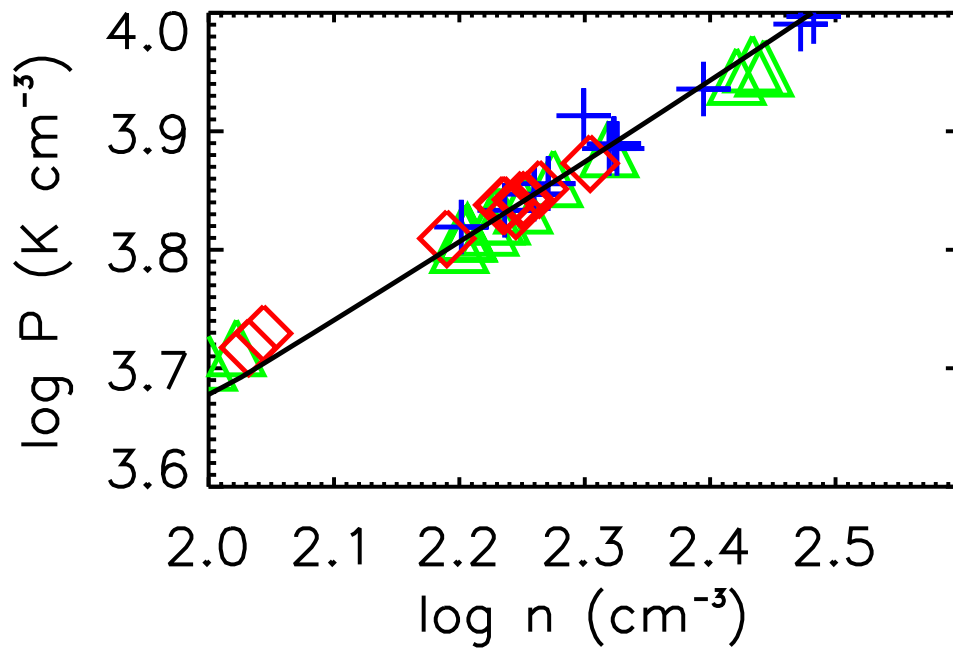


Figure 7.9: Isolated core tracks on a pressure-density diagram. The green triangles correspond to a condensing clump, the blue crosses to a rotating clump and the red diamonds to a clump with random motions. The solid black line is part the cooling-heating equilibrium curve which was shown in figures 6.3 and 6.12.

Metal enrichment of the clouds

8.1 Setup of the simulation

A two-dimensional, high-resolution simulation very similar to those presented in the previous Chapters, is performed using the same setup, namely two young OB associations placed at a certain distance from each other in a warm diffuse background. These cold and dense shells eventually collide in the middle of the computational domain. In this case though, each OB association comprises 20 "average" stars, placed in a circular region of 5 pc radius and the physical size of the domain is half that of the simulations in Chapters 6 and 7.

An important increase in efficiency in comparison to the previous simulations is achieved with the use of Adaptive Mesh Refinement (AMR). Given the nature of the problem under study, the most adequate refinement policy is to trigger the division of a oct when the difference in the gradients of pressure and density exceeds a certain threshold. We have used a threshold equal to 1% in this work. Experimenting with the value of the threshold gave no significant differences in the grid structure, although thresholds higher than 10% failed to capture the shock structure properly.

The supershells in this setup are expanding in a uniform diffuse background, which means that any perturbations that are expected to seed the fluid instabilities we want to study must arise at the grid level. In order then to make this simulation comparable to previous results, we should also seed the perturbations at the smallest grid level and the physical scale for seeding the perturbation should be the same between different runs. For this reason, we initiate the simulation with a nested grid configuration, where the highest resolution region is located at the center of the simulation box. Once the first seeds of the perturbation start to grow, we switch to the adaptive refinement policy described above.

Figure 8.1 shows the behavior of the three different grid configurations. The top row shows the logarithm of hydrogen number density and the bottom row shows the corresponding grid structure. The grid structure for the uniform grid run is, of course, trivial, but it is shown here

This chapter is an adaptation of the paper "On the inefficiency of metal enrichment of cold gas in colliding flow simulations", by E.Ntormousi and A. Burkert, to be submitted to the *Astrophysical Journal*.

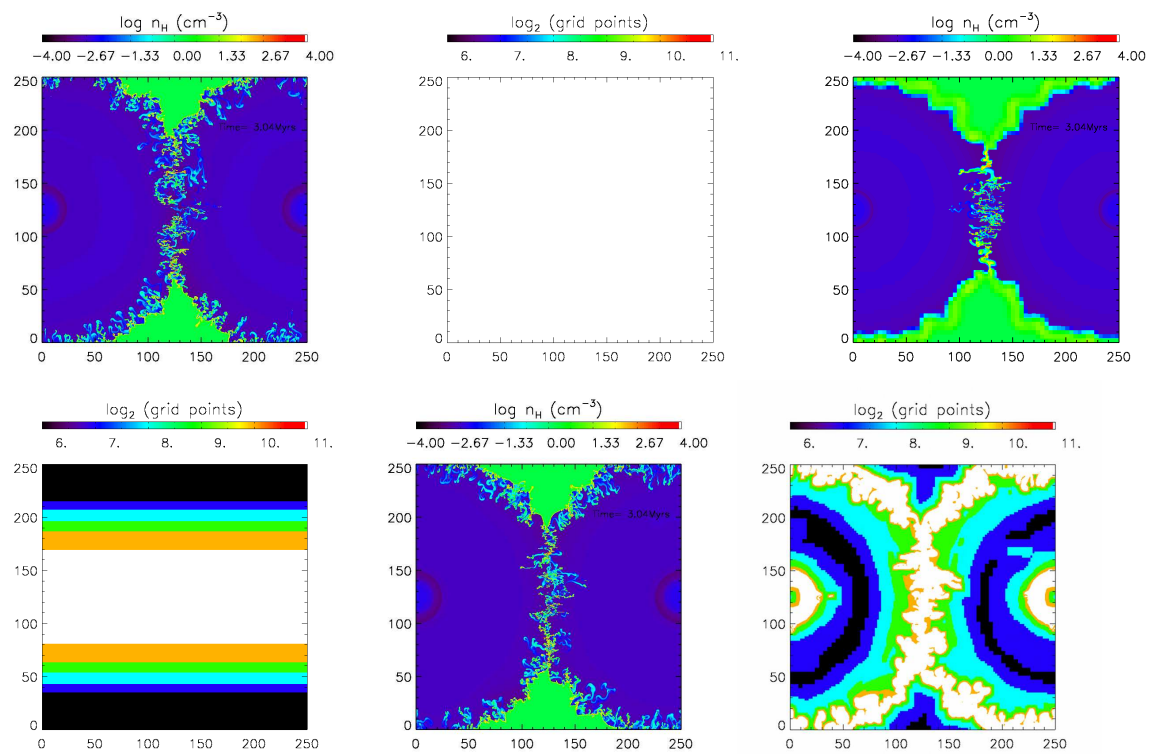


Figure 8.1: Snapshots of three runs using different refinement techniques, taken at the same timestep, about 3 Myrs after star formation. From left to right, uniform grid, geometry-based refined and gradient-based refined grid. The plots on the top row show the logarithm of hydrogen number density and the plots on the bottom row show the corresponding grid structure. The axes coordinates are in parsecs.

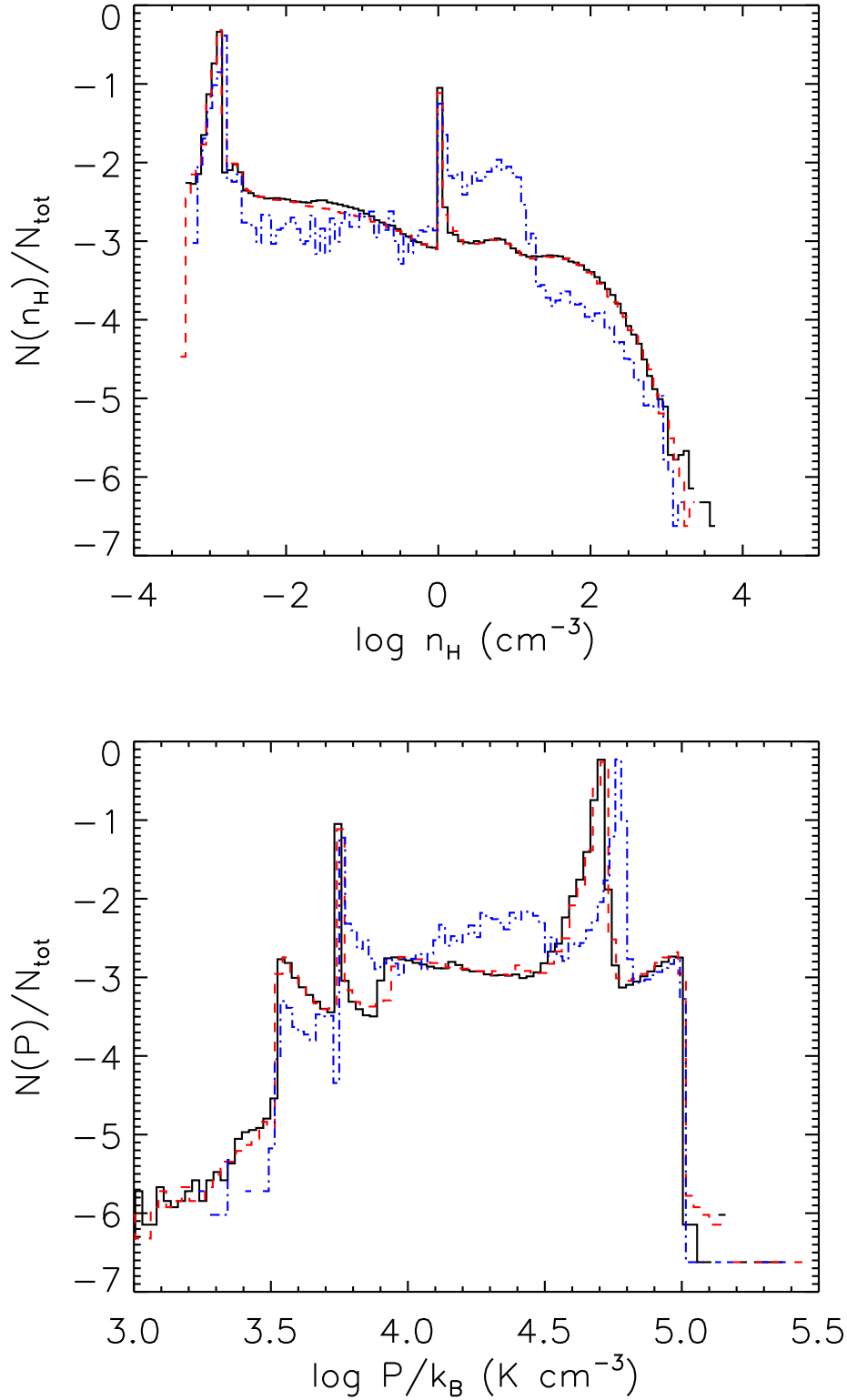


Figure 8.2: Density (top) and pressure (bottom) histograms of the same snapshots shown in Figure 8.1, about 3 Myrs after star formation. The solid black histograms correspond to the run with a uniform grid, the dashed red histograms to the gradient-based AMR run and the dashed-dotted blue histograms to the geometry-based refinement run.

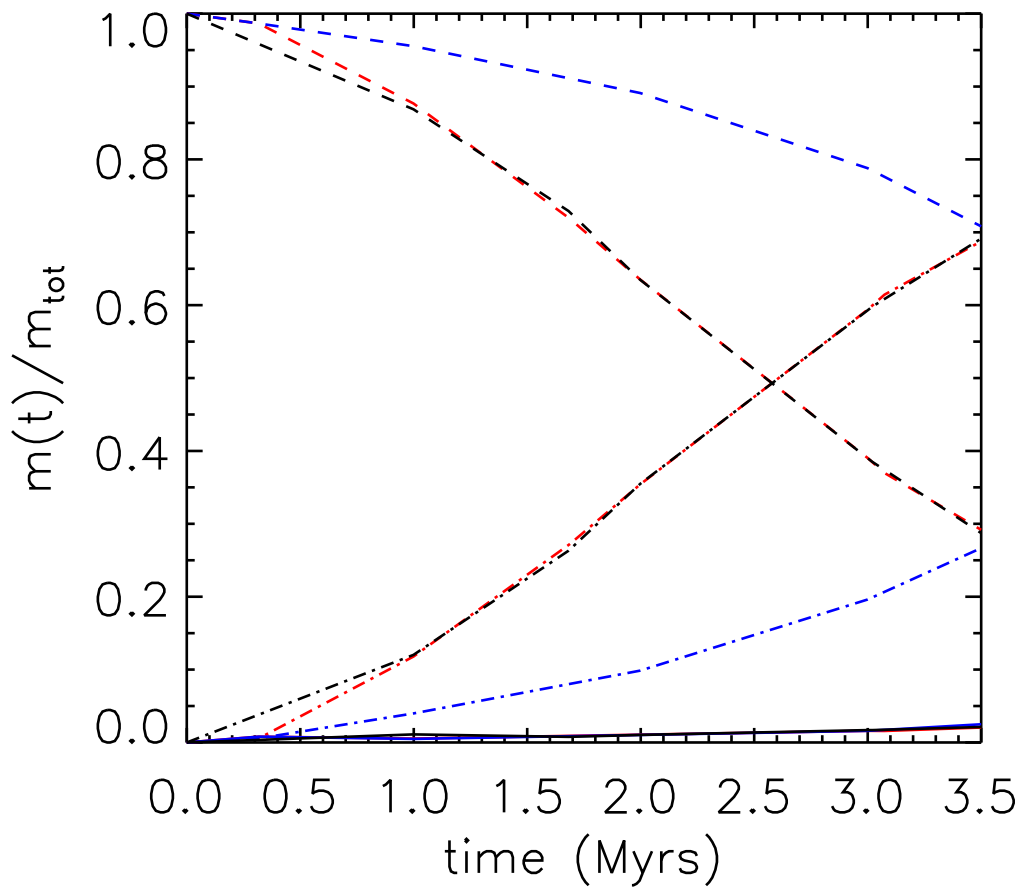


Figure 8.3: Gas mass fractions with time for three models. The black lines correspond to the run with a uniform grid, the red lines to the gradient-based refinement run and the blue lines to the geometry-based refinement run. Dashed lines show the mass fraction of the gas in the warm phase, solid lines show the gas mass fraction in the hot phase and dashed-dotted lines show the gas mass fraction in the cold phase. (Hot phase: gas with $T \geq 25000$ K, warm phase: gas with $100 \text{ K} < T < 25000$ K, cold phase: gas with $T < 100$ K).

anyway for completeness. The density and pressure gradient-based refinement works very well in following the shocks and the locations where cold structure is formed (rightmost panel of Figure 8.1). However, the small-scale noise introduced by the interpolation, in combination with the nonlinear nature of the gas dynamics in this environment leads to slight differences in the morphology of the gas between the uniform and the adaptively refined grid at the same timestep.

There is a minimum resolution below which cold gas does not form at the edges of the shells at all, evident in the run with a nested grid configuration (middle panel of Figure 8.1). In the regions where the grid size is too large the shocks are smoothed out, suppressing the Vishniac Instability and preventing the gas at the edges of the shells from becoming thermally unstable.

The volume fractions of the gas in each phase are practically identical between the uniform grid and the gradient-refined grid simulations (Figure 8.2), however the gas in the uniform grid run is allowed to condense to slightly higher densities, as shown by the density histogram on the top panel of Figure 8.2. The nested grid simulation has significantly less gas in the high-density regime in comparison, due to the lower resolution in the top and bottom parts of the grid.

The corresponding pressure histograms for the three runs are shown on the bottom panel of Figure 8.2. Again, the uniform grid run and the gradient-defined AMR runs seem to agree almost completely, but the geometry-based refinement run has a slightly different configuration, with a lot of gas in the thermally unstable regime, unable to condense and cool further. This is indicative of the result one might get from cooling shock simulations if the resolution is insufficient to capture the initial density enhancements.

The mass fractions of the gas in different temperature regimes are plotted in Figure 8.3. The dotted-dashed lines in this Figure correspond to the cold gas ($T < 100$ K), which forms small dense clumps, the dashed lines correspond to the warm gas ($100 \text{ K} < T < 25000$ K), mainly consisting of the background gas and the coronas around the cold clumps, and the solid lines correspond to the hot gas ($T \geq 25000$ K), mainly located in the wind and the shocked areas. Black color denotes the uniform grid run, blue the geometry-based refinement run and red the gradient-based refinement run. The mass fractions in different phases seem to agree between the uniform grid and the gradient-based grid runs during the whole simulation time, with the cold gas dominating the mass towards the end of the simulation (about 80% of the total mass). However, the nested grid run fails to reach these high mass fractions due to the very low resolution in part of the domain.

In conclusion, the comparison between simulations of this setup with AMR and with uniform grid simulations have shown no difference in the amount of cold gas, the position of the shocks and the sizes or velocity dispersions of the formed clumps. Small differences in the shock morphology are, of course, always present, due to the very nonlinear nature of these phenomena.

For this particular simulation we use a box of 250 pc physical size, at an effective resolution of 2048^2 . The choice of a smaller box with respect to Paper I is not only more physical, in terms of the average distance between OB associations in the Galaxy but it also yields a smaller computational volume for the same physical resolution, significantly reducing the computational cost of the simulation.

We stop the calculation when the turbulence in the collision area starts to expand towards the inflow boundaries. In this particular case this happens 4.36 Mys since star formation in the OB associations.

As mentioned before, the aim of this work is to study the advection of metals from the OB associations to the cold gas formed at the shock wake. This is done by means of a passive advected quantity, representing the metal injection from the stars. A constant amount of metals, equal to 10^{-3} metal particles/cm³ is added at the wind region at each coarse timestep. As this value is totally arbitrary, it can be weighted to simulate different environments.

The amount of metals introduced by the OB associations is assumed here to have a negligible effect on the amount of cold gas formed. In principle, though, extra metals could affect our results due to their contribution to the cooling, which would also change the regime where the gas becomes thermally unstable. In our calculations the most important coolant of the gas is line emission from carbon and oxygen. A decrease in the abundance of these elements would cause the area where we can have phase formation due to the Thermal Instability to shrink, and an enrichment would enlarge the Thermal Instability regime (Wolfire et al., 1995).

Support for the approximation we are making comes from Walch et al. (2011b), who studied the effect of metallicity on the formation of cold gas from Thermal Instability in simulations of turbulence. They found that, for driven turbulence (which is the case in our models), the total amount of cold gas in the simulation is not significantly affected by changes in the metallicity. This means that, as long as the metallicity of the gas we are simulating is high enough to capture the Thermal Instability regime of the ISM, we are not making significant errors in the total amount of cold gas in the domain by ignoring the enrichment from the OB stars in the cooling function.

8.2 Metal enrichment of the gas from the OB associations

Figure 8.4 shows snapshots of the simulation before and after the shell collision. The top panels of this Figure are contours of the logarithm of the gas temperature and the bottom panels show the logarithm of the ratio of metal to hydrogen atoms in the cell.

The general picture of the simulation is the same as in Paper I. The spherical shocks created by the stellar feedback are unstable to the Vishniac instability (Vishniac, 1983, 1994) as small-scale wind imperfections create ripples on their surface. The result of the gas condensation at the peaks of these ripples is to trigger the Thermal Instability (Field, 1965), creating cold and dense clumps at the shock wake. The shear on the shell surface, also caused by the Vishniac Instability, gives rise to characteristic Kelvin-Helmholtz eddies, thus contributing to the dynamics of the newly-formed cold clumps (left panel of Figure 8.4).

When the shells collide, the combination of the large-scale shear by the collision and the small-scale structure already present in the shells gives rise to a turbulent region at the collision interface which contains both warm and cold gas (right panel of Figure 8.4). Turbulence is a very efficient mixing mechanism, so we naturally expect an enhancement in metallicity of the warm gas after the shell collision.

In Figure 8.4, we can indeed see that the warm gas has enhanced metal content. The same can be shown more clearly by plotting the mass fraction of the gas in the computational domain in density-metallicity bins. In Figure 8.5, showing such plots for two snapshots of the simulation, we can see that the dense gas dominates the mass of the gas in the computational domain. At the same time we see that it never reaches relative enrichment of more than 10^{-4} . For comparison, we note that, were the metals ejected by the stars to be instantaneously and homogeneously mixed in the diffuse gas phase, the relative enrichment would be 10^{-2} and if all the metals from the stars ended up in the cold phase, the relative enrichment of that

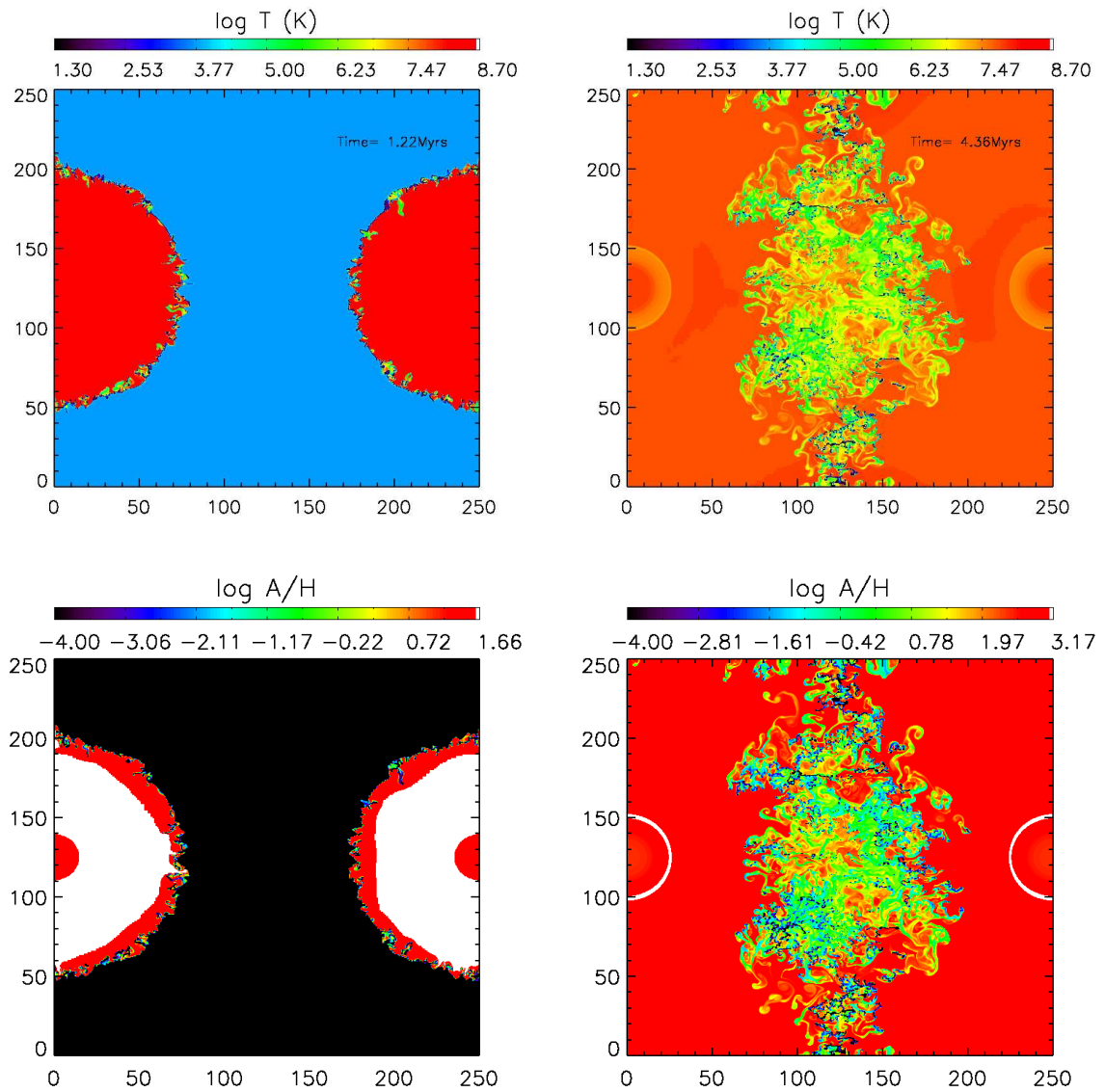


Figure 8.4: Logarithm of temperature (top) and logarithm of relative metal content (bottom) for two snapshots. On the left, 1.22 Myrs and on the right, 4.46 Myrs after star formation took place in the OB associations.

phase would be of about $5 \cdot 10^{-2}$.

Throughout the simulation practically all the metals injected by the OB associations stay in the hot wind, despite the fact that most of the mass is in the cold gas component. At late times a small fraction of the metals (1-5%) mixes into the slightly denser, warm gas ($n_H \simeq 10^{-1}$, $T \simeq 10^5$) due to the shell collision that causes turbulent mixing.

8.3 Metal enrichment of the clumps

A clump is identified as a collection of adjacent cells with densities above 50 cm^{-3} and temperatures lower than 100 K. By this definition alone, Figure 8.5 already indicates that the clumps do not contain significant amounts of material from the OB associations.

To look at the clump metallicities in more detail, we plot their metallicity distributions, shown in Figure 8.6. The top panels in this Figure show the distributions of the mean absolute metal content of the clumps, in the arbitrary units chosen in this simulation for the metallicity ($10^{-3}/\text{cm}^3$ injected in the wind domain at each timestep) and the bottom panels show distributions of the mean metallicity over the mean hydrogen number density of the clumps. The plots on the left-hand side correspond to the snapshot at 1.22 Myrs and the plots on the right-hand side to the final snapshot, at 4.36 Myrs.

Even though the numbers can be rescaled to mean different absolute metal content in the clumps, the important fact here is that the cold phase will always receive at least two orders of magnitude less metals than the diffuse warm phase.

Even though the metal injection from the OB associations does not stop during the simulation time, the metal content of the clumps does not seem to increase significantly. The spread of the distribution of the relative metal content of the clumps seems to increase with time. As the system evolves, new clumps are formed at relatively lower metallicities. The little metals they accumulate over time leads to the formation of a peak in the distribution. However, the maximum value of the distribution does not increase, meaning there is no significant enrichment.

Figures 8.7 and 8.8 show the mean number density of metals in a clump as a function of distance from its closest OB association and as a function of the polar angle with respect to the horizontal line in the middle of the domain, respectively. The amount of metals in a clump does not seem to depend on its position with respect to the OB associations, pointing to a very uniform distribution of metallicities around the young associations.

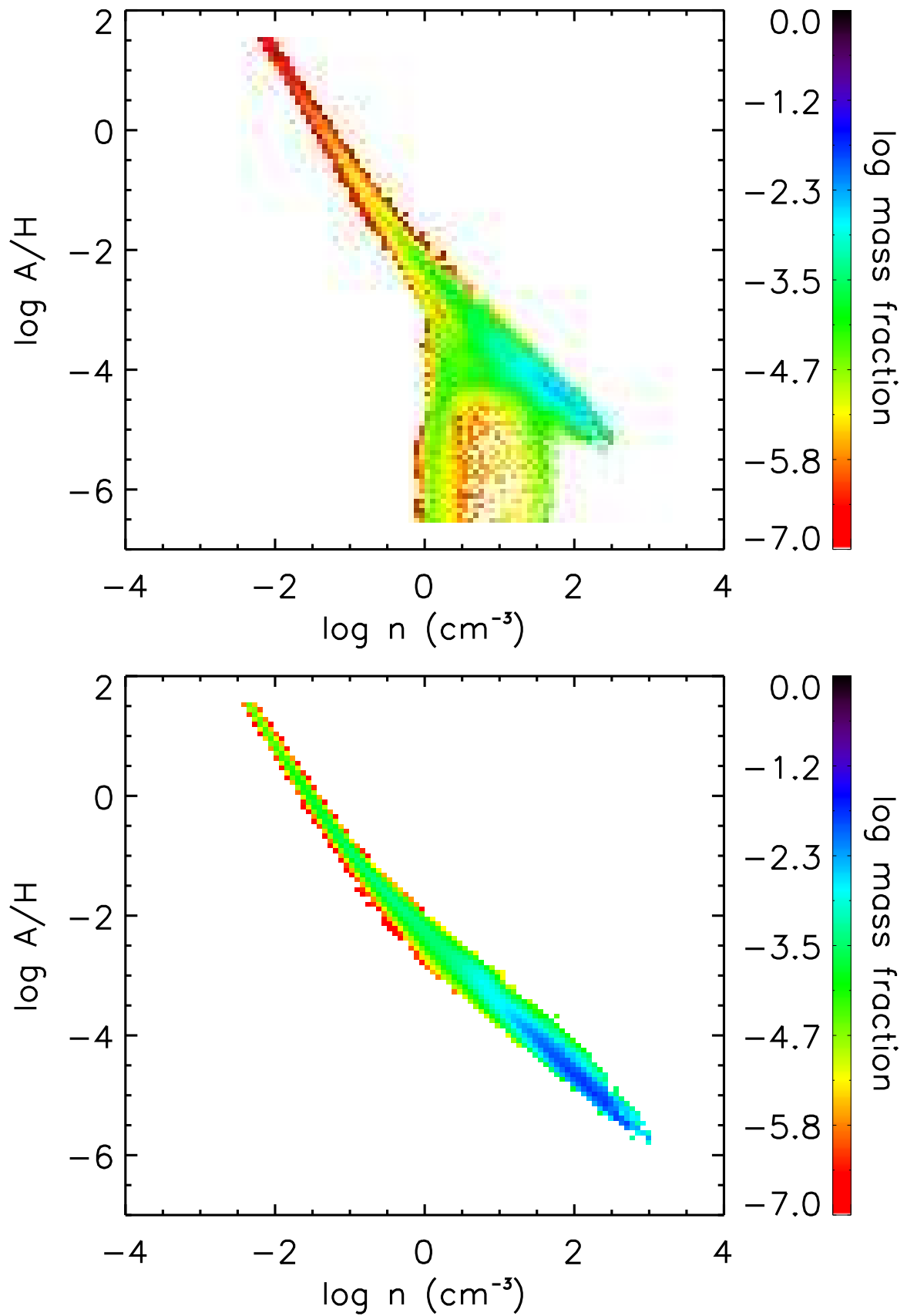


Figure 8.5: Mass fractions in density-metallicity bins at two snapshots, 1.22 Myrs (top) and 4.36 Myrs (bottom) after star formation.

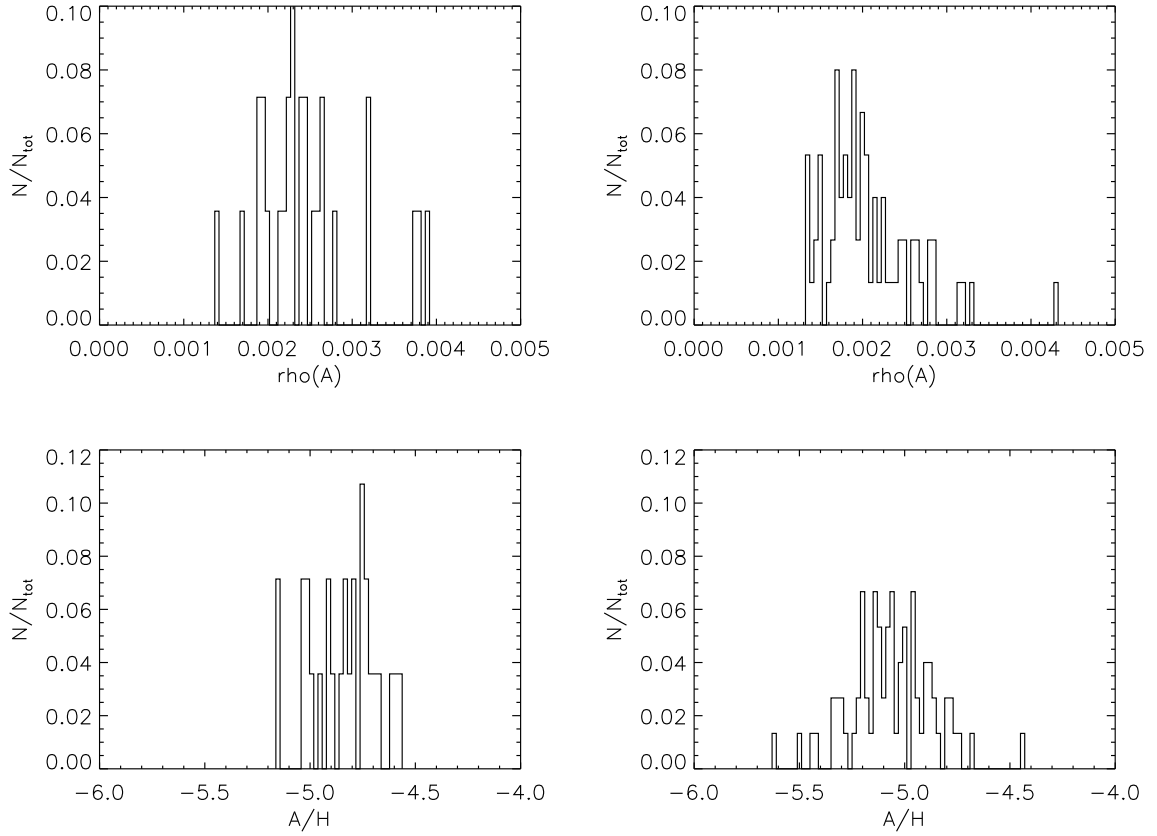


Figure 8.6: Top: Distributions of the absolute metal content of the clumps. Bottom: Distributions of the metal content of the clumps over their hydrogen number density. The data are from snapshots 1.22 Myrs (left) and 4.36 Myrs (right) after star formation.

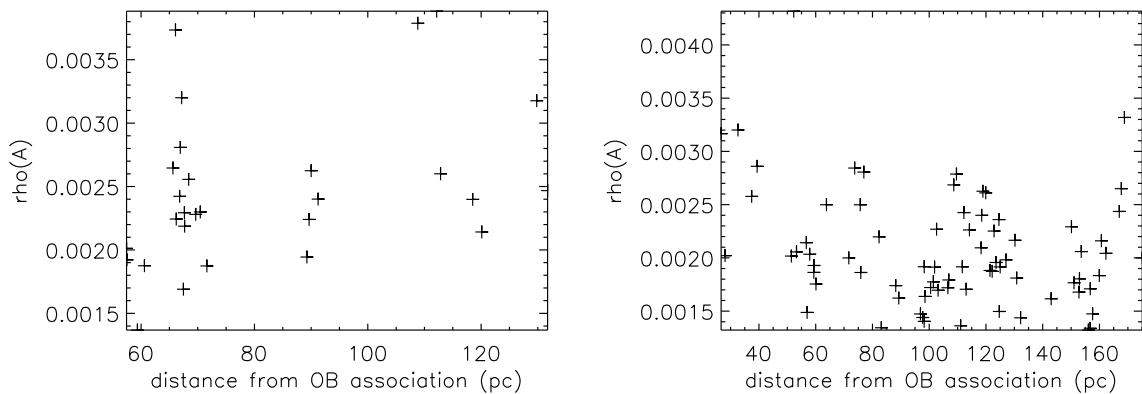


Figure 8.7: Dependence of the clump metal content on their distance from the closest association. The plots are shown at 1.22 Myrs (left) and 4.36 Myrs (right) since the beginning of the simulation.

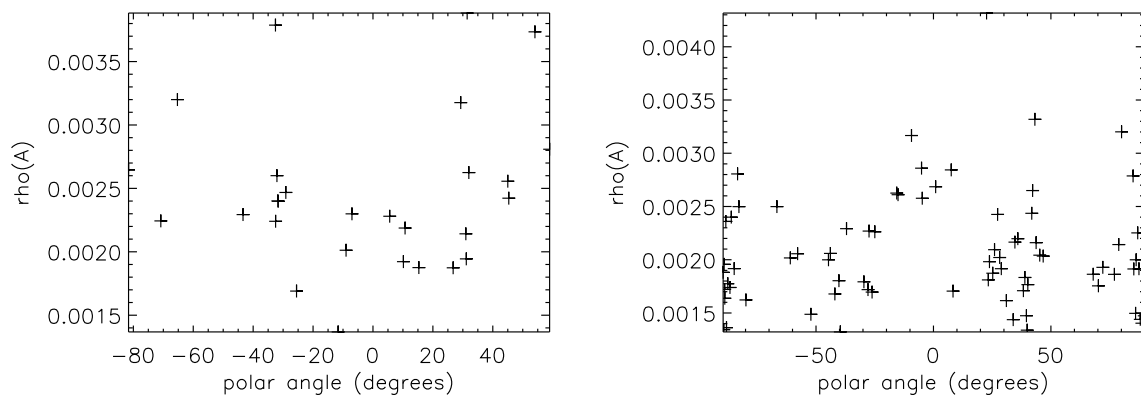


Figure 8.8: Dependence of the clump metal content on their polar angle calculated with respect to the horizontal line at the center of the computational domain. The plots are shown at 1.22 Myrs (left) and 4.36 Myrs (right) since the beginning of the simulation.

Summary and Conclusions

In this text we have presented our work on the formation of cold structure from large-scale colliding flows. In particular, we have shown the results of detailed numerical simulations of colliding superbubbles. These large cavities of hot gas are created by the violent feedback from young massive stars, implemented as a time-dependent energy and mass source in a public hydrodynamics code. The extremely dynamical evolution of the gas was followed to the point of the fragmentation and collision of the dense shells.

Our results provide a picture of the ISM similar to that in Audit & Hennebelle (2005) and Hennebelle & Audit (2007b), where the ISM phases are tightly interwoven, with sharp thermal interfaces between them. Of course, a more detailed comparison is not possible, since that work was done with a much higher resolution, representing a smaller region of the ISM and not including the hot phase. In our simulations, elongated cold structures sit in warm, thermally unstable coronas, submerged in a hot dilute medium that the stellar winds and supernovae from young OB stars create. Clumps are dynamical entities, constantly merging and splitting and in general not in pressure equilibrium with their surrounding gas. In that sense, the picture we see in our simulations is very different from the classical ISM model proposed by McKee & Ostriker (1977), where the clouds are treated as quasi-static spheres. The structures we find are rather long thin filaments, very similar to the large "blobby sheets" proposed by Heiles & Troland (2003).

We identify individual clumps in the simulations by setting density and temperature thresholds and connecting adjacent locations in the simulation domain which exceed these thresholds. This method favors the identification of the smallest cold and dense structures. The clumps tend to be connected in groups within a common warm corona, forming long filaments and are mostly located in areas of lower pressure with respect to their surroundings. The latter causes many of them to condense to higher densities and smaller volumes, almost isothermally. Apart from condensing clumps we find rotating clumps, as well as clumps hosting irregular motions. All these internal motions are reflected in the velocity dispersion as supersonic internal motions. Approximately 11 to 16% of the identified clumps are rotating and are interesting candidates for forming protostellar disks. However, rotation should be studied in three dimensions for more reliable results.

Internal clump motions tend to decrease with time, as the clumps come closer to thermal pressure equilibrium with their warm surroundings. However, if gravity and star formation

was included in our simulations, we would expect these motions to be sustained for longer times due to gravitational collapse and feedback from the newly formed stars in their interior.

Cold clumps in our simulations form by Thermal Instability condensation of the ambient diffuse medium when it is perturbed by the expanding shells. This, in combination with the fact that the mass injected by the OB associations is a very small fraction of the total mass in our domain throughout the simulation, shows that the material forming the new clumps could not have been enriched directly by the supernova explosions. The material ejected from the OB associations will probably enrich the interstellar matter on much larger timescales, after the hot bubbles have mixed with the diffuse medium.

In order to study of metal advection from the hot to the cold ISM, we have presented a simulation of the same setup, using an advected quantity. This quantity was inserted in the region of the domain representing the wind, to represent the metals ejected by the winds and supernova explosions in these OB associations. In this way, we were able to distinguish between material originating from the stars and material originating from the diffuse ISM in the composition of the cold clumps.

We have found that the metal content of the clumps is very low throughout the simulation. The maximum metal to hydrogen number ratio reached in the simulation is about 10^{-4} , two orders of magnitude lower than the value of the same ratio for the warm diffuse medium. The fact that the diffuse gas receives a significant fraction of the injected metals implies that, if molecular clouds were to form in this environment, significant enrichment would be delayed by at least one stellar generation. This effect is even more relevant if we consider that the free-fall time for each of these dense clumps is about 1 Myr, which means that many of them would be collapsing before the end of this simulation, had gravity been considered, leaving even less time for enrichment.

The metal content of the clumps seems to be independent of their position with respect to the OB association. This, in combination with the small spread in cloud metallicities, means that the next stellar generation, formed by the clumps created in such an environment, would be very uniform in its metal content, provided the diffuse component is also well mixed.

Of course, there are many effects that have not been included in this work. For instance, we have assumed that the metal injection from the OB associations is roughly constant with time and that it is uniformly distributed in the wind region. Both these assumptions are questionable. We would, in principle, expect the metals to be contained in small clumps, as part of clumpy winds or fast supernova ejecta, possibly making mixing more efficient. In addition, the wind material should of course differ in quantities and composition from the supernova material, although this would still mostly end up in the diffuse rather than the dense cold phase. These are all complications that should be taken into account in future work.

Thermally unstable gas amounts to about 8 to 10% of the total gas mass in the last snapshots of our simulations, far from the almost 50% that is commonly detected in observations (Heiles & Troland, 2003) or found in simulations of turbulent, thermally bistable flows (Gazol et al., 2001, 2005). This is because our simulations are dominated by what we identify as CNM, that is, gas with temperatures lower than 100K. Due to our very high resolution, this gas is also very dense, reaching hydrogen number densities of the order of 10^5 cm^{-3} . This gas would be mostly molecular, so it would not be identified as cold HI in observations. In simulations with gravity we would not expect to encounter this issue, since gravity would eventually dominate the dynamics of the formed clumps and turn them into stars once they became dense enough, so thermal instability would no longer be responsible for their evolution

at these densities.

The simulations presented here are only a first step to modeling triggered molecular cloud formation using physically motivated colliding flow parameters. We have not attempted a parameter study in this paper, but it will be the object of future work to study the effect of varying the distance between the superbubbles, the number of OB stars creating the superbubbles and the metallicity of the gas.

In this work we have also not taken into account galactic shear or density stratification. Assuming a galactic rotation rate of $26 \text{ km sec}^{-1} \text{ kpc}^{-1}$, the relative shear in our computational box would be 13 km sec^{-1} . This velocity would have a crossing time of approximately 37 Myrs, which is much longer than what our simulations last. Density stratification with a scale height of $H=150\text{pc}$ would cause the superbubbles to expand faster along the vertical direction, but since we are interested mostly in what happens at the superbubble collision interface, we can neglect this effect as a first approximation.

Our calculations also ignore magnetic fields and gravity. We would expect magnetic fields to play a significant role in the dynamics of the problem, both during the expansion of the superbubbles and also during the more complex collision phase, if they had a preferred orientation, but in two dimensions we would not be able to model all relevant phenomena properly anyway. Gravity is essential for studying the evolution of the clumps and for estimating their star forming efficiency. Combining with the modeling of a third dimension, it would give us useful mass estimates of the formed structures. Moving to three dimensions and including gravity is work in process and will be presented in a future paper.

We find the main limitations of our work to be the lack of resolution and bidimensionality. As we have pointed out, our simulations do not reach the resolution required to capture all the relevant physical processes on the smallest scales. We have accounted for small-scale effects by only studying clumps which contain more than 16 grid cells. Higher numerical resolution will certainly provide more insight on the number of formed clumps and their internal structure. Although numerical effects do introduce a thermal conduction effect, explicitly modeling thermal conduction would help set the minimum scale for formed clumps and achieve convergence with increasing resolution. On the other hand, if gravity is simulated it will probably already become important at length scales larger than the Field length.

The restriction of the presented models to two dimensions is emphasizing the formation of filaments. In three dimensions, these structures could have a sheet-like morphology. Gravity could then be responsible for turning these sheets into filaments (Burkert & Hartmann, 2004; Hartmann & Burkert, 2007; Heitsch et al., 2008b).

Bibliography

- Alves, J., Lombardi, M., & Lada, C. J. 2007: *The mass function of dense molecular cores and the origin of the IMF*, A&A, 462, L17
- Audit, E. & Hennebelle, P. 2005: *Thermal condensation in a turbulent atomic hydrogen flow*, A&A, 433, 1
- Ballesteros-Paredes, J., Hartmann, L., & Vázquez-Semadeni, E. 1999: *Turbulent Flow-driven Molecular Cloud Formation: A Solution to the Post-T Tauri Problem?*, ApJ, 527, 285
- Burkert, A. 2006: *The turbulent interstellar medium*, Comptes Rendus Physique, 7, 433
- Burkert, A. & Hartmann, L. 2004: *Collapse and Fragmentation in Finite Sheets*, ApJ, 616, 288
- Burkert, A. & Lin, D. N. C. 2000: *Thermal Instability and the Formation of Clumpy Gas Clouds*, ApJ, 537, 270
- Chandrasekhar, S. 1961, Hydrodynamic and hydromagnetic stability, ed. Chandrasekhar, S.
- Churchwell, E., Babler, B. L., Meade, M. R., Whitney, B. A., Benjamin, R., Indebetouw, R., Cyganowski, C., Robitaille, T. P., Povich, M., Watson, C., & Bracker, S. 2009: *The Spitzer/GLIMPSE Surveys: A New View of the Milky Way*, PASP, 121, 213
- Churchwell, E., Povich, M. S., Allen, D., Taylor, M. G., Meade, M. R., Babler, B. L., Indebetouw, R., Watson, C., Whitney, B. A., Wolfire, M. G., Bania, T. M., et al. 2006: *The Bubbling Galactic Disk*, ApJ, 649, 759
- Dale, J. E., Wunsch, R., Smith, R. J., Whitworth, A., & Palouš, J. 2011: *The fragmentation of expanding shells - III. Oligarchic accretion and the mass spectrum of fragments*, MNRAS, 411, 2230
- Dale, J. E., Wunsch, R., Whitworth, A., & Palouš, J. 2009: *The fragmentation of expanding shells - I. Limitations of the thin-shell approximation*, MNRAS, 398, 1537
- Dalgarno, A. & McCray, R. A. 1972: *Heating and Ionization of HI Regions*, ARA&A, 10, 375
- de Avillez, M. A. & Breitschwerdt, D. 2004: *3D HD and MHD Adaptive Mesh Refinement Simulations of the Global and Local ISM*, in Astrophysics and Space Science Library, Vol. 315, How Does the Galaxy Work?, ed. E. J. Alfaro, E. Pérez, & J. Franco, 331–+

- Dobbs, C. L., Burkert, A., & Pringle, J. E. 2011: *Why are most molecular clouds not gravitationally bound?*, MNRAS, 413, 2935
- Draine, B. T. 2011: *Astronomical Models of PAHs and Dust*, in EAS Publications Series, Vol. 46, EAS Publications Series, ed. C. Joblin & A. G. G. M. Tielens, 29–42
- Ehlerová, S. & Palouš, J. 2005: *H I shells in the outer Milky Way*, A&A, 437, 101
- Elmegreen, B. G. 1994: *A Q condition for long-range propagating star formation*, ApJ, 427, 384
- Elmegreen, B. G. & Lada, C. J. 1977a: *Sequential formation of subgroups in OB associations*, ApJ, 214, 725
- Elmegreen, B. G. & Lada, C. J. 1977b: *Sequential formation of subgroups in OB associations*, ApJ, 214, 725
- Falgarone, E. & Phillips, T. G. 1990: *A signature of the intermittency of interstellar turbulence - The wings of molecular line profiles*, ApJ, 359, 344
- Ferrière, K. M. 2001: *The interstellar environment of our galaxy*, Reviews of Modern Physics, 73, 1031
- Field, G. B. 1965: *Thermal Instability.*, ApJ, 142, 531
- Frisch, U. 1996, Turbulence, ed. Frisch, U.
- Gazol, A., Vázquez-Semadeni, E., & Kim, J. 2005: *The Pressure Distribution in Thermally Bistable Turbulent Flows*, ApJ, 630, 911
- Gazol, A., Vázquez-Semadeni, E., Sánchez-Salcedo, F. J., & Scalo, J. 2001: *The Temperature Distribution in Turbulent Interstellar Gas*, ApJ, 557, L121
- Hartmann, L. 2002: *Flows, Fragmentation, and Star Formation. I. Low-Mass Stars in Taurus*, ApJ, 578, 914
- Hartmann, L., Ballesteros-Paredes, J., & Bergin, E. A. 2001: *Rapid Formation of Molecular Clouds and Stars in the Solar Neighborhood*, ApJ, 562, 852
- Hartmann, L. & Burkert, A. 2007: *On the Structure of the Orion A Cloud and the Formation of the Orion Nebula Cluster*, ApJ, 654, 988
- Haud, U. & Kalberla, P. M. W. 2007: *Gaussian decomposition of H I surveys. III. Local H I*, A&A, 466, 555
- Heiles, C. 1979: *H I shells and supershells*, ApJ, 229, 533
- Heiles, C. 1984: *H I shells, supershells, shell-like objects, and 'worms'*, ApJS, 55, 585
- Heiles, C. & Troland, T. H. 2003: *The Millennium Arecibo 21 Centimeter Absorption-Line Survey. II. Properties of the Warm and Cold Neutral Media*, ApJ, 586, 1067
- Heitsch, F., Hartmann, L. W., & Burkert, A. 2008a: *Fragmentation of Shocked Flows: Gravity, Turbulence, and Cooling*, ApJ, 683, 786

- Heitsch, F., Hartmann, L. W., Slyz, A. D., Devriendt, J. E. G., & Burkert, A. 2008b: *Cooling, Gravity, and Geometry: Flow-driven Massive Core Formation*, ApJ, 674, 316
- Heitsch, F., Slyz, A. D., Devriendt, J. E. G., Hartmann, L. W., & Burkert, A. 2006: *The Birth of Molecular Clouds: Formation of Atomic Precursors in Colliding Flows*, ApJ, 648, 1052
- Hennebelle, P. & Audit, E. 2007a: *On the Structure of the Interstellar Atomic Gas*, in Astronomical Society of the Pacific Conference Series, Vol. 365, SINS - Small Ionized and Neutral Structures in the Diffuse Interstellar Medium, ed. M. Haverkorn & W. M. Goss, 133–+
- Hennebelle, P. & Audit, E. 2007b: *On the structure of the turbulent interstellar atomic hydrogen. I. Physical characteristics. Influence and nature of turbulence in a thermally bistable flow*, A&A, 465, 431
- Hollenbach, D. J. & Thronson, Jr., H. A., eds. 1987, Astrophysics and Space Science Library, Vol. 134, Interstellar processes; Proceedings of the Symposium, Grand Teton National Park, WY, July 1-7, 1986
- Kennicutt, Jr., R. C., Calzetti, D., Walter, F., Helou, G., Hollenbach, D. J., Armus, L., Bendo, G., Dale, D. A., Draine, B. T., Engelbracht, C. W., Gordon, K. D., et al. 2007: *Star Formation in NGC 5194 (M51a). II. The Spatially Resolved Star Formation Law*, ApJ, 671, 333
- Kim, W. & Ostriker, E. C. 2002: *Formation and Fragmentation of Gaseous Spurs in Spiral Galaxies*, ApJ, 570, 132
- Kim, W. & Ostriker, E. C. 2006: *Formation of Spiral-Arm Spurs and Bound Clouds in Vertically Stratified Galactic Gas Disks*, ApJ, 646, 213
- Klessen, R. S. 2001: *The Formation of Stellar Clusters: Mass Spectra from Turbulent Molecular Cloud Fragmentation*, ApJ, 556, 837
- Kochanek, C. S. 2011: *The Astrophysical Implications of Dust Formation during the Eruptions of Hot, Massive Stars*, ApJ, 743, 73
- Kolmogorov, A. 1941: *The Local Structure of Turbulence in Incompressible Viscous Fluid for Very Large Reynolds' Numbers*, Akademiia Nauk SSSR Doklady, 30, 301
- Koyama, H. & Inutsuka, S. 2004: *The Field Condition: A New Constraint on Spatial Resolution in Simulations of the Nonlinear Development of Thermal Instability*, ApJ, 602, L25
- Lada, C. J., Alves, J., & Lada, E. A. 1999: *Infrared Extinction and the Structure of the IC 5146 Dark Cloud*, ApJ, 512, 250
- Lada, C. J., Alves, J. F., & Lombardi, M. 2007: *Near-Infrared Extinction and Molecular Cloud Structure*, Protostars and Planets V, 3
- Landau, L. D. & Lifshitz, E. M. 1959, Fluid mechanics, ed. Landau, L. D. & Lifshitz, E. M.
- Larson, R. B. 1981: *Turbulence and star formation in molecular clouds*, MNRAS, 194, 809

- Lequeux, J. 2005, *The interstellar medium*, ed. Lequeux, J.
- Mac Low, M., Klessen, R. S., Burkert, A., & Smith, M. D. 1998: *Kinetic Energy Decay Rates of Supersonic and Super-Alfvénic Turbulence in Star-Forming Clouds*, *Physical Review Letters*, 80, 2754
- McCray, R. & Kafatos, M. 1987a: *Supershells and propagating star formation*, *ApJ*, 317, 190
- McCray, R. & Kafatos, M. 1987b: *Supershells and propagating star formation*, *ApJ*, 317, 190
- McKee, C. F. & Ostriker, J. P. 1977: *A theory of the interstellar medium - Three components regulated by supernova explosions in an inhomogeneous substrate*, *ApJ*, 218, 148
- Molinari, S., Swinyard, B., Bally, J., Barlow, M., Bernard, J., Martin, P., Moore, T., Noriega-Crespo, A., Plume, R., Testi, L., Zavagno, A., et al. 2010: *Hi-GAL: The Herschel Infrared Galactic Plane Survey*, *PASP*, 122, 314
- Nigra, L., Gallagher, III, J. S., Smith, L. J., Stanimirović, S., Nota, A., & Sabbi, E. 2008: *NGC 602 Environment, Kinematics and Origins*, *PASP*, 120, 972
- Ntormousi, E., Burkert, A., Fierlinger, K., & Heitsch, F. 2011: *Formation of Cold Filamentary Structure from Wind-blown Superbubbles*, *ApJ*, 731, 13
- Ntormousi, E. & Sommer-Larsen, J. 2010: *Hot gas haloes around disc galaxies: O VII column densities from galaxy formation simulations*, *MNRAS*, 409, 1049
- Padoan, P. 1995: *Supersonic turbulent flows and the fragmentation of a cold medium*, *MNRAS*, 277, 377
- Parmentier, G. 2011: *From the molecular-cloud- to the embedded-cluster-mass function with a density threshold for star formation*, *MNRAS*, 413, 1899
- Pringle, J. E., Allen, R. J., & Lubow, S. H. 2001: *The formation of molecular clouds*, *MNRAS*, 327, 663
- Salpeter, E. E. 1977: *Formation and destruction of dust grains*, *ARA&A*, 15, 267
- Schneider, S. & Elmegreen, B. G. 1979: *A catalog of dark globular filaments*, *ApJS*, 41, 87
- Sutherland, R. S. & Dopita, M. A. 1993: *Cooling functions for low-density astrophysical plasmas*, *ApJS*, 88, 253
- Teyssier, R. 2002: *Cosmological hydrodynamics with adaptive mesh refinement. A new high resolution code called RAMSES*, *A&A*, 385, 337
- Tielens, A. G. G. M. 2005, *The Physics and Chemistry of the Interstellar Medium*, ed. Tielens, A. G. G. M.
- Vázquez-Semadeni, E., Gómez, G. C., Jappsen, A. K., Ballesteros-Paredes, J., González, R. F., & Klessen, R. S. 2007: *Molecular Cloud Evolution. II. From Cloud Formation to the Early Stages of Star Formation in Decaying Conditions*, *ApJ*, 657, 870

- Vázquez-Semadeni, E., Ryu, D., Passot, T., González, R. F., & Gazol, A. 2006: *Molecular Cloud Evolution. I. Molecular Cloud and Thin Cold Neutral Medium Sheet Formation*, ApJ, 643, 245
- Verschuur, G. L. 2004: *Interstellar Neutral Hydrogen Emission Profile Structure*, AJ, 127, 394
- Vishniac, E. T. 1983: *The dynamic and gravitational instabilities of spherical shocks*, ApJ, 274, 152
- Vishniac, E. T. 1994: *Nonlinear instabilities in shock-bounded slabs*, ApJ, 428, 186
- Vishniac, E. T. & Ryu, D. 1989: *On the stability of decelerating shocks*, ApJ, 337, 917
- Voss, R., Diehl, R., Hartmann, D. H., Cerviño, M., Vink, J. S., Meynet, G., Limongi, M., & Chieffi, A. 2009: *Using population synthesis of massive stars to study the interstellar medium near OB associations*, A&A, 504, 531
- Walch, S., Whitworth, A. P., & Girichidis, P. 2011a: *The influence of the turbulent perturbation scale on pre-stellar core fragmentation and disc formation*, MNRAS, 1725
- Walch, S., Wünsch, R., Burkert, A., Glover, S., & Whitworth, A. 2011b: *The Turbulent Fragmentation of the Interstellar Medium: The Impact of Metallicity on Global Star Formation*, ApJ, 733, 47
- Whitworth, A. P., Bhattal, A. S., Chapman, S. J., Disney, M. J., & Turner, J. A. 1994: *Fragmentation of shocked interstellar gas layers.*, A&A, 290, 421
- Williams, J. P., Blitz, L., & McKee, C. F. 2000: *The Structure and Evolution of Molecular Clouds: from Clumps to Cores to the IMF*, Protostars and Planets IV, 97
- Wolfire, M. G., Hollenbach, D., McKee, C. F., Tielens, A. G. G. M., & Bakes, E. L. O. 1995: *The neutral atomic phases of the interstellar medium*, ApJ, 443, 152
- Wong, T. & Blitz, L. 2002: *The Relationship between Gas Content and Star Formation in Molecule-rich Spiral Galaxies*, ApJ, 569, 157
- Wünsch, R., Dale, J. E., Palouš, J., & Whitworth, A. P. 2010: *The fragmentation of expanding shells - II. Thickness matters*, MNRAS, 407, 1963
- Yang, C., Gruendl, R. A., Chu, Y., Mac Low, M., & Fukui, Y. 2007: *Large-Scale Gravitational Instability and Star Formation in the Large Magellanic Cloud*, ApJ, 671, 374
- Zuckerman, B. & Evans, II, N. J. 1974: *Models of massive molecular clouds*, ApJ, 192, L149

Acknowledgments

This thesis represents the efforts of the last four years and signifies the beginning of my research career. It would have been impossible for me though to reach this point without the support of several people in my environment. I take this opportunity to thank them.

I am grateful to my PhD advisor, Andreas Burkert, for all our interesting discussions, for sharing his excitement for science with me and for helping my growth as an independent researcher with his sincere support.

I received a lot of practical help for my thesis work from Fabian Heitsch. Not only did he help me gain insight into the physics of the ISM by sharing his experience with me, but he also trusted me with some of his codes. In particular, the calculations of the cooling and heating rates, as explained in Chapter 2 have been calculated with his code.

Katharina Fierlinger shared her PhD work on implementing stellar feedback in RAMSES with me. Without her contribution a lot of this work would not have been possible. In addition, her careful observations significantly improved this work. Of course, I am also grateful to Rasmus Voss for providing the stellar feedback data for this work and for being always available for questions regarding his calculations.

I also thank all my friends and colleagues here at the LMU Observatory, Thorsten Naab, Peter Johansson and Roland Jesseit, not only for technical advice, but also for all the fun we have had these years and for their kind words of advice at hard times.

To my Physics Diploma supervisor at the Aristotle University of Thessaloniki, Loukas Vlahos, an eternal "thank you" for believing in me from the start and for encouraging me to pursue a career as a scientist.

To my family, all my love and gratitude for always being there for me and for all the sacrifices they've made so that I can fulfill my dreams.

Finally, to my partner, Jose Luis Pinar, a big thank you from my heart for your faith in me, for your support and understanding. I would never have reached this far without you.

Curriculum Vitae

Personal

Name: Evangelia Ntormousi
Born: 31st of March, 1984
Citizenship: Greek
Address: Scheinerstr. 1, Munich, Germany D-81679

Education

2007–date	Ph.D in Astrophysics	International Max Planck Research School (IMPRS), USM-LMU
2001–2007	Bachelor and Masters in Physics	Aristotle University Thessaloniki, Greece

Publications

- E. Ntormousi, A. Burkert, On the inefficiency of metal enrichment in colliding flow simulations, in prep.
- E. Ntormousi, A. Burkert, K. Fierlinger and F. Heitsch, Formation of cold filamentary structure from wind-blown superbubbles, *ApJ*, 731, 13
- E. Ntormousi, J. Sommer-Larsen, Hot gas haloes around disc galaxies, 2010, *MNRAS*, 409, 1049